UC Berkeley
UC Berkeley Electronic Theses and Dissertations

Title

A Particle-Level Study of Smear Buildup in Heat-Assisted Magnetic Recording Disk Drives

Permalink

https://escholarship.org/uc/item/8733x6gp

Author

Tom, Roshan Mathew

Publication Date

2024

Peer reviewed|Thesis/dissertation

A Particle-Level Study of Smear Buildup in Heat-Assisted Magnetic Recording Disk Drives

By

Roshan Mathew Tom

A dissertation submitted in partial satisfaction of the

requirements for the degree of

Doctor of Philosophy

in

Engineering - Mechanical Engineering

in the

Graduate Division

of the

University of California, Berkeley

Committee in charge:

Professor David B. Bogy, Chair
Professor Christopher Dames
Professor Jon Wilkening

Summer 2024

A Particle-Level Study of Smear Buildup in Heat-Assisted Magnetic Recording Disk Drives

Abstract

A Particle-Level Study of Smear Buildup in Heat-Assisted Magnetic Recording Disk Drives

by

Roshan Mathew Tom

Doctor of Philosophy in Engineering - Mechanical Engineering

University of California, Berkeley

Professor David B. Bogy, Chair

Ever since the first hard disk drive (HDD) was invented in 1956, it has played a dominant role in global data storage needs. Conventional HDDs, however, have reached the theoretical density limit, called the superparamagnetic limit. Heat-assisted magnetic recording (HAMR) is a novel HDD variant that has been proven to break this theoretical limit. In this technology, a tiny laser is embedded in the read-write head that heats a nanoscale spot in the disk to several hundred Kelvin. The elevated temperature enables writing on highly coercive disks that resist the superparamagnetic effect. The physics underlying HAMR has proven to work; however, a commercial implementation has been met with numerous engineering challenges. Due to its complex nature, the head-disk interface (HDI) remains susceptible to premature failure. One key challenge is called smear, which is a contamination buildup on the head. This smear ultimately causes the head to crash on the disk, severely limiting the lifetime of HAMR drives. Therefore, mitigating smear is indispensable in the quest for reliable hard drives. This dissertation uses a range of numerical techniques to study the transport of smear nanoparticles in the head-disk interface.

We begin with a study of the HDI using classical continuum analysis. The temperature field and thermal protrusion on the head and disk surfaces are calculated by employing the transient heat conduction equation and a thermo-mechanical model of a slider. These calculations revealed the presence of a thermal spot in both the head and the disk surface, with the disk exhibiting significantly higher temperatures. We then explored the effect of the thermal fly-height control (TFC) power and the disk rotation speed on the head temperature. Additionally, a laser-induced protrusion was observed and studied on the head surface.

Next, we introduced the concept of smear as nanoparticles by calculating the optical and air-bearing related force. Using the Rayleigh approximation, the optical force was calculated on a spherical and ellipsoidal nanoparticle. The resulting force field revealed the presence of an optical trap just under the near-field transducer (NFT). A comparison with appropriate drag and thermophoresis force showed that optical forces could be significant for nanoparticles

with large volumes, such as flat ellipsoids. Further, metals of all sizes are sensitive to this force due to their permittivity satisfying the Frohlich condition. Also, dielectric particles are found to congregate near large metallic contaminants due to the formation of a secondary surface plasmon on its surface. We then quantified the air-bearing related forces considering the Chapman-Enskog velocity distribution of the air-bearing. The resulting equation revealed three forces: drag, thermophoresis, and lift. Of these, lift forces were found to be negligible. Then, a sensitivity analysis over different parameters revealed the conditions where each force dominates. We found that smaller nanoparticles in light gases experience higher thermophoresis force, whereas heavier nanoparticles in heavy gases experience higher drag. These results can help control the growth of smear in the head-disk interface.

We also devised a novel hybrid simulation strategy to model the head surface smear growth. The technique accelerates a molecular dynamics simulation by calculating the force field derived from prior calculations. This simulation strategy successfully replicated the streak-like features on the head found in experiments. Two types of streaks were observed: a thick streak that occurred due to direct disk-to-head transport and a thin streak due to the oscillating motion of the nanoparticles in the air-bearing. The hybrid simulation was demonstrated to be an effective tool for simulating smear over long timescales.

Further, we used the direct simulation Monte Carlo (DSMC) method to study the air bearing under nanoscale spacings. The DSMC method incorporated the consistent Boltzmann algorithm (CBA) to account for dense gas behavior. It revealed the presence of a vertical drift in the air bearing due to the temperature difference between the head and the disk. We observed significant water vapor levels due to the high saturation pressure of the head disk interface. We also observed the particles' near ballistic trajectory under ultra-low spacing. This prompted the examination of material transport in ultra-low flying conditions where the air-bearing molecules are sparse. The imbalance in the head and disk temperatures resulted in an imbalance in the van der Waals forces, which transported smear nanoparticles to the head. This effect was found to be significant for clearance less than 2 nm.

Finally, we conclude by summarizing this dissertation's novel results, commenting on the nature of the smear formation, and proposing mechanisms that may help mitigate it.

Achachan, Amma, Divya, Nandu, and

To Him who upholds the universe by the word of His power
(Hebrews 1:3)

Contents

List of Figures

List of Tables

Abbreviations

ABS	Air-Bearing Surface
AD	Areal Density
AI	Artificial Intelligence
BPR	Bit-patterned Recording
BTE	Boltzmann Transport Equation
CBA	Consistent Boltzmann Algorithm
CE	Chapman-Enskog
CML	Computer Mechanics Laboratory
DLC	Diamond Like Carbon
DSMC	Direct Simulation Monte Carlo
ePMR	Energy-assisted Perpendicular Magnetic Recording
FH	Fly Height
FHC	Fly Height Change
FWHM	Full-Width Half Maximum
GMR	Giant Magnetoresistance
HAMR	Head-Assisted Magnetic Recording
HDD	Hard Disk Drives
HDI	Head-Disk Interface
HTC	Heat Transfer Coefficient
LHL	Laser Heat Loss
LSP	Localized Surface Plasmon
LSPR	Localized Surface Plasmon Resonance
MA	Micro Actuator
MAMR	Microwave-Assisted Magnetic Recording
MD	Molecular Dynamics
MFP	Mean Free Path
MGL	Molecular Gas Lubrication
NAS	Network Attached Storage
NFT	Near Field Transducer
PFPE	Perfluoropolyether
PMR	Perpendicular Magnetic Recording
RH	Relative Humidity
RPM	Rotations Per Minute
SMR	Shingled Magnetic Recording
SNR	Signal-to-Noise Ratio
SP	Surface Plasmon
SPARTA	Stochastic Parallel Rarefied-gas Time-accurate Analyzer
SPP	Surface Plasmon Polaritons
SSD	Solid State Drives

TFC	Thermal Fly-Height Control
THC	Transient Heat Conduction
TMR	Tunneling Magnetoresistance
VCM	Voice Coil Motor
WG	Waveguide
b	bit
B	Byte = 8 bits
KB	Kilobyte = 1000 Bytes
MB	Megabyte = 1000 Kilobytes
GB	Gigabyte = 1000 Megabytes
TB	Terabyte = 1000 Gigabytes
PB	Petabyte = 1000 Terabytes
EB	Exabyte = 1000 Petabytes
ZB	Zettabyte = 1000 Exabytes
YB	Yotabyte = 1000 Zettabytes
	*The storage industry uses steps of 1000 rather than 1024.

Acknowledgments

First and foremost, I want to express my deep gratitude to my advisor, Prof. David Bogy. His guidance and support have been instrumental in my Ph.D. journey. He allowed me to pursue my research interests and provided timely motivation when needed. The weekly meetings kept me on track. I am truly grateful for his mentorship over the past five years.

I also thank Prof. Jon Wilkening and Prof. Chris Dames for their invaluable contributions as members of my doctoral committee. Their courses in mathematics and heat transfer have significantly influenced my research. I am also grateful to Prof. Papadopoulos and Prof. Govindjee during my Quals. I appreciate Prof. Papadopoulos' guidance during my first year, which was crucial in helping me acclimate to the US. I thank the staff (especially Yawo) at the ME department for all the logistics. I admire their commitment to the well-being of the students.

I want to thank Western Digital for two summer internships, which have been invaluable to this Ph.D. I especially want to thank Dr. Robert Smith, who taught me how to conduct research in modeling hard drives. I also thank Dr. Qing Dai, Dr. Sukumar Rajauria, Dr. Oscar Ruiz, Dr. Erhard Schreck, and Dr. Tan Trinh for their mentorship. Not only academically, but those summers were refreshing in every way possible. I enjoyed the friendships with other employees and interns, the long drives in the summer heat, the adventures, and the comfortable accommodations. I especially cherish WD cafe lunches. I can't think of something more refreshing than a shared meal after a morning of hard work. This dissertation would not have been there if it had not been for those two summers.

I am grateful to all my colleagues at the Computer Mechanics Lab at Berkeley — Dr. Siddhesh Sakhalkar, Dr. Amin Ghafari, Dr. Qilong Cheng, Dr. Bair Budaev, Nikhil PS, and Yiheng Li. The numerical simulation and experiments done by Siddhesh and Qilong laid the foundation for my research. I also want to thank them for their advice on navigating my Ph.D. and publishing papers. I thank ASRC and CML for supporting me during this period.

I also thank all the people who gave me technical advice. I thank Dr. Matthew Mate and Dr. Bruno Marchon for their insights into the unique behavior of PFPE molecules. I thank the DSMC experts—Prof. Alejandro Garcia, Dr. Michael Gallis, and Dr. Steve Plimpton—for discussing DSMC and using SPARTA. I further thank all my professors from IIT Madras, particularly Prof. Saravanan and Prof. Pillai, for teaching me the foundations of research.

I also thank all my friends in the Bay Area who made this place feel like another home. My friends at Berkeley - Nikhil PS, Sruthi, Vaishnavi, and Devanshi. You remind me of India, feeding me good Indian food when I crave it. I thank everyone at Focalpoint Bible Church for taking me as one of their own. I especially thank Kevin, Jason, Elliot, Thomas, Tony, and Manny. I remember our late-night conversations on theology, life, and basically every topic on earth. Thank you for your constant encouragement, which has been invaluable. I also thank Charlie Nason for mentoring me, listening to my concerns, breaking through my convoluted thoughts, and giving me advice. I also thank Mike, Steve, Jonathan, Vivian, Josh, Joni, Jasper, Elliot, and everyone else. I have enjoyed being at the church with you.

Chapter 1

Introduction

In this age, data is ubiquitous. The ability to send, store, retrieve, and transmit data forms the cornerstone of the digital revolution [1]. In 2023 alone, 120 zettabytes (1 trillion gigabytes) of data are estimated to have been created, captured, copied, and consumed in the world [2]. If each bit, represented by a penny, were stacked on each other, the combined height would stretch over 1200 light-years! Data is the driving force behind innovation and decision-making processes, from the latest scientific advancements to breakthroughs in healthcare. One example of the power of data is the development of artificial intelligence (AI). AI algorithms depend on vast datasets to train themselves. The resulting AI systems have become integral to various aspects of our lives - from mundane customer service to expressive art.

The explosion of data has led to a rise in demand for fast, cheap, and convenient ways to store data. Massive data storage services such as Google Drive, iCloud, Box, and Amazon AWS are gaining popularity. These businesses can utilize various methods of storing data. Solid state drives (SSD), hard disk drives (HDD), tape storage, and optical storage are some of the methods. However, due to the scalability and price, HDD stands out among all other forms of enterprise data storage. As a result, cloud data centers choose HDDs to store up to 90% of the data [3]. Even on the consumer end, there has been a trend to use network-attached storage (NAS) systems for daily use due to the availability of fast and reliable internet. Many NAS manufacturers, such as Synology NAS, are built around hard drives. Therefore, even though most consumers only see SSD storage devices, most of their data is stored on HDDs.

The demand for data will only continue to rise. Using existing HDD technology for the data storage needs of the future is unfeasible. The availability of raw materials, manufacturing limitations, power requirements, and environmental concerns would significantly limit future expansion. Therefore, there is a vital need to design new HDDs that are faster and cheaper and store more data than ever. Heat-assisted magnetic recording (HAMR) is widely considered to be the way forward. This dissertation investigates some specific challenges toward the commercial success of HAMR. This chapter serves as an introduction. Sec. 1.1 briefly explains the relevant technology behind HDDs, and Sec. 1.2 presents the additional innovations in HAMR. Then, Sec. 1.3 introduces the HDI challenges in HAMR, focusing on the issue

of smear. Sec. 1.4 details the objective of this dissertation, and Sec. 1.5 contains the organization and the novel contributions of this dissertation.

1.1 The Hard Disk Drive

The history of HDDs dates back to 1956 when IBM first rolled out the first HDD for its RAMAC 305 computer [4]. It was bigger than a refrigerator, weighed more than a ton, and could hold less than 4 megabytes (MB) of data. Since then, this technology has seen incredible innovations. In 2023, Western Digital released 28 terabytes (TB) HDD (1 TB $= 10^6$ MB) in a 3.5-inch form factor, weighing only 670 grams [5]. This translates to an improvement of over 10 billion. Such progress is only rivaled by the semiconductor industry.

The internal view of the HDD is shown in Fig. 1.1. The main components are the spindle that rotates the disk at several thousand rotations per minute (RPM), a magnetic disk where the data is stored, a slider containing read/write transducers to store and retrieve data, a suspension system to maintain a constant spacing between the slider and the disk, an actuator arm, and a voice coil motor (VCM) that controls the radial movement of the slider [6].

Several disks are clamped on the motor-driven spindle that spins at 5000-10000 RPM. Each disk has several layers, as shown in Fig. 1.2. The base is a substrate made of either glass or aluminum-magnesium alloy. This layer is generally a few millimeters thick, giving the disk its structural strength. On top of the substrate, several metallic layers that are a few nanometers thick are deposited. One of these layers is made of a chromium-cobalt-platinum alloy, where the data is stored. The circular layer is divided into concentric radial segments, which are then divided into several sectors. A sector is the smallest storage unit of the disk, typically 512 bytes in length. Within a sector, each magnetic grain is magnetized by the write head. The orientation of these grains denotes 1s and 0s [7]. To increase the signal-to-noise ratio (SNR), multiple adjacent grains are magnetized in the same direction to operate as 1 bit. Above the disk magnetic layer, a 2nm thick diamond-like carbon (DLC) layer is deposited to protect against impact, wear, and corrosion. Finally, a 1 nm thick perfluoropolyether (PFPE) lubricant layer is deposited above the DLC to reduce wear and friction between the read/write head and the disk. PFPE lubricants are used because of their beneficial properties, such as low surface energy, viscosity, and vapor pressure. They are also chemically and thermally stable [6].

The read and write operations are done through a slider, as shown in Fig 1.3a. The trailing edge portion of the slider forms the head. It contains two sensors (Fig 1.4b), one for writing and the other for reading. The read sensor utilizes the giant magnetoresistance (GMR) effect or the tunneling magnetoresistance (TMR) effect to detect the direction of the magnetization [8, 9]. The write element is a thin coil of wire that generates a magnetic field to flip the direction of the bits to the desired direction. Given that the size of each bit is only several nanometers, it is critical that the read/write elements be less than 5 nm from the magnetic layer to ensure accuracy. Several clever techniques are used to achieve the required spacing. The primary mechanism is the air-bearing. Although recent hard drives
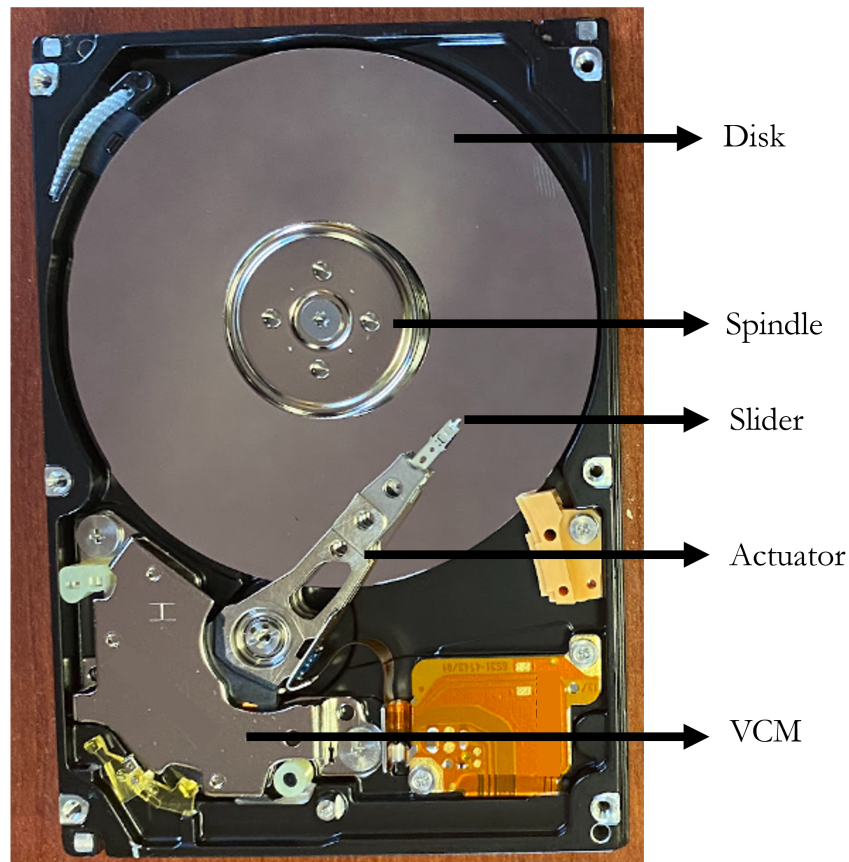
Figure 1.1: Internal view of an HDD

operate entirely in helium, we still use the term air bearings to maintain convention with literature [10]. When the disk rotates at a very high RPM (5000-10000 RPM), the boundary layer above the disk also starts moving. As the air moves under the slider, it compresses and generates lift due to a unique etching pattern on the air-bearing surface (ABS). This lift opposes the suspension load. At equilibrium, consistent spacing of several tens of nanometers is maintained between the slider and the disk. This spacing is also known as the fly height (FH) [11].

The air-bearing itself cannot reliably get the read/write elements closer than about 5 nm. Therefore, a thermal height control (TFC) is utilized to achieve the desired spacing [12]. Here, a tiny resistive heater (Joule heater) is embedded near the trailing edge of the slider (see Fig. 1.4b). The local temperature rises when a small current is applied to this heater. Due to thermal expansion, a small protrusion develops, reducing the local clearance to a few nanometers. The TFC has the added benefit that sub-5 nm spacing is achieved only near the read/write element, and the rest of the slider is further away, reducing the chances of
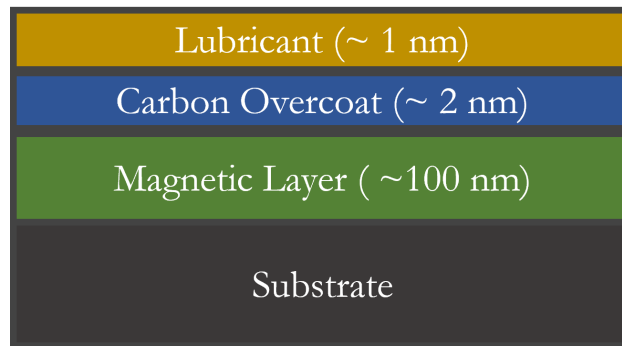
Figure 1.2: Schematic cross-section of the disk

slider-disk contact due to intermolecular forces.
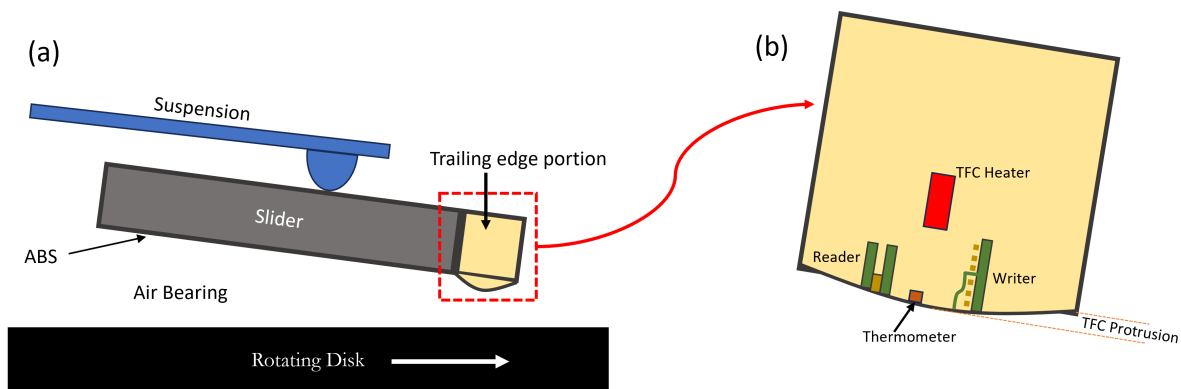
Figure 1.3: (a) Schematic view of the slider, (b) schematic view of the trailing edge portion

The movement of the slider in the radial direction is controlled by the voice coil motor (VCM) and piezoelectric micro-actuator (MA) [13, 14]. They instruct the actuator arm to the required angle, giving access to the desired radial track. Recent hard disk drives contain multi-actuator systems that act together to double the data transfer speed [15]. Since the track width can be as small as 90 nm [16], with the required control precision to be about 10% of the track width, the VCM and MA need to be within a 9 nm tolerance. Even the vibration from adjacent drives needs to be accounted for [17]. Therefore, combined with the precision in the fly height, the tolerances and dynamical stability in an HDD are genuinely astounding.

1.2   Heat-Assisted Magnetic Recording

An essential specification that tracks the development of HDDs is the areal density (AD). It is defined as the number of bits written in a unit area. Over the years, innovations have enabled the areal density to reach close to 1 Tb/in^2. Increasing AD further would cause the random thermal fluctuations to influence adjacent bits [18]. Thus, a bit would randomly flip, leading to data loss. This is known as the superparamagnetic effect [19]. Although this limit has already been reached in the last two decades, some ingenious workarounds have enabled higher capacity drives in the same form factor. Energy-assisted perpendicular magnetic recording (ePMR) [20] utilizes a current on the write pole, increasing the signal-to-noise ratio (SNR), and leading to higher AD. Another technology is shingled magnetic recording (SMR) [21], in which adjacent write tracks overlap, improving AD. Thirdly, the capacity has also increased by stacking more platters in the same form factor. In 2022, Western Digital released 10-platter hard drives that can store up to 26TB [22]. Nevertheless, all these methods are fundamentally limited by the superparamagnetic limit.

In light of this, several technologies were proposed to increase AD further. Some of them include heat-assisted magnetic recording (HAMR) [23], microwave-assisted magnetic recording (MAMR) [24], and bit-patterned recording (BPR) [25]. Among these, HAMR has emerged as the most viable and has seen considerable investment in recent years. To understand HAMR, we first look at the concept of coercivity, which is defined as the ability of a ferromagnetic material to resist demagnetization in the presence of an external magnetic field. Coercivity is measured in Amperes per meter (A/m). For instance, a neodymium magnet has a room temperature coercivity of 800 kA/m [26], whereas the typical HDD disk has 140 kA/m [27]. Therefore, the best way to increase AD is to use a material with a higher coercivity. An iron-platinum (FePt) granular media is a widely considered option with a room temperature coercivity of 2000 kA/m [28]. However, such a material poses another challenge - its coercivity makes it nearly impossible to write data using the current HDD head. But, coercivity is observed to vary with temperature. Specifically, above its Curie temperature, the coercivity drops to near zero, and the material transitions to a paramagnet. At this temperature, it is easy to write data. As seen in Fig. 1.4a, in HAMR, whenever a bit needs to be written, it is heated to near its Curie temperature. Then, it is rapidly cooled to store and read data. This forms the operating principle of HAMR [29].

The Curie temperature of FePt is between 650 and 780 K [30]. HAMR achieves this temperature with the aid of a laser. In addition to the usual elements, HAMR heads include a laser diode, a waveguide, and a near-field transducer (NFT) (see Fig 1.4b) [31]. The laser diode generates the laser, which is then transported to the underside through a tantalum pentoxide (Ta_2O_5) waveguide [32]. The diffraction limit of light prevents the laser from being focused less than the wavelength of the light. Therefore, an NFT utilizes the principle of surface plasmons. The coupling of the laser between the waveguide and the NFT excites a localized surface plasmon (LSP) that travels to the top of the NFT [33]. The NFT then couples with the magnetic layer, increasing its temperatures by several hundred degrees. Since the diffraction limit does not hinder the LSP, a several nanometers wide focused hotspot

can be formed on the disk.
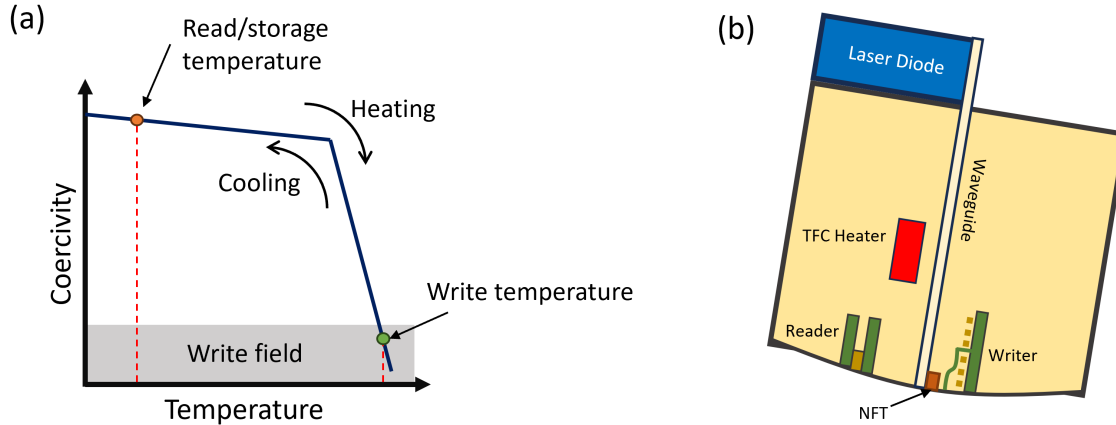
Figure 1.4: (a) Operating principle of HAMR (Inspired by Ref [29]), (b) schematic of HAMR slider's trailing edge portion (head)

1.3 Challenges in HAMR

Although HAMR was first introduced in the early 2000s [34], it has yet to see commercial success. Seagate has recently started shipping HAMR [35]; however, many specifications still need to be published, and its availability is only for select customers. The slow deployment is primarily due to the numerous reliability challenges that need to be solved [36, 37]. One specific area that remains an obstacle is the reliability of the head-disk interface (HDI). The HDI refers to the area between the head and the disk. It is subject to large optical and thermal fields. The temperatures at the disk exceed 700 K, and the temperature at the head exceeds 400 K. These temperatures can cause overheating of the various elements, leading to premature failure. The entire slider itself may crash into the disk. Further, the laser delivery process has losses, which get converted to heat energy in the head. As a result, angstrom level surface protrusions and fly height changes (FHC) can occur [38]. Furthermore, the surface plasmon from the NFT induces a huge optical field, which can also lead to unintended consequences [39]. Therefore, to build reliable HAMR drives that can last for years, it is necessary to have a fundamental understanding of the HAMR head-disk interface.

One specific reliability issue is the observation of smear in many experimental studies [40–42]. Smear is the buildup of contaminations on the head after write-operations. AFM images of the smear are shown in Fig 1.5. The study of smear is challenging as the head-disk interface is multiscale and complex. It stretches hundreds of microns in the down-track and cross-track directions but only a few nanometers in the vertical direction. The temperature

gradients exceed 10^9 K/m. The NFT forms a local protrusion [43] and induces electric field gradients exceeding 10^{16} V/m^2 [39]. The space between the head and the disk forms an air-bearing of helium or air. The combination of these fields induces phenomena such as thermal decomposition[44], thermophoresis, air shear [45], evaporation, condensation [46], and mechanical contact [47]. The disk is also composed of several materials, including iron, platinum, PFPE (perfluoropolyether) lubricants, carbon overcoats [48], etc. Therefore, the contaminants can originate from a variety of sources by a variety of mechanisms. These contaminations eventually fill up the HDI, severely limiting the lifetime of HAMR drives [36]. It can also cause flying instability of the head, leading to the premature crash of the head to the disk. Therefore, it is critical to build effective strategies to control the growth of smears.
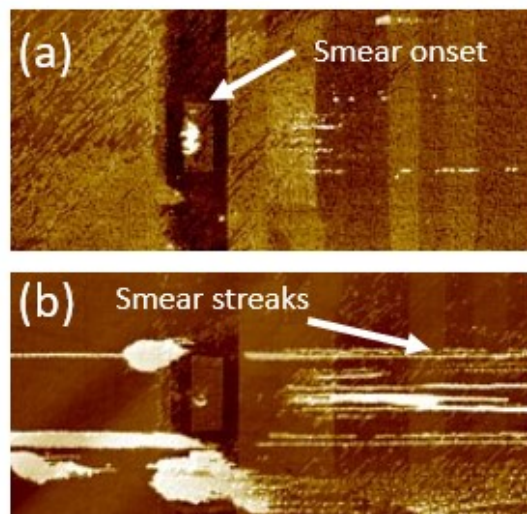
Figure 1.5: AFM images of smear [49]

Very few peer-reviewed articles have been published studying how to contain smear [50, 51]. However, due to the commercial value of reducing smear, several patents have been filed describing strategies to control smear [52–63]. The majority of these methods involve a mechanical wiping-like behavior where the head surface is brought in contact with the surface, be it the media, an entirely separate surface. The relative motions between the head and the cleaning surface wipe the smear away from the head. However, the subsequent head damage as a consequence of this procedure is not understood.

Further, several other interesting methods are proposed to reduce smear. Ref. [51] suggests using head-only heating to reverse the smear formation procedure and transfer the smear to the disk surface. This method, however, can potentially build smear on the media surface. Ref. [53] suggests using two-stage lubricant heating to remove the contaminants on the NFT surface. Ref. [62] proposes burning carbonaceous smear when the head is parked and not writing. Burning would require a significant presence of oxygen, bringing into question if the

air-bearing in HAMR would be pure helium. Ref. [64] disclosed an oxygen diffusion unit, which may suggest the possibility of a burning smear. Another interesting smear control strategy is the inclusion of a smear that does not affect or improve the head-disk reliability. Ref. [56] suggests doping the media surface with agents, and Ref. [58] suggests pretreating the NFT to allow the formation of a transparent smear. Simulations from Ref. [36] also show that highly pure SiOx contaminants can improve the plasmonic coupling between the NFT and the media. Finally, improving the quality of the head and disk material has also been a way to reduce smear. Ref. [52] developed a high-temperature lubricant from perfluoroalkyl-based polymers that may be stable at HAMR temperatures, and Ref. [60] developed a dual-layer media overcoat that reduces the operating temperature of the head-disk interface, causing less smear buildup.

Understanding the mechanism behind the growth of smear is critical in utilizing existing strategies and designing new techniques. Many numerical models have been done to simulate the growth of smear in HAMR. On one hand, many researchers have focused on modeling smear growth as a continuum solid or fluid [44, 65–69]. The viscoelastic model has found considerable attention that assumes that smear consists of PFPE lubricants [6, 68, 69]. In this model, the head and the disk were considered to have a thin-film viscoelastic fluid characterized by its thickness, viscosity, surface tension, and disjoining pressure. The thin film is governed by lubrication theory. Further, a lubricant vapor is modeled between the thin film characterized by its vapor density and governed by the continuity constraint and Fick's law of diffusion. The material transport between the phases is modeled by evaporation and condensation with rates determined by the Hertz–Knudsen–Langmuir model. However, such a continuum model has some limitations. Firstly, it is challenging to incorporate effects from different phenomena. For example, it is unknown how to integrate the impact of an electric field from the NFT into lubrication theory or the continuity equation. Second, the head-disk interface's characteristic length is in the nanometer scale, with the head-to-disk spacing being as small as 1 nm. In this scale, the molecular nature of the smear is significant. For instance, the thickness of a lubricant molecule is about a nanometer. Hence, the thickness of the lubricant as a thin film is not a continuum but takes discrete values.

Molecular dynamics (MD) has been another method to study the growth of smear or contaminations in HAMR. [70–74]. MD has primarily been used to study the decomposition and transport of the PFPE lubricant molecules. As each atom is modeled using its potential function, it exactly calculates the lubricant behavior in the disk and head surfaces and accurately tracks its trajectory in the air-bearing. Ref. [70] simulated lubricant transport from the disk to the head surface as the latter approaches the disk. It revealed the presence of a lubricant bridge held by lubricant-to-lubricant molecular forces at less than 9 nm spacing. Ref. [71] studied the thermal decomposition of D-4OH lubricant and found a two-step decomposition process. The first is the decomposition of functional end groups, which leads to the formation of H_2O molecules. The other is the decomposition of the main chain at the C-O and C-C bonds, which leads to smaller fluoroethers. Ref. [72] studied the contamination from hydrocarbon oils from other sources, such as the spindle motor and bearings. They postulated a two-step process where the air-borne molecules first condense on the disk surface before

being transferred to the head by evaporation. They also found that an existing lubricant layer on the head surface can accelerate lubricant transport. Ref. [73] further showed that the lubricant transfer from the disk to the slider decreased with increasing functional groups of the disk lubricant, decreasing the local pressure change and the disk speed. Ref. [75] studied the effects of shear on lubricant diffusion on the disk surface, finding ultra-thin lubricant undergo slipper under high temperatures. Most studies recommend using heavier lubricants with multiple end groups to reduce head smear. One major limitation of MD simulations is that they simulate short timescales, lasting around one nanosecond [72]. Since HAMR drives are expected to last several years and a single rotation of the disk lasts a few milliseconds, it is crucial to model smear over longer timescales.

1.4 Objective of this Dissertation

HAMR, the most promising technology for increasing HDDs' areal density, is approaching widespread commercialization. Its continued success depends on its reliability, especially inside the head-disk interface. This dissertation aims to study the HDI by developing numerical models that bridge the gap between continuum methods and molecular methods. We aim to do that through the following objectives.

1. Use numerical models to study the effect of the laser on the structural, thermal, and humidity characteristics of the head-disk interface.

2. Develop numerical methods to study particle-level smear transport over sufficiently long timescales.

3. Conduct parametric studies to explore the conditions where smear buildup is significant.

1.5 Organization and Novel Contributions of this Dissertation

This section presents an overview of this dissertation and highlights its novel contributions. Chapter 1 introduced the technology behind HAMR hard drives and the problem of smear.

Chapter 2 discusses the thermal and structural aspects of the head-disk interface. First, we look at the nanoscale heating of the disk to determine its temperature distribution. Then, we use nanoscale heat transfer theory to study the temperature distribution at the head. Finally, we apply classical mechanics to study the structural deformation, highlighting the laser-induced protrusion on the head.

In Chapter 3, we study the role of optical forces in the HAMR HDI. Since the surface plasmon contains very high electric and magnetic field gradients, it is expected to influence the movement of particles. Using classical electromagnetism, we calculate the optical forces.

A force-field map reveals the presence of an optical trap near the NFT. Further, we highlight the conditions in which they are significant through a sensitivity analysis.

Then, in Chapter 4, we quantify the air-bearing related forces on PFPE lubricant nanoparticles. We use the Chapman-Enskog velocity distribution to describe the helium gas-bearing. Then, we calculate the deflection of a helium atom when it strikes a PFPE nanoparticle. The net momentum transfer is integrated over all helium atoms to calculate the air-bearing forces on a PFPE lubricant fragment. The forces can be divided into drag, thermophoresis, and lift forces. The lift forces were negligible compared to the first two. Finally, a sensitivity analysis of the resulting forces revealed the conditions where each force dominates.

In Chapter 5, we propose a hybrid simulation strategy to simulate the growth of smear nanoparticles. Using the forces developed in chapter 4, we create a force field in the air-bearing. Then, we assume that the van der Waals force holds the PFPE lubricant particles on the disk. Subsequent heating of the disk causes the particles to evaporate from the disk and condense on the head. The density map of the nanoparticles on the head is plotted as smear patterns. The results show the first numerical simulation replicating the smear streaks observed on HAMR heads.

In Chapter 6, we study the air-bearing inside the HAMR HDI under ultra-low spacing and temperature hotspots. First, we introduce the direct simulation Monte Carlo (DSMC) method; then, we apply the consistent Boltzmann algorithm (CBA) to account for the non-ideal gas effects. A 2D channel with a thermal spot containing temperature gradients in the horizontal and vertical directions represents the air-bearing under HAMR conditions. The results show the presence of a gradient in the air bearing and density due to the vertical gradient. Further, the humidity levels at the interface were observed to be much higher than what was possible in CMR drives.

Chapter 7 proposes the presence of ballistic jumps in ultra-low spacing conditions. The underlying phenomenon is the uneven temperature-dependent van der Waals forces between the head and disk surfaces. The simulation indicates that under 2 nm of spacing, the contaminants can be picked up by the relatively cooler head.

Finally, in Chapter 8, we conclude the dissertation by summarizing the results from all the chapters. Then, we offer some strategies to aid in smear mitigation. Finally, we discuss ways to extend this research.

Chapter 2

Structural and Thermal Study of the HDI

2.1   Introduction

The head-disk interface (HDI) in heat-assisted magnetic recording (HAMR) hard disk drives is very complex due to the additional elements near the trailing edge, as shown in Fig. 1.4b. In this chapter, we apply the equations of heat transfer and solid mechanics to calculate the temperature distribution and the structural deformations due to the presence of the laser, waveguide, and near-field transducer (NFT). After Sec. 2.1 introduces the chapter, Sec. 2.2 describes the numerical model used to simulate the temperature and displacement of the head-disk interface. Then, Sec. 2.3 explains the various simulations and results. Finally, Sec. 2.4 discusses and concludes the results from the chapter.

2.2   Numerical Model

2.2.1   Disk Thermal Model

In order to write data on the magnetic layer, the disk needs to be heated to the Curie temperature (700 K). The rise in temperature and subsequent changes are not instantaneous and are possibly gradual curves. Since the disk is not stationary, we employ the classical transient heat conduction (THC) equation to calculate the disk temperature profile. If T and u are the temperature and velocity of a body, the THC equation is given by:

$$\rho C \left(\frac{\partial T}{\partial t} + u \cdot \nabla T \right) = \nabla(\kappa \nabla T) + q_{gen} \tag{2.1}$$

where ρ, C, and κ are the density, heat capacity, and thermal conductivity of the material, respectively. The term q_{gen} accounts for volumetric heat sources. Our simulation occurs in the frame of the disk ($u = 0$), from where the laser moves at a constant velocity. We assume

the surface laser heat flux is Gaussian in distribution with a given peak intensity (l_p) and a full-width half maximum (FWHM, l_d). Then, the intensity at a given point is,

$$I = l_p \exp(-\frac{r^2}{l_d/(2\sqrt{\log 2})}) \tag{2.2}$$

with r being the distance of the point from the center of the hotspot. The model indicated that typical values of l_p to maintain 800 K peak temperature was in the order of 10^{12} W/m^2 for a 30 nm laser and 10^{10} W/m^2 for a 300 nm laser. Since the laser is supposed to heat a nanoscale spot instantaneously, we assume that the temperature far from the center of the hotspot is room temperature. Therefore, we only simulate the area near the hotspot. The simulation box (Fig. 2.1) is rectangular, with dimensions proportional to the laser FWHM (l_d). Specifically, $80l_d$ in the down-track direction, $32l_d$ in the cross-track direction, and $6l_d$ in the direction of propagation (vertical direction). The domain was discretized into 24000 10-node tetrahedral elements using a Delaunay triangulation. The mesh size along the path of the laser was refined to capture the hotpot accurately. Then, a time semi-discretization FEM code was programmed in MATLAB to calculate the temperature distribution at a given time. Since we expect the temperature to be near room temperature in areas far from the hotspot center, a Dirichlet boundary condition (BC) was imposed on the lateral faces with $T = 300$ K. At the bottom face, a heat sink was simulated using a Neumann boundary condition (BC) with an effective heat transfer coefficient, $h_f = 100$ W/m^{2}K. Our analysis showed that the choice of the heat transfer coefficient did not significantly impact the trends in this simulation. The expressions for the finite element discretization and solution procedure are recorded in appendix A.

From Eq 2.1, we see that material parameters that can influence the temperature distribution are thermal conductivity, heat capacity, and density. The operational parameters are the linear laser velocity (u) and the laser heat flux (Eq 2.2). Since the disk material and operational parameters are not accurately known, we consider a range of possible values as tabulated in Table 2.1.

To maintain uniformity between simulations, the peak power is chosen such that the peak temperature is 800 K. The laser/disk linear velocity is taken to be between 5 m/s (corresponding to the inner diameter of the disk at 5400 rpm) and 50 m/s (corresponding to the outer diameter of the disk at 10000 rpm). The baseline velocity is 25 m/s, midway between the extremes. The FWHM can take two values: 30 nm or 300 nm. The smaller value of 30 nm is representative of HAMR operating conditions[76], whereas the larger value of 300 nm is seen in some experiments conducted without an NFT [77]. Since the density and heat capacity appear together in Eq 2.1, we combine the terms as $\rho C = C_v$ in our simulations. C_v is the effective heat capacity per unit volume [78]. The density of the disk can range from 2000 kg/m^3 (for PFPE lubricants) to 15000 kg/m^3 (for FePt nanoparticles [79]). The baseline value is taken to be 10000 kg/m^3 as most disk material components are metallic. C_v for the recording layer is around 3×10^6 J/m^{3}K. The thermal conductivity is different in the out-of-plane and in-plane directions [80]; however, for the sake of simplicity, we assume the material is isotropic. The thermal conductivity for FePt media has been reported to be as
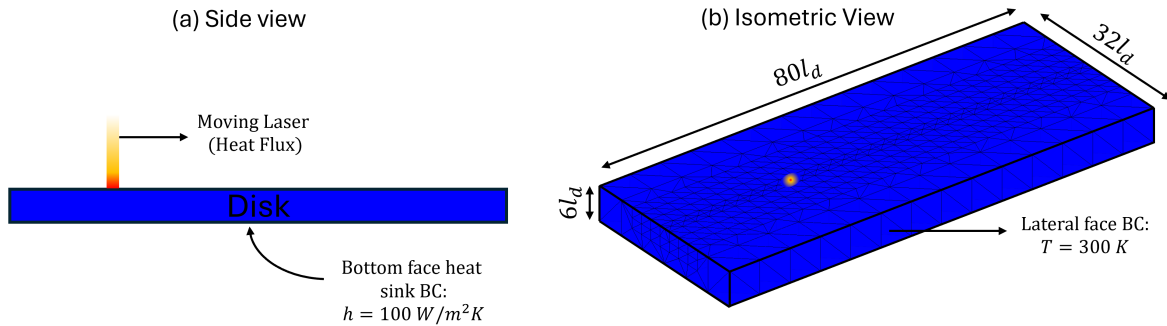
Figure 2.1: Schematic of the disk simulation domain. (a) Side view, (b) isometric view. The laser spot size is enlarged, and only two levels of mesh refinement were plotted for better visibility

low as 6 W/mK [81], whereas the other media materials, such as the DLC layer, can have thermal conductivity up to 1000 W/mK [82]. The baseline value is taken to be 15 W/mK.

Table 2.1: Material parameters to solve transient heat conduction equation

Parameters	Minimum	Maximum	Baseline
Effective heat capacity	2 J/cm^{3}K	4 J/cm^{3}K	3 J/cm^{3}K
Thermal conductivity	5 W/mK	1000 W/mK	15 W/mK
Laser (disk) velocity	5 m/s	50 m/s	25 m/s
FWHM	30 nm	300 nm	30 nm

2.2.2   Head Thermal and Mechanical Model

The HAMR head is composed of numerous components, encompassing both sizable elements like the waveguide and laser diode, as well as more nanoscale features such as the NFT and the read-write sensors. The inclusion of the laser causes significant changes in its thermal and structural characteristics. In this section, we aim to quantify the temperature rise on the surface of the head and the associated deformations.

Heat sources

There are three sources of heat in a typical HAMR head. The first is due to the TFC heater, which is responsible for the TFC protrusion [83]. If a voltage (V) is applied across a TFC heater with known resistivity, then the heat generated per unit time per unit volume is given by

$$q = \frac{1}{\rho}\nabla V \cdot \nabla V \tag{2.3}$$

where ρ is the resistivity of the material. In the case of a conventional HDD, the temperature rise is between 30-50 K.

The second heat source is due to the losses in the laser delivery system. It encompasses the losses incurred during the laser's propagation through the waveguide, the coupling losses between the waveguide and the NFT, and the losses occurring at the tip of the NFT. The intensity of the laser in the waveguide as a function of distance (x) is given by:

$$I = I_0 e^{-4\pi k(\lambda)x/\lambda} \tag{2.4}$$

Where λ is the wavelength of the laser and $k(\lambda)$ is the extinction coefficient as a function of the wavelength. The waveguide is made of tantalum pentoxide (Ta_2O_5), whose extinction coefficient is less than 2×10^{-6} for laser wavelengths greater than 600 nm [84, 85]. Since HAMR uses a laser wavelength of approximately 800 nm[86], the intensity along the waveguide can be calculated by,

$$I = I_0 e^{3.1416\times 10^{-5}x} \tag{2.5}$$

Where x is in microns. The thickness of a slider is less than about 250 μm, so the net loss of intensity is less than 1%. Therefore, we ignore this loss. The other losses occur near the NFT when the laser couples with it or exits from the end of the waveguide. The design of the NFT and its coupling characteristics is very complex; therefore, we will approximate this coupling loss with a fixed heat across a volume comparable to the NFT. Experiments [51] have shown that no laser is emitted from the waveguide when the laser has less than 13 mW power, suggesting that around 13 mW is lost as heat energy.

The third source of heat is due to the back-heating from the disk to the head. [87, 88]. The head-disk spacing can be as low as 1 nm, and given that the disk heats up to 800 K during writing, heat transfer occurs between the head and the disk. Four heat transfer mechanisms exist - air conduction, viscous dissipation, phonon conduction, and radiation [88]. We ignore the radiative and viscous dissipation, as they are insignificant compared to the others. The net heat transfer coefficient (HTC) is then,

$$htc_{net} = htc_{air} + htc_{phon} \tag{2.6}$$

The contribution of air conduction can be calculated using temperature jump theory [89, 90]. It mainly depends on the thermal conductivity of air, head-disk spacing, and mean free path

of the air-bearing (which then depends on the pressure). The equation for the heat transfer coefficient is given by:

$$htc_{air} = \frac{\kappa_{air}}{h + 2\frac{2-\sigma_T}{\sigma_T}\frac{2\gamma}{\gamma+1}\frac{1}{\text{Pr}}\lambda_{air}} \tag{2.7}$$

where κ, h, σ, γ, Pr, λ are the thermal conductivity, fly height, thermal accommodation coefficient, ratio of specific heats of air, Prandtl number, and the mean free path of air, respectively. The contribution of phonon conduction can be modeled using wave-based phonon conduction theory [91–93]. An empirical model reveals that it depends on the head-disk spacing, disk temperature, and the head-disk temperature difference [94]. It is given by:

$$htc_{phon} = c_1 \ln(h) + c_2 \ln\left(\frac{T_d - T_s}{400}\right) + c_3 \ln\left(\frac{T_d}{298}\right) + b \tag{2.8}$$

where c_i are coefficients that fit the numerical data. They depend on density, wave speed, and Debye-frequencies of the head and disk. T_d and T_s are the disk and slider temperatures, respectively. An explanation of the nanoscale heat-transfer theory is summarized in Ref [88].

Simulation strategy

We employ the simulation approach established by Sakhalkar et al. [88, 94, 95] for determining the necessary fields. The temperature distribution and structural deformations on the head are contingent on the fly height and pressure distribution, while conversely, the fly height and pressure distribution hinge on the structural deformations of the head. Given this interdependence, an iterative method becomes essential. A visual representation of this methodology is illustrated in Fig. 2.2. The fly height and pressure can be computed using CML Air (Sec. 2.2.2), while the temperature distribution and structural deformations can be resolved through a finite-element solver (2.2.2).
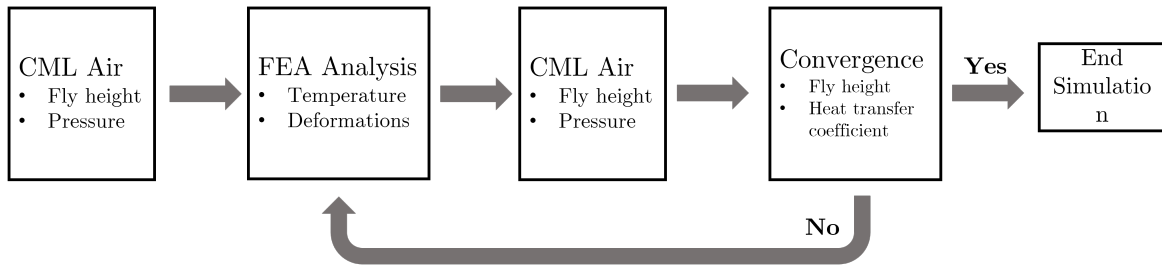
Figure 2.2: Schematic of the iterative procedure to calculate the head temperature and structural deformation [6]

CML Air

CML Air is a software developed at the Computer Mechanics Lab, UC Berkeley, that solves the generalized Reynolds Equation with the Fukui–Kaneko slip correction[96]. It uses Patanker's control volume method with a multigrid solver. The software receives the ABS surface etching and surface protrusions to calculate the steady-state flying height pressure distribution. Since the back-heating from the disk to the head depends on the heat transfer coefficient (HTC), which in turn depends upon the spacing and head-disk forces, we use the output from CML Air to calculate the required HTC.

Slider thermo-mechanical model

A thermo-mechanical finite element code was developed in MATLAB to calculate the temperature and displacement fields on the slider. The code receives various heat sources described in Sec 2.2.2 as inputs to a thermal solver that calculates the temperature field. A structural solver uses this temperature field as input to calculate the displacement field. A schematic of the model with the forces are shown in Fig. 2.3. The FEM solution procedure and associated matrices can be found in Appendix A
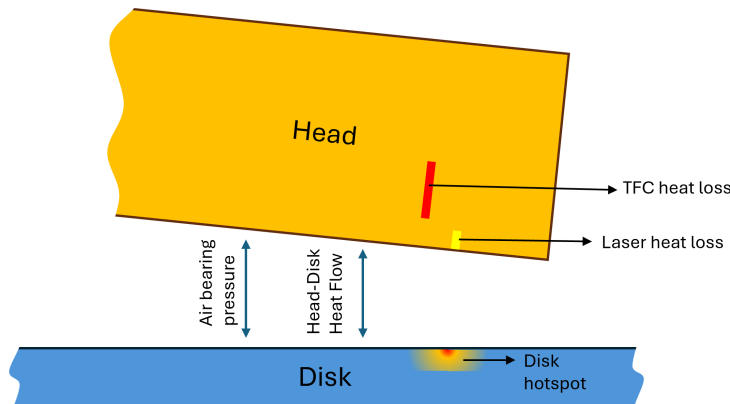
Figure 2.3: Schematic of head-disk thermo-mechanical model with the forces and heat sources

The slider is an orthogonal block with dimension $843.5 \times 700 \times 230 \mu$m. The leading side is made of aluminum-titanium-carbide (AlTiC) [97]. and the trailing portion is made of Al_2O_3 [88]. Due to the difficulty in modeling the dimension of the read and write sensors, we will group them as a single block of dimension $25 \times 30 \times 35$ μm in the trailing portion and flush with the ABS. The material parameters are taken as the average of the read and write sensor properties taken from Ref. [98]. The TFC heater is embedded as a block $0.1 \times 22 \times 4.5$ μm

above the read-write elements. Since the concept of a TFC heater arose from the heating of the write element [99], we assume that it is made of copper, the same or similar material as the write coil [98]. The NFT heating element is a smaller block with dimension $0.3 \times 0.6 \times 0.2$ μm near read-write elements and flush with the ABS. It is made of gold. A 10-node tetrahedral mesh was constructed in ANSYS and exported to MATLAB for analysis. The mesh was refined near the read-write elements and the heat sources to ensure the grid independence of the solution. The material parameters of the materials are listed in Table 2.2.

Material	**E** (GPa)	ν	$\alpha(\times 10^{-6})$/K	κ (W/mK)
AlTiC [98]	390	0.22	7.1	20
Al2O3 [98]	138	0.25	7.1	1.8
TFC heater [98]	130	0.34	15.4	403
Read-write elements [98]	170	0.32	14.1	220
NFT (Au) [100]	70	0.42	14	100 [101]

Table 2.2: Material parameters for thermo-mechanical finite element analysis. **E** is the Young's modulus, ν is the Poisson ratio, α is the coefficient of thermal expansion, and κ is the thermal conductivity.

The thermal analysis solves the steady-state version of the transient heat-conduction equation (Eq 2.1), given by:

$$\nabla(k\nabla T) = -q_{gen} \tag{2.9}$$

The convection coefficient on the lateral surfaces were 100 W/m^{2}K and 2000 W/m^{2}K on the top surface. The higher value on the top surface was due to the attached metal suspension. The ambient pressure and temperature were 298 K and 101325 Pa, respectively. Finally, on the ABS, the nanoscale heat transfer theory was applied to calculate the heat transfer coefficient.

The structural analysis solves the static structural deformation equations in the absence of body forces given by:

$$\nabla \cdot \boldsymbol{\sigma} = 0 \tag{2.10}$$
$$\boldsymbol{\epsilon}_{th} = \alpha \nabla T \tag{2.11}$$
$$\boldsymbol{\sigma} = \boldsymbol{D}(\boldsymbol{\epsilon} - \boldsymbol{\epsilon}_{th}) \tag{2.12}$$

where $\boldsymbol{\sigma}$, $\boldsymbol{\epsilon}$, $\boldsymbol{\epsilon}_{th}$ and $\boldsymbol{D}$ are the Cauchy stress tensor, total strain tensor, thermal strain tensor, and the elastic stiffness matrix, respectively. Equation 2.10 is Cauchy's first law, Eq 2.11 is the linear expansion equation, and Eq 2.12 is the constitutive relationship. The pressure field was applied as a force on the bottom side of the slider. Finally, to enforce a boundary condition, the displacement at the two top corners near the leading edge was set to zero, and the top of the slider was constrained in the vertical direction.

2.3 Simulation Results

2.3.1 Disk Temperature

In the first simulation, we investigate the temperature profile when the velocity of the laser is varied (Fig 2.4). The approximate power required to maintain 800 K at 30 nm Laser FWHM is tabulated in Table 2.3. In the case when the laser FWHM is 30 nm, the heating occurs, and it roughly takes the same time as the cooling. Also, the slower disk is observed to have a more gradual cooling when the temperature is less than 350 K, but where the temperature is greater than 500 K, the results are nearly identical. In all three cases, a Gaussian fit seems to be quite suitable. On the other hand, in the case of a large FWHM, there is an asymmetry in the heating and cooling regions, with the former being much shorter. Nevertheless, this asymmetry is observed only when the temperature is less than 350 K. Since HAMR requires a rapid heating and cooling period, it is beneficial for the disk to operate at high RPM.
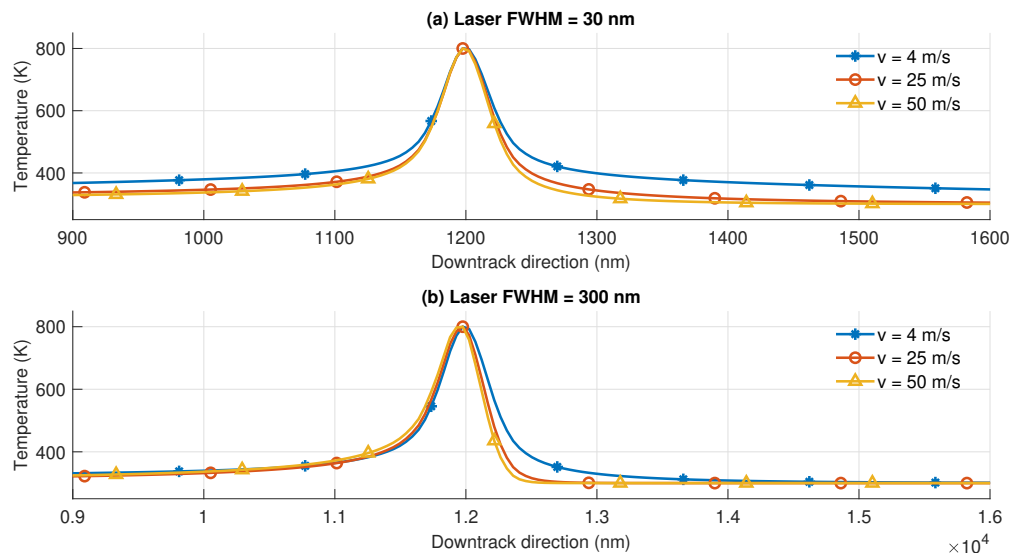
Figure 2.4: Variation of disk temperature at different laser velocities for (a) FWHM = 30 nm, and (b) FWHM = 300 nm

Parameters	30 nm FWHM	300 nm FWHM
v = 4 m/s	0.4398 mW	5.0684 mW
v = 25 m/s	0.4923 mW	6.0910 mW
v = 50 m/s	0.5142 mW	7.0905 mW

Table 2.3: Output power required to maintain an approximate 800 K peak temperature at various disk velocities

In the second simulation, we investigate the role of thermal conductivity. Three cases, ($\kappa = 5, 15, 1000$ W/mK) are plotted in Fig 2.5. The required power to maintain 800 K is tabulated in Table. 2.4 We observe similar results for each FWHM as earlier. We note that the temperature gradient is inversely proportional to thermal conductivity. Therefore, rapid cooling requires materials with low thermal conductivity [102].
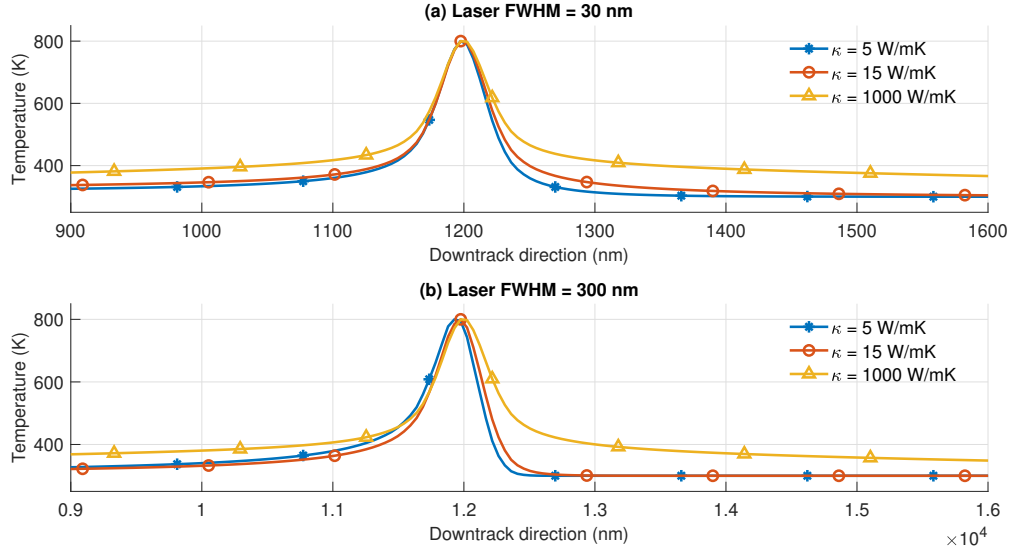
Figure 2.5: Variation of disk temperature at different disk thermal conductivity for (a) FWHM = 30 nm, and (b) FWHM = 300 nm

Parameters	30 nm FWHM	300 nm FWHM
$\kappa = 5$ W/mK	0.1765 mW	2.6477 mW
$\kappa = 15$ W/mK	0.4923 mW	6.0915 mW
$\kappa = 1000$ W/mW	28.2041 mW	292.2590 mW

Table 2.4: Output power required to maintain an approximate 800 K peak temperature at various disk thermal conductivities

In the third simulation, we investigate the role of the effective heat capacity of the disk in the disk temperature profile. The results are plotted in Fig. 2.6. The required power is tabulated in Table. 2.5. We do not observe any difference in the range considered. From the three simulations, we observe that in the case of a small laser size, a Gaussian temperature distribution is sufficient to describe the temperature distribution on the disk accurately. Furthermore, a two-term Gaussian distribution can represent the results for larger laser sizes.
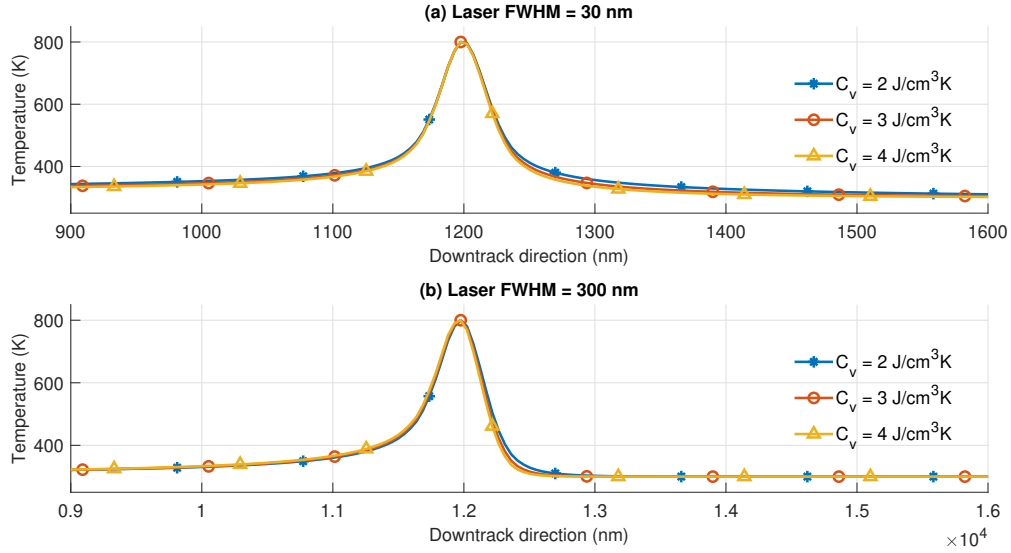
Figure 2.6: Variation of disk temperature at different disk specific heat capacity for (a) FWHM = 30 nm, and (b) FWHM = 300 nm

Parameters	30 nm FWHM	300 nm FWHM
$C_v = 2$ J/cm³K	0.4800 mW	5.7313 mW
$C_v = 3$ J/cm³K	0.4923 mW	6.0908 mW
$C_v = 4$ J/cm³K	0.5011 mW	6.4361 mW

Table 2.5: Output power required to maintain an approximate 800 K peak temperature at various disk heat capacities

2.3.2 Head Temperature

The temperature profile on the head was computed at 35 mW TFC power and a 30 mW power loss resulting from the waveguide-NFT coupling. The resulting temperature distribution is shown in Fig. 2.7. For reference, a case without any waveguide-NFT coupling loss is also included. A distinct temperature spike is evident in all three plots, reaching approximately 150 K for a 30 mW power loss. This spike spans about 5 microns in the down-track direction, corresponding to the mean dimension of the waveguide-NFT coupling element. Notably, the distribution in the down-track direction is asymmetric, as at $x = 843$ μm, the trailing edge-air boundary exhibits a lower thermal conductivity, leading to more heat retention on the trailing side. The AlTiC section, on the other hand, acts like a heat sink [98]. In the cross-track direction, a symmetric temperature distribution is observed with a spike at the center. Additionally, between 330 and 370 μm, a temperature jump can be seen, which is because of the higher thermal conductivity of the effective read-write sensor element.
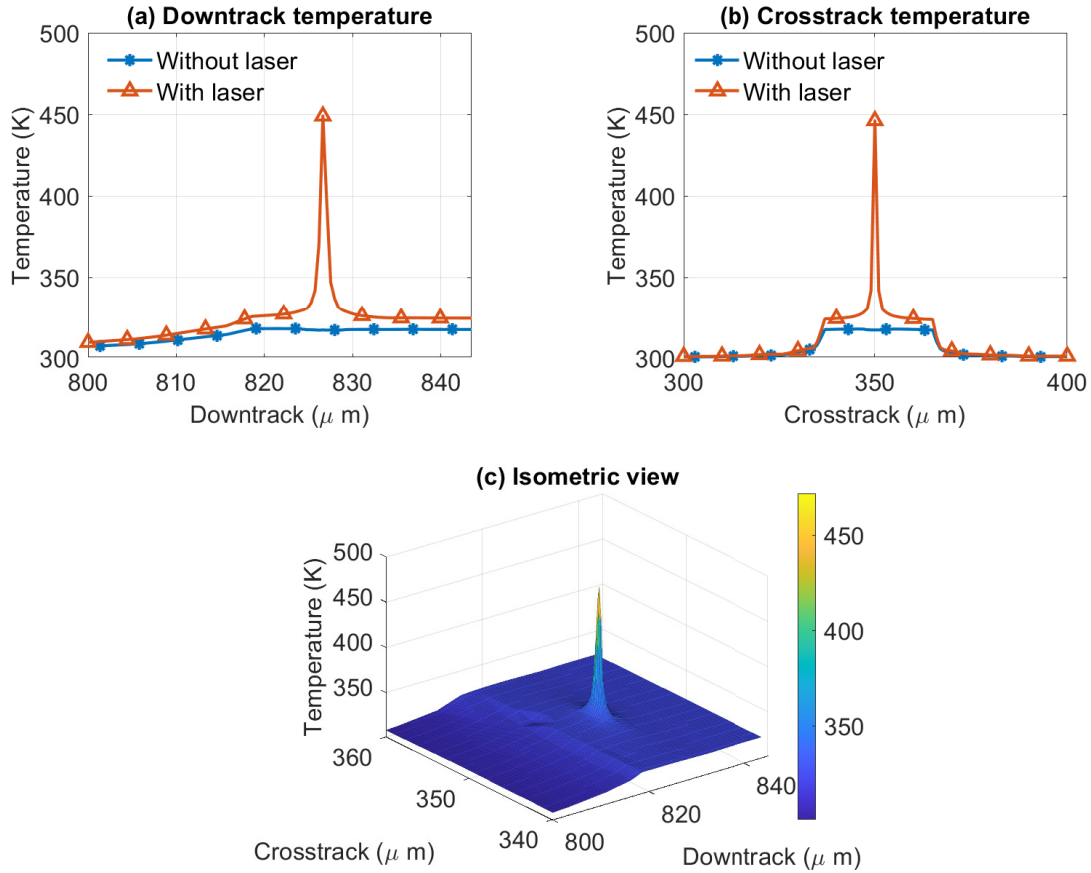
Figure 2.7: Head temperature distribution (a) Along the down-track direction, (b) Along the cross-track direction, and (c) An isometric 3D view

2.3.3 Head Protrusions

Similar to the temperature calculations, the deformations on the head were computed at 35 mW TFC power and a 30 mW power loss from the waveguide-NFT coupling. The structural deformations are graphically represented in Fig. 2.8. A reference condition without any Waveguide-NFT heat loss is also plotted. Due to the rise in temperature, a protrusion is developed near the read-write sensor [103], which enables a further reduction in minimum fly height. In the case with only the TFC heater (no laser), the maximum protrusion is approximately 9Å (represented by the blue/star curve). Moreover, within the depicted range in Fig. 2.8a, the protrusion consistently exceeds 4Å. When we compare the case with the laser (represented by the red/triangle curve), two distinctions become apparent. Firstly, there is a noticeable protrusion, known as the laser-induced protrusion (also known as the

NFT protrusion [104] or angstrom level protrusion [43]) in the vicinity of the laser heat loss element, exhibiting a local elevation of approximately 1 to 2 Å. This can be attributed to the temperature spike depicted in Fig. 2.7a-c. Since the area over which the temperature spikes in Fig. 2.7a is small compared to the TFC heating, the magnitude of the protrusion is small. Secondly, throughout the entire plot range, the latter consistently maintains an additional 1 to 2 Å protrusion. This contrasts with Fig. 2.7a, where the temperature difference away from the NFT was negligible. Therefore, the laser heating element *enhances* the TFC protrusion even without a corresponding temperature rise. The protrusion exhibits an asymmetrical nature analogous to the head temperature, which arises from distinct boundary conditions at both ends.
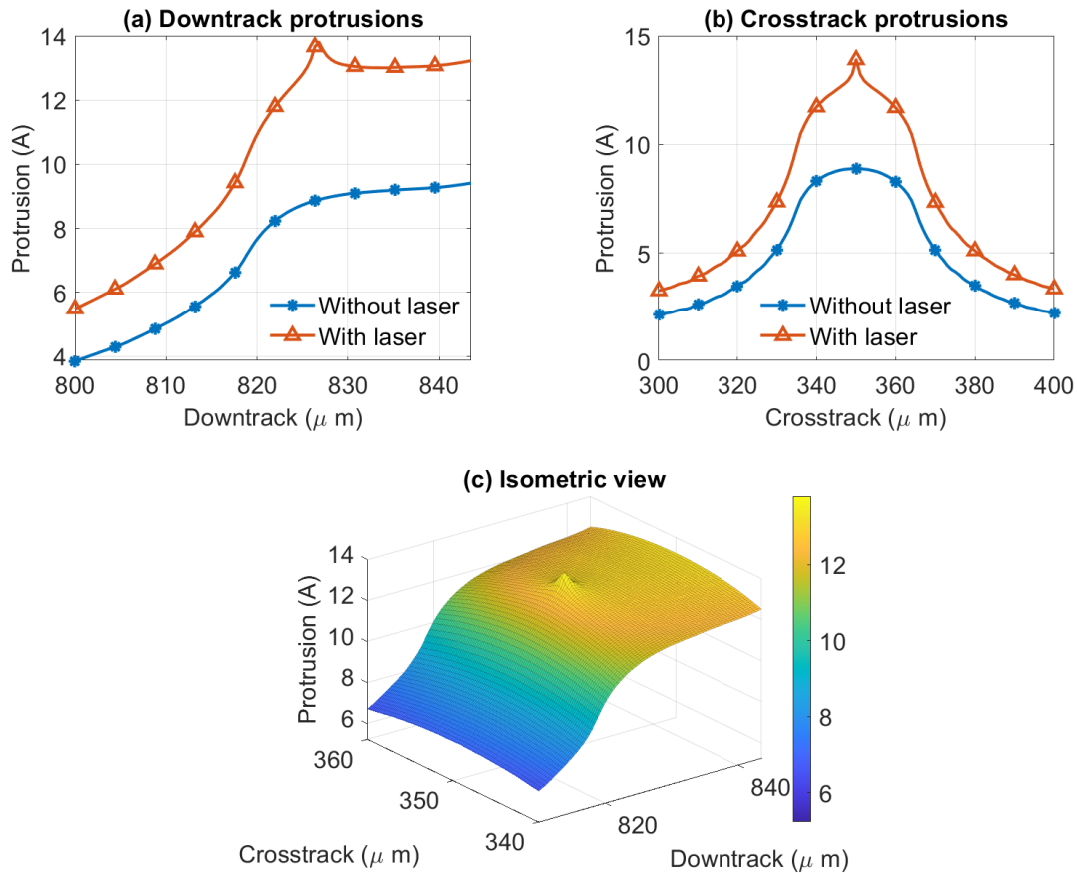
Figure 2.8: Head protrusion distribution (a) along the down-track direction, (b) along the cross-track direction, and (c) an isometric 3D view

The peak protrusion with the laser exceeds 1 nm as Fig. 2.8a-b shows. This is relevant, considering the minimum fly height can be as low as 1 nm. Therefore, the heat loss from the

laser can significantly impact the flying characteristics. Further, since HAMR requires tight spacing controls to write data accurately, it is essential to look at the factors that influence laser-induced protrusion carefully. Several parameters are important in studying the thermal characteristics of the head-disk interface. This chapter will look at the TFC power and the disk linear velocity.

2.3.4 Effect of TFC Power

We begin by examining the dependence of the TFC power on the maximum laser-induced protrusion (LIP) and the peak head temperature. For a given TFC power (P_{TFC}) and laser heat loss (LHL) power (P_{LHL}), the LIP and the peak head temperature (T_h) are given by

$$\text{LIP} = \max\left(\text{Prot}_{P_{TFC}, P_{LHL}}\right) - \max\left(\text{Prot}_{0, P_{LHL}}\right) \tag{2.13}$$

$$T_h = \max\left(T_{P_{TFC}, P_{LHL}}\right) - \max\left(T_{0, P_{LHL}}\right) \tag{2.14}$$

where $\text{Prot}_{a,b}$ and $T_{a,b}$ are the protrusion and temperature for the parameters a and b, which refer to the TFC power and the LHL power.
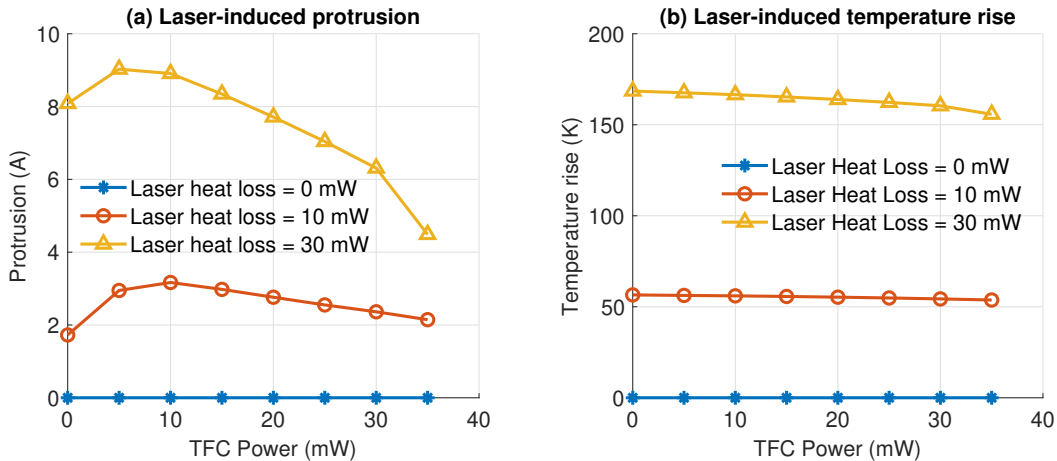
Figure 2.9: (a) The dependence of the laser-induced protrusion (LIP) with TFC power at three different laser heat losses. (b) Dependence of peak head temperature with TFC power

The results are plotted in Fig. 2.9. First, we observe that for a given LHL, the rise in head temperature (Fig. 2.9b) does not vary with TFC power. This suggests that the temperature contribution may be decoupled from the disk temperature. However, this is valid only if the heat loss mechanism can be described as a resistive heater. In a real HAMR head, the heat loss mechanism is much more complicated and may require advanced analysis. We can also observe interesting results in the case of the head protrusion. In Fig. 2.9a, at low TFC powers, the LIP monotonically increases with increasing TFC power. However,

after TFC power of roughly 10 mW, the LIP gradually decreases with increasing TFC power. Essentially, a peak is observed around 10 mW TFC power. In the case of $P_{LHL} = 30$ mW, the peak is about 2 Å. At about 40 mW TFC power, the LIP returns to the value without TFC power. The initial increase occurs due to the way the TFC Heater influences the boundary condition near the NFT. In contrast, a higher TFC power decreases the head-disk spacing, leading to an enhanced head-to-disk heat transfer, causing a smaller protrusion.

2.3.5 Effect of Disk Rotation Speed

The disk in hard drives has been designed to spin between 5400 to 10000 revolutions per minute (RPM). The operational RPM of HAMR drives is not public. Nevertheless, since the simulation is done at the micrometer level, the linear speed, as observed from the slider, is more relevant. Since the slider can fly over the inner and outer radii of the disk, the disk speed will play a crucial role in the flying characteristics of a hard drive. In this study, we studied how the disk rotation speed (or linear speed) can influence the head temperature and protrusion. Using a procedure similar to those in Sec. 2.2, we plot the distributions in Fig. 2.10. The results clearly show that the influence of RPM on the head protrusion is negligible. Even in the case of 30 mW laser heat loss, the difference between the 5400 and 10000 RPM is less than 1 Å.
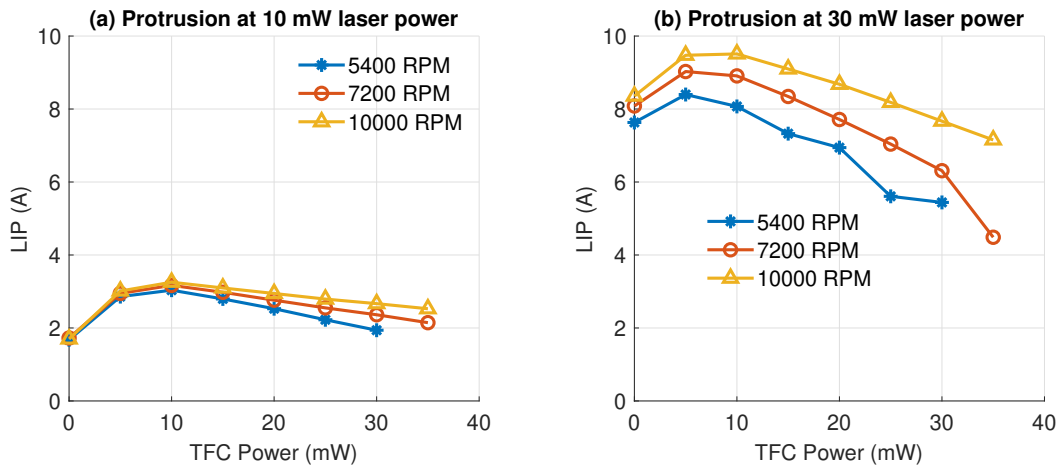
Figure 2.10: The dependence of the laser-induced protrusion (LIP) with TFC power at various RPM. (a) Laser heat loss = 10 mW (b) Laser heat loss = 30 mW

2.4 Conclusions

In this chapter, we presented models to describe the thermal and structural characteristics of the head-disk interface. Classical heat transfer and solid mechanics equations are used to calculate the temperature and displacement profiles. The results give us insight into the factors that influence HAMR reliability. First, we saw the existence of very high temperatures on the head and disk surfaces, and with it, there is a more significant temperature gradient exceeding 1×10^9 K/m. A parametric analysis revealed that the temperature distribution on the disk surface is largely unaffected by the variations over the parameters we analyzed. This is promising since it will allow flexibility to tune these parameters for head stability without compromising the disk temperature distribution. However, extreme material properties, as well as material anisotropy, may influence the disk temperature.

The head temperature rise was estimated to be around 150 K due to the laser coupling losses. This is significantly higher than conventional hard disks with just a TFC. Therefore, efficient waveguide-NFT coupling with an efficient heat dissipation mechanism is vital to prevent damage to the write coil. The protrusion that develops as a consequence is not as pronounced as the temperature spike. Examining the laser-induced protrusion with the TFC power revealed a coupling between the waveguide-NFT system and the TFC heater. This increases the TFC protrusion by at least 1Å, implying that a lower TFC power is needed to maintain the minimum fly height. Finally, we saw that the LIP is largely unaffected by the disk velocity. It is also important to recognize the relative magnitude of the protrusion with respect to the down-track direction in Figs. 2.8, 2.10 and 2.9. The slope of the surface is practically zero. Although these protrusions affect the flying behavior, the relative magnitude of the protrusion in comparison to the horizontal (down-track) direction is not significant. Therefore, we ignore the protrusion in the rest of the dissertation and focus only on the temperature spike.

Chapter 3

Optical Forces on Smear Nanoparticles

3.1 Introduction

In his seminal work, Arthur Ashkin [105] showed that a focused laser beam could trap a microscopic particle due to an optical force. This force forms the basis of optical tweezers. Further, in the last few decades, this theory has been extended to break the diffraction limit of light through plasmonic tweezers [106], which utilize surface plasmon polaritons (SPP) and localized surface plasmon resonance (LSPR). We know that the NFT generates a strong optical field in the head-disk interface by the excitation of a localized surface plasmon [33]. The magnitude of the electric field is about 7×10^7 V/m [107] with a gradient of 5×10^{16} V/m^2. Although multiple investigations have focused on the temperature-related mechanism driving the formation of smear [65, 69, 108, 109]; however, to our knowledge, no study has yet considered the effects of the electric field gradient. It is possible that the head-disk interface can act as a plasmonic tweezer that traps smear particles. Therefore, in this chapter, we look into the impact of this electric field gradient on smear formation. Using suitable theoretical assumptions, we will quantify the optical forces. Then, we will compare the magnitude of these forces with the drag and thermophoretic force for a spherical and ellipsoidal nanoparticle to show the relative significance of the optical trap. The results suggest the presence of an optical trap that can influence smear formation. A sensitivity analysis of the relevant parameter space indicates that the smear nanoparticle properties and shape significantly affect the optical force. Additionally, we find that a lower head-disk interface spacing and the presence of foreign contaminants can aid the optical force mechanism of smear formation. Finally, we summarize the results.
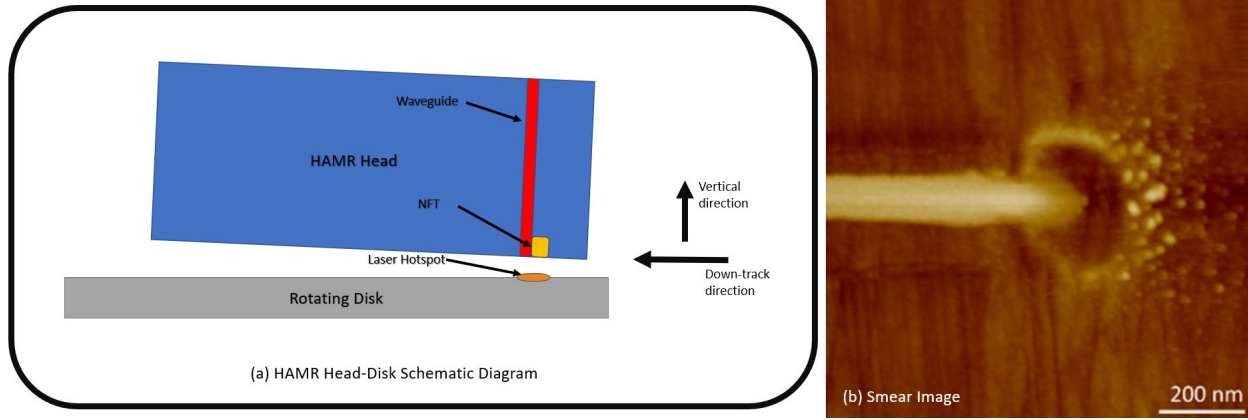
Figure 3.1: (a) Schematic view of the HAMR head-disk assembly (Not to scale). Two directions are also shown relative to the head. The down-track direction is along the circumferential direction on the disk, and the vertical direction is perpendicular to it. The cross-track direction is along the width of the head and into the plane of the schematic (b) Experimental image of smear on the head after HAMR writing.[110]

3.2 Derivation of Forces

3.2.1 Optical Forces

We begin by assuming that the fundamental smear unit is a particle. This simplifies our analysis as we investigate the force field experienced by the particle at a given position in the head-disk interface. The average electromagnetic force on a particle is determined by the electric and magnetic fields at a closed surface that envelops the particle[111]. The force on the particle can be written as:

$$\langle \boldsymbol{F} \rangle = \left\langle \oint_s \boldsymbol{T} \cdot \boldsymbol{n} ds \right\rangle \tag{3.1}$$

$$= \oint \left\{ \frac{\epsilon}{2} \mathrm{Re} \left[(\boldsymbol{E} \cdot \boldsymbol{n}) \boldsymbol{E}^* \right] - \frac{\epsilon}{4} (\boldsymbol{E} \cdot \boldsymbol{E}^*) \boldsymbol{n} + \frac{\mu}{2} \mathrm{Re} \left[\mu (\boldsymbol{H} \cdot \boldsymbol{n}) \boldsymbol{H}^* \right] - \frac{\mu}{4} (\boldsymbol{H} \cdot \boldsymbol{H}^*) \boldsymbol{n} \right\} ds \tag{3.2}$$

where $\boldsymbol{E}$ and $\boldsymbol{H}$ are the electric and magnetic fields, respectively. μ and ϵ are the relative permeability and the relative permittivity of the surrounding medium, respectively. $\boldsymbol{T}$ is Maxwell's stress tensor, $\boldsymbol{n}$ is the unit normal perpendicular to the integral area ds. The integral is over a surface that encloses the particle. Solving this equation yields two components of force. One is the scattering force, and the other is the optical force [111]. The former points along the in-plane k-vector (that is, along the direction of propagation). It is also known as radiation pressure. In contrast, the optical force is along the electric field gradient vector and is responsible for the optical/plasmonic tweezers effect.

Calculating Maxwell's stress tensor and the subsequent integration is very difficult to implement and requires lengthy computations. Therefore, we use a suitable approximation to derive a closed-form equation. When the particle size is sufficiently smaller than the wavelength of light, the dipole or Rayleigh approximation is invoked. The particle is approximated as a point dipole acting on an external electric field. The scattering and optical forces under this assumption are given by [111, 112]:

$$\boldsymbol{F}_{scattering} = \frac{n_m}{c} C_{pr} I \hat{z} \tag{3.3}$$

$$\boldsymbol{F}_{optical} = \frac{1}{2} \mathrm{Re} \left(\boldsymbol{p} \nabla \boldsymbol{E} \right) \tag{3.4}$$

where n_m, I, and $\hat{z}$ are the refractive index of the surrounding medium, intensity of light and the direction of propagation, respectively. C_{pr} is the cross-section of radiation pressure given by,

$$C_{pr} = \frac{8}{3} \pi (kr)^4 r^2 \left(\frac{\epsilon - \epsilon_m}{\epsilon + 2\epsilon_m} \right)^2 \tag{3.5}$$

and $\boldsymbol{p}$ is the polarization given by,

$$\boldsymbol{p} = 4\pi \epsilon_m \epsilon_0 r^3 \frac{\epsilon - \epsilon_m}{\epsilon + 2\epsilon_m} \boldsymbol{E} \tag{3.6}$$

where r is the radius of the particle and ϵ, ϵ_m are the relative permittivity of the particle and the surrounding medium. ϵ_0 is the vacuum permittivity. c and k are the speed and wave number of light, respectively. Therefore, we can write the force on the particle as:

$$\boldsymbol{F}_{scattering} = \frac{8\pi n_m k^4 r^6}{3c} \left(\frac{\epsilon - \epsilon_m}{\epsilon + 2\epsilon_m} \right)^2 I \tag{3.7}$$

$$\boldsymbol{F}_{optical} = \frac{2\pi n_m r^3}{c} \left(\frac{\epsilon - \epsilon_m}{\epsilon + 2\epsilon_m} \right) \nabla I \tag{3.8}$$

where, $I = \frac{1}{2} c\epsilon_0 n_m |\boldsymbol{E}^2|$ is the intensity of light. Since the optical force is proportional to r^3 and the scattering force is proportional to r^6, when r is in the order of nanometers, we have $\boldsymbol{F}_{scattering} \ll \boldsymbol{F}_{optical}$. Thus, we will neglect the scattering effects for the remainder of this chapter.

The head-disk interface in the vicinity of the NFT spans several tens of nanometers along the surface of the head and less than 10 nm in the vertical direction across the head-disk interface. Thin structures can fit well in this gap. We can approximate the flake-like structure as an ellipsoid with a very high aspect ratio. Gans [113–115] developed a modified polarization for an ellipsoidal particle given by:

$$\boldsymbol{p} = 4\pi\epsilon_m\epsilon_0 r_1 r_2 r_3 \left(\frac{\epsilon - \epsilon_m}{3\epsilon_m + 3L_i(\epsilon - \epsilon_m)} \right) \boldsymbol{E} \tag{3.9}$$

where r_i and L_i are the radius and a geometric factor in the ith direction, respectively. L_i ranges from 0 and $\frac{1}{3}$ and is given by,

$$L_i = \frac{r_1 r_2 r_3}{2} \int_0^\infty \frac{dq}{(r_i^2 + q) f(q)} \tag{3.10}$$

$$\text{where, } f(q) = \sqrt{(q + r_1^2)(q + r_2^2)(q + r_3^2)} \tag{3.11}$$

Here, r_i is the radius of the ellipsoid in the respective direction. Using the modified polarization factors, the net optical force is given by,

$$\boldsymbol{F}_{optical} = \frac{2\pi n_m r_1 r_2 r_3}{c} \left(\frac{\epsilon - \epsilon_m}{3\epsilon_m + 3L_i(\epsilon - \epsilon_m)} \right) \nabla I \tag{3.12}$$

We call the term in the parenthesis the enhancement factor (E_f) as it indicates the field enhancement that a particle induces around itself. The denominator in this term indicates the possibility of a singularity when the geometric factor and permittivity satisfy the Fröhlich condition, given by:

$$3\epsilon_m + 3L_i(\epsilon - \epsilon_m) = 0 \tag{3.13}$$

$$\Rightarrow \epsilon = \epsilon_m \left(1 - \frac{1}{L_i} \right) \tag{3.14}$$

As the permittivity of the particle approaches the value given by Eq 3.14, the force experienced by the particle drastically increases. Since L_i is always less than 1, the condition is met only when the real part of the permittivity is negative. In such materials, the imaginary component of the permittivity is non-zero; thus, the force does not reach a singularity. Nevertheless, this condition is interesting because when the real part does satisfy the Fröhlich condition, the optical force reaches its peak value. The relevance of this condition will be explored when we study the material dependence of the optical force.

3.2.2 Thermophoretic Force

We calculated the thermophoretic force in Sec. 4.2; however, the formulation was done for a cylindrical nanoparticle. Since the optical force was quantified for spherical and ellipsoidal nanoparticles, we derive approximate relations to account for this shape change. The thermophoretic force, in the case of spherical particles, was developed by Torczynski and reported in Gallis [116].

$$F_T = - \left(\frac{3}{2}\pi r^2 n k_B \sqrt{(T_C T_H)} \right) \left(\frac{T_H^{1/2} - T_C^{1/2}}{T_H^{1/2} + T_C^{1/2}} \right) \tag{3.15}$$

Where r, n, k_B are the sphere's radius, the number density of the gas, and the Boltzmann constant. T_H and T_C are the temperatures in the hot and cold end, respectively. This formulation accounts for the free molecular nature of the gas bearing when spacing is less than 10 nm. Further, since this equation was developed for a sphere and not an ellipsoid, we will limit the use of the formula to the spherical nanoparticle.

3.2.3 Drag Force

Similarly, we apply appropriate changes to the drag force obtained in Sec. 4.2 to account for the shape difference. The drag forces can be thought of as either the pressure drag or the skin friction drag. In the case of the pressure drag, Epstein formulated the drag force in the free molecular regime as [117]:

$$F = \frac{2}{3}r^2\rho_g\sqrt{\frac{2\pi k_B T}{m_g}}\left(1 + \frac{\pi\alpha}{8}\right) \tag{3.16}$$

where α is a factor depending on the collision of the gas particle with the nanoparticle's surface. In the case of very small spheres, α is close to 1. In the case of an ellipsoidal structure with a high aspect ratio, skin-friction drag force dominates. The skin-friction component can be approximated by the shear force experienced by the head. The total shear force on the head is calculated using an air-bearing simulation. If the total shear force is $F_{s,total}$, then

$$F_{s,ellipsoid} = 2F_{s,total}\frac{A_{ellipsoid}}{A_{head}} \tag{3.17}$$

where $A_{ellipsoid}$ and A_{head} are the projected surface areas of the ellipsoid and the head, respectively.

3.3 Results

3.3.1 Simulation Assumptions

The first set of simulations starts with a clean air-filled head-disk interface with a spacing of 8nm. The clean air was used to understand the origin of smear accumulation. As the air-bearing is pressurized to maintain spacing between the head and the disk, the air density is calculated at a pressure of 25 atm. The representative mass of each air molecule is 4.3×10^{-26}kg. We simulate two particles to compare the forces. One is a spherical nanoparticle with a radius of 1 nm, and the other is an ellipsoid with radii 6nm in the in-plane direction and 1 nm in the vertical direction (see Fig. 3.2). The particles have a refractive index of 1.53 at 830 nm light and a density of 2650 kg/m^3, corresponding to a SiO$_2$ particle. The forces are calculated in three directions. First, the down-track direction that is along the length of the head and parallel to the write-track. Second, the cross-track direction that is

perpendicular to the write-track and along the width of the head. The third is the vertical direction that is perpendicular to the recording medium and the head air-bearing surface. The down-track and vertical directions are shown in Fig 3.1a. The forces were calculated at each point in the plane, and the resulting forces were plotted as a heat map. Each point in this heat map shows the magnitude of the force in the direction that the map represents.

The electric field at the interface of the HAMR head-disk assembly is found by solving Maxwell's equations using a frequency domain finite element method simulation of an proprietary HAMR head-disk assembly in CST Microwave Studio [65]. A steady-state solver is then used to calculate the temperature field.

(a) Side view of Elipsoid   (b) Isometric view of Ellipsoid
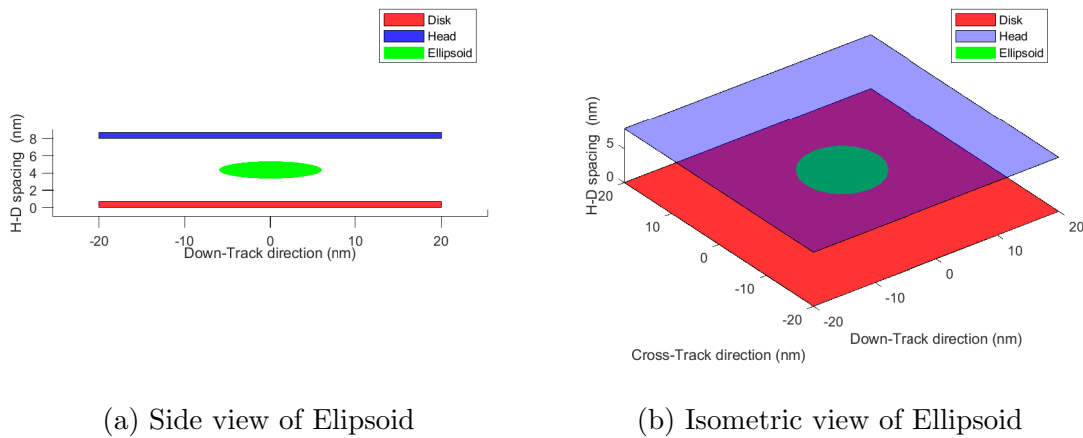
Figure 3.2: Illustration of the ellipsoid: The blue and red planes represent the top and bottom surfaces of the disk and head, respectively. The green disk at the center is the ellipsoidal smear nanoparticle. (a) The side view of the Ellipsoid, (b) The isometric view

3.3.2 Spherical Particle

In the case of the spherical particle, the drag, thermophoretic, and optical forces are shown in Figs. 3.3 and 3.4. The magnitude of the optical force is about 25 fN in the down-track direction and 60 fN in the vertical direction. A stagnation point is observed near the trailing end of the near field transducer (NFT). This force would cause the nanoparticle to stay near the NFT. Some of the features of the forces in the down-track direction are asymmetrical as the underlying electric field gradient is asymmetric. With the forces in the vertical direction (Fig 3.4a), we see a positive force pulling the particle towards the NFT (away from the disk). Nevertheless, the forces are smaller compared to the drag and thermophoretic forces. They indicate that the optical forces on the spherical SiO$_2$ particles would not overcome the forces, pushing the particle downstream of the NFT.
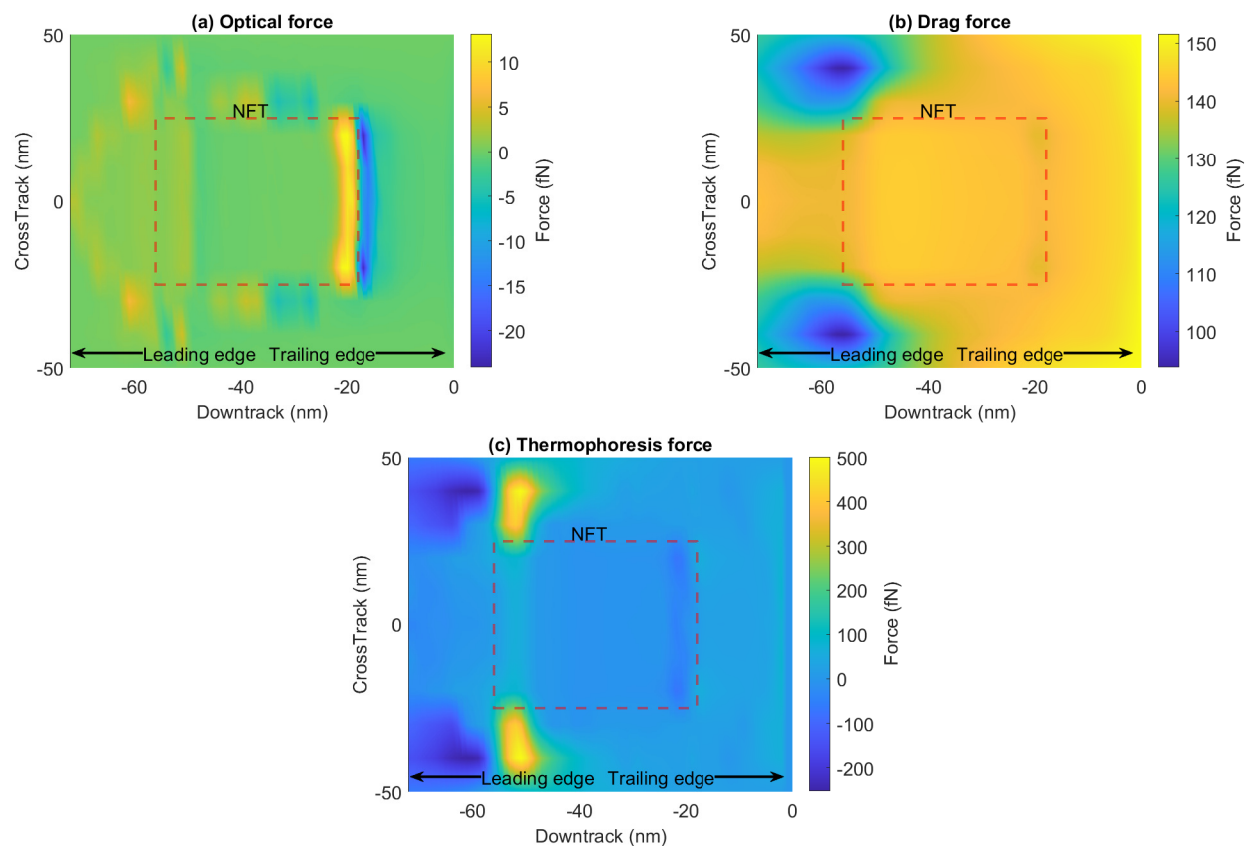
Figure 3.3: Comparison of forces on a spherical particle in the down-track direction. (a) Optical force on a plane 1 nm below the head, (b) the drag force in the down-track direction, (c) the thermophoretic force in the down-track direction

3.3.3   Ellipsoidal Particle

In the case of the ellipsoidal particle, the optical forces and drag force are shown in Fig 3.5. The overall behavior and pattern of the optical forces are similar to that of the spherical case. However, it is worth noting that for an ellipsoidal shape, the force acting on the particle is an order of magnitude larger than the spherical-shaped particle. The optical force on the ellipsoidal particle is 44x larger, whereas its drag force is 2x larger. This is because the optical force is directly proportional to the volume, and the ellipsoidal particle achieves a much larger volume in the thin interface than the sphere. The drag force on the ellipsoidal shape does not increase as dramatically with volume since the ellipsoid behaves as a streamlined body. Thus ellipsoidal or slender-shaped SiO_2 particles would experience significant optical forces. The opposing forces near the trailing edge of the NFT induce a potential well that traps a smear particle against the opposing drag force.

In the vertical direction (Fig 3.5c), the forces are negligible near the disk. However, as
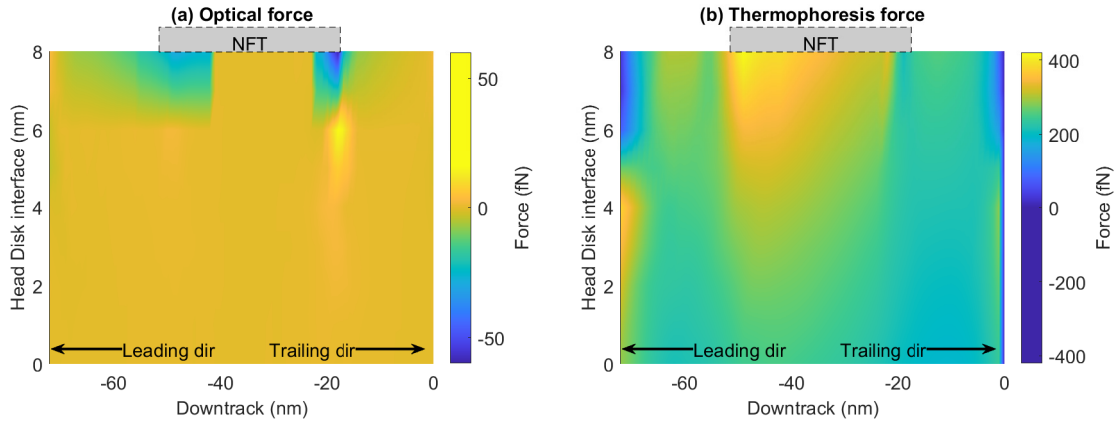
Figure 3.4: Comparison of forces on a spherical particle in the vertical direction. (a) the optical force, (b) the thermophoretic force

the particle approaches the NFT, the optical force gradually increases. Specifically, large forces are seen near the leading and trailing edge of the NFT. This occurs because the surface plasmon generated by the laser has its peak intensity at these locations. The opposing forces create an entrapment zone such that a smear particle flying in the vicinity of the NFT is captured by it. Combined with the forces seen in the down-track direction and cross-track direction, the optical trap is formed that can confine smear particles in the head-disk interface. This confinement can initiate a smear buildup in the head.

3.4   Sensitivity analysis of optical force

3.4.1   Material Dependence

In addition to SiO_2, smear can originate from a complex combination of materials, including HAMR disk metals such as iron, platinum, and cobalt, and dielectrics such as PFPE lubricant [41, 47]. In this sub-section, we vary the smear material to determine the impact on the optical force. The materials' permittivities primarily drive the variation in optical forces. The component containing the relative permittivity is the field enhancement factor E_f. Using the relative permittivity values (square of the refractive index) found in the literature for different particles in Table 3.1, we calculated the optical force along the down-track, cross-track, and vertical directions. The potential well obtained from these graphs is plotted in Fig 3.7. The results indicate that the metals generally experience much larger optical forces than dielectrics. Further, even among the metals which were evaluated, platinum and cobalt have the deepest potential well. Among the dielectrics, silica particles have larger optical forces than PFPE lube. These differences can be attributed to the different enhancement factors associated with the different materials.
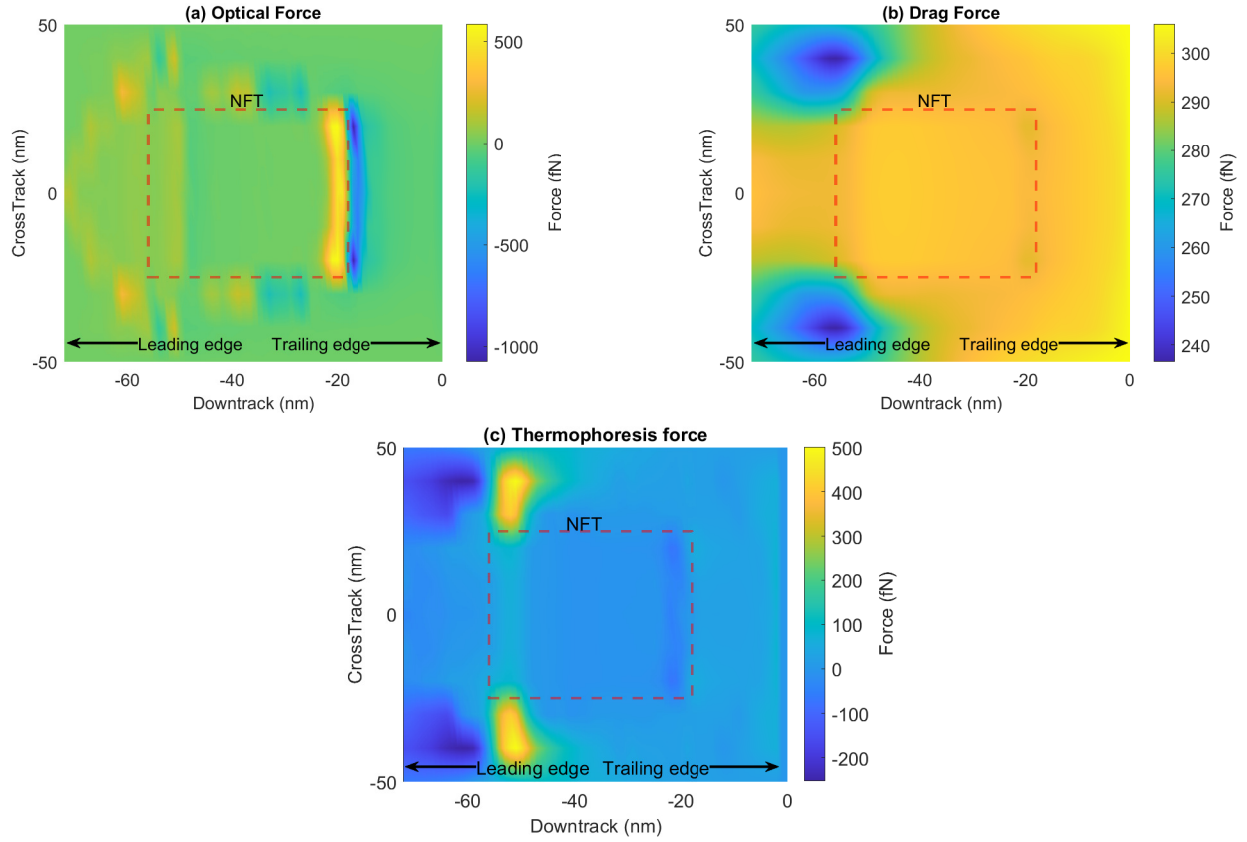
Figure 3.5: Comparison of forces on an ellipsoidal particle: (a) Optical force in the down-track direction, (b) the thermophoretic force in the down-track direction, (c) the optical force in the vertical direction

We plot the enhancement factor for these materials as a function of the aspect ratio in Fig. 3.6. In these plots, the radius in the vertical direction, r_z is set at 1 nm. In the case of iron, when $r_y = 1$nm and $r_x = 6.76$nm, the geometric factor, $L_i = 0.0578$. The permittivities of iron and air are $2.9425 + 3.4115i$ and 1, respectively. When we insert these values in the Frölich equation, we get $E_f = 3.4776$, which is the point where the enhancement factor is at its peak. This peak is because the real part of its permittivity meets the Frölich condition. As mentioned earlier, the imaginary term of the relative permittivity prevents a singularity. Similar behavior is seen for both cobalt and platinum. The peak dimensions are plotted in Table 3.2. For platinum, the enhancement factor rises rapidly to values exceeding iron by an order of magnitude. However, these values are reached only at extremely high aspect ratios. At those dimensions, the particle can no longer be approximated as a point dipole with a uniform electric field gradient across it. The equations developed earlier would, therefore, no longer apply.

In the case of PFPE (Fig 3.6c), the enhancement factor grows until it reaches a steady

peak value. Any increase in the aspect ratio has negligible effects on the enhancement factor. A similar result can be observed for SiO_2 as well. For PFPE and SiO_2, the peak E_f values are 0.27 and 0.44, respectively. These values are less than 1, so we call them attenuation rather than enhancement. This result is consistent with the lower potential wells seen in Fig 3.7.

Material	Refractive Index ($\sqrt{\epsilon}$)
Iron (Fe) [118]	$2.9425 + 3.4115i$
Cobalt (Co) [118]	$2.5452 + 4.9155i$
Platinum (Pt) [119]	$0.601383 + 8.4208i$
PFPE Lube	1.35
Silica	1.53

Table 3.1: Refractive indices of different materials at $\lambda = 830$ nm

r_y (nm)	r_x (nm)		
	Iron	Cobalt	Platinum
2	6.76	8.09	16.45
6	10.16	12.31	26.02
10	11.76	14.38	31.32
E_f (Peak)	3.4776	6.49	85.92

Table 3.2: r_x and r_y combinations when the peak enhancement factors occur for different elements. r_z is fixed at 1 nm.

3.4.2 Effect of Head Disk Spacing

The head-disk spacing in HAMR varies depending on a variety of factors. Here, we examine how the optical forces change with varying head-disk spacing. As in the previous sections, an electromagnetic analysis is done for head-disk spacings of 8 nm, 4 nm, and 2 nm. Optical forces on an ellipsoidal SiO_2 particle were then calculated and analyzed. The normalized potential wells from these cases are shown in Fig 3.8. All three plots show that decreasing the spacing results in an increase in the optical force. Thus, in general, operating at higher spacing may potentially reduce optically-induced smear collection. Further, the increase in the potential depth as we go from 8 nm to 4 nm and that from 4nm to 2nm is similar. This suggests that the rate at which the optical force decrease also decreases at higher spacing. Thus, there is a limit beyond which any increase in spacing will not result in a meaningful drop in the optical force.
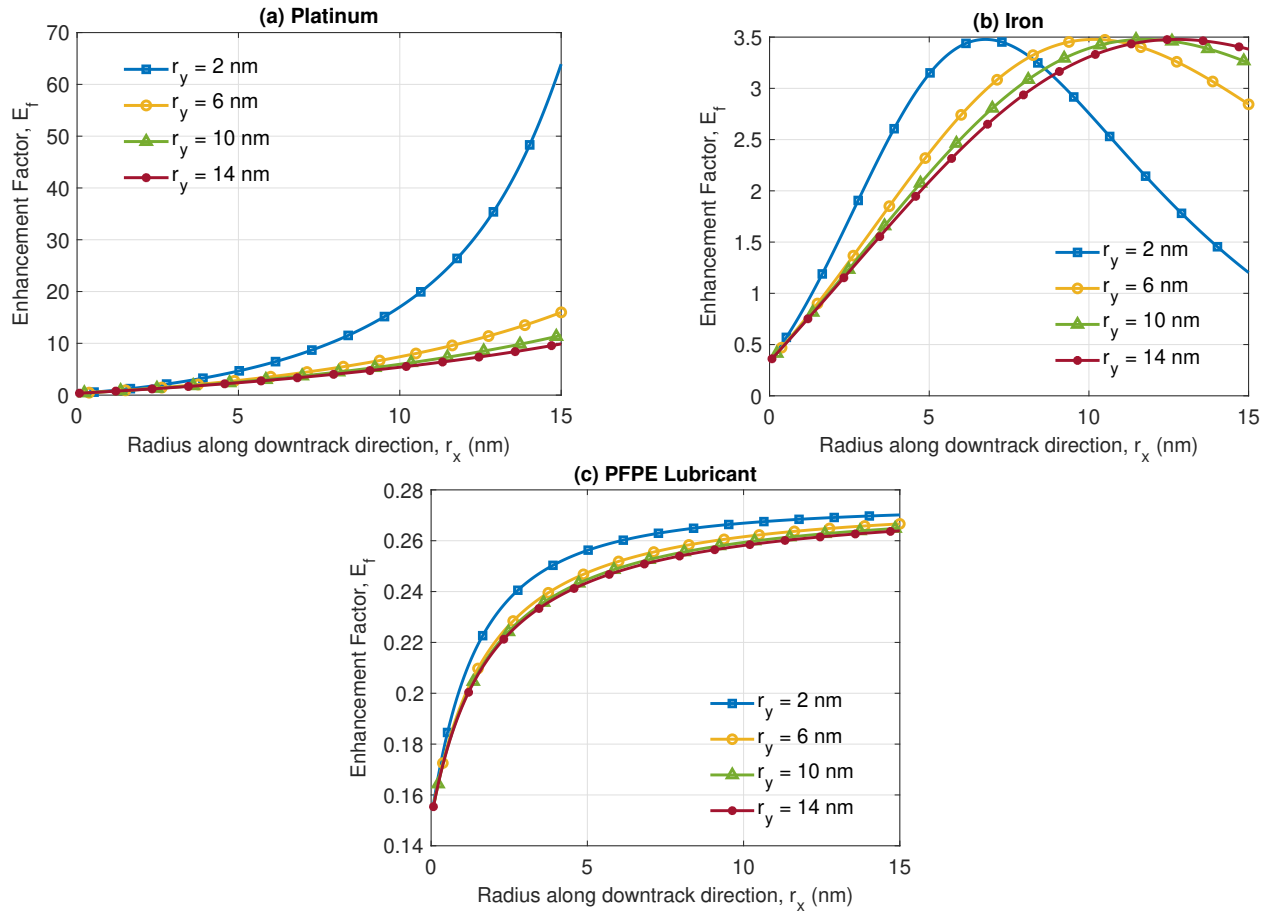
Figure 3.6: Field enhancement for platinum (a), iron (b), and PFPE lubricant(c). r_x is the radius in the down-track direction, r_y is the radius in the cross-track direction and r_z, the radius in the vertical direction is fixed at 1 nm.

3.4.3 Effect of Contamination

Our analysis assumed a clean air interface with no contamination in all previous simulations. However, in operating conditions, the head-disk interface contains many contaminants. In this sub-section, we analyze the force experienced by an ellipsoidal nanoparticle of smear in an environment where other smear contaminants are already present. We consider two kinds of contaminants. Since organic materials, such as the lubricant that coats the disk, are plentiful at the interface, our first contaminant is a layer of organic smear on the head. Second, as we have shown, platinum exhibits a significant enhancement factor and has the potential to have a considerable influence on the forces experienced by a secondary nanoparticle. So we introduced a nano-sized metallic body made of platinum in the interface and analyzed the results.
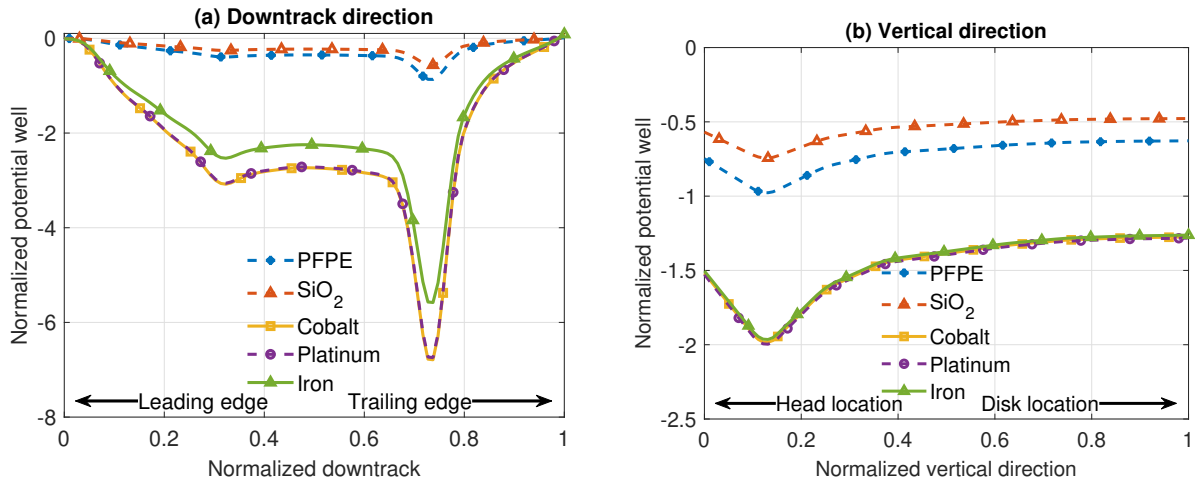
Figure 3.7: (a) The normalized potential well in the down-track direction on a plane 1nm below the head for various materials, (b) the normalized potential well in the vertical direction for various materials

Layer of organic smear

In this case, we model the head-disk interface in two layers. The first layer attached to the disk was clean and free from contaminants, and the second layer attached to the head was made entirely of organic smear. By varying thicknesses of the two layers, this configuration resembles the growth of the smear on the head surface over time. Taking the refractive index of the organic layer to be 1.3, we calculated and analyzed the optical force in the down-track and vertical directions for each case. The forces are normalized using the peak force, and the potential wells obtained are shown in Fig 3.9. The first case is for a total spacing of 4 nm without any smear, the second case when the total spacing is 4 nm with 2 nm each of air and smear, and the third case is for a total spacing of 2 nm without any smear, and the fourth case is for a total spacing of 2 nm with 1nm of air and smear.

The rise in force, for the smear of the 2 nm and 4 nm cases, is by a factor of 1.5. Therefore, if we fix the spacing while allowing the smear to build up on the head, the optical forces experienced by a smear nanoparticle in the layer of air increase. Further, the potential well in the second and third cases follow a similar path at critical locations. In both these cases, a 2 nm layer of air is present. This shows that the thickness of the layer of air determines the optical force on a smear nanoparticle. When the smear accumulates on the head's surface, the effective depth of the clean air reduces. Thus, the interface behaves as if the head-disk spacing is reduced when we estimate the optical force. These results highlight the importance of keeping the head-disk interface free of organic smear layers. Otherwise, the optical force can promote additional smear growth.
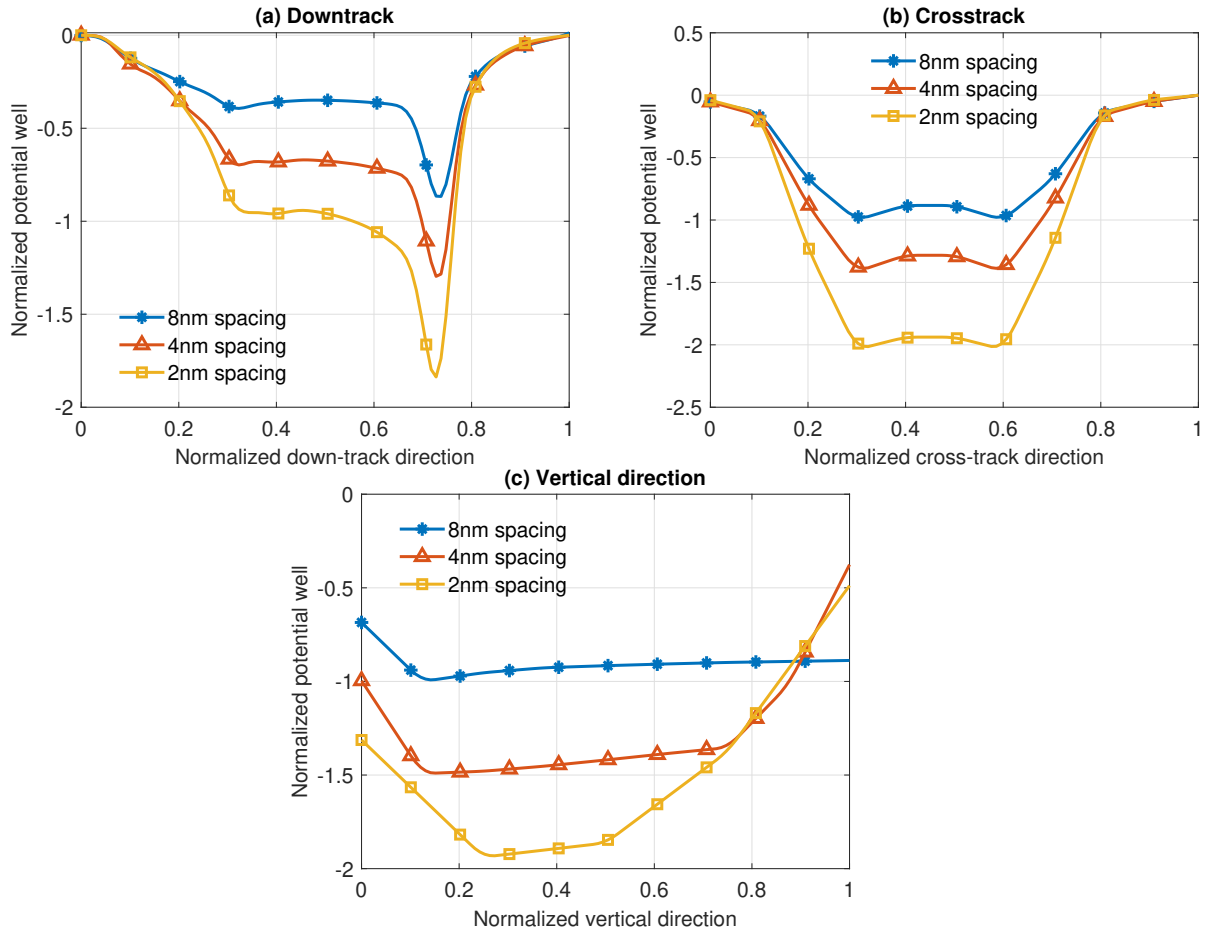
Figure 3.8: Optical forces for varying spacing, (a) down-track direction (calculated on a plane 1 nm below the head), (b) cross-track direction (calculated on a plane 1 nm below the head), and (c) vertical direction

Presence of a metallic body

Here, we introduce a cylindrical object made of platinum into a clean 8 nm thick head-disk interface. The cylinder has a radius of 10 nm and a length of 2.2 nm. The platinum particle was placed on the disk. We then calculate the optical force and examine the net force field generated by the primary interface particle on a secondary nanoparticle. The force field is normalized by the force when the object is not present. The subsequent potential well in the down-track and vertical directions is shown in Fig. 3.10. We see that the potential well's depth in the presence of the particle is about 8 times greater in the down-track direction and 20 times greater in the vertical direction. The peak drop in the potential well is found to be near the surface of the cylinder. The sharp drop is due to a secondary surface plasmon being generated at the metal-air interface of the object. This secondary plasmon induces a
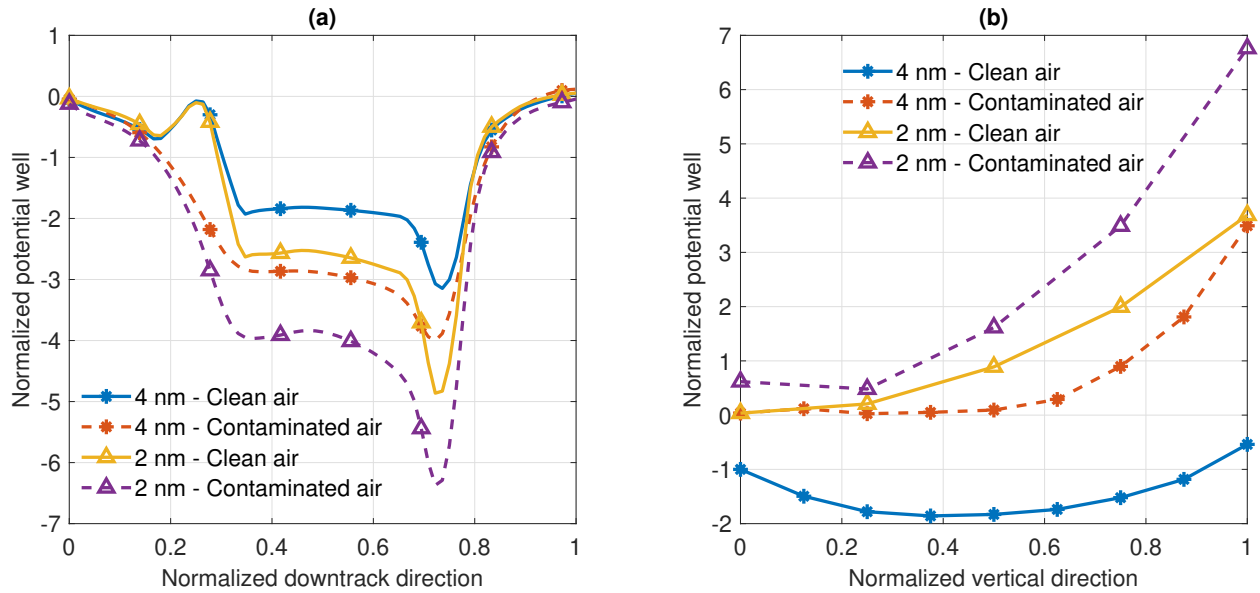
Figure 3.9: Normalized potential well along different directions for varying spacing and contamination rates, (a) down-track direction, and (b) vertical direction

large electric field gradient capable of trapping other smear nanoparticles. Therefore, smear particles in the vicinity of the metallic object are drawn towards it rather than the NFT. This attraction and subsequent adhesion to the metallic object could cause it to grow in size. Effectively, the original particle and those surrounding it behave as a composite object with an arbitrary shape. This composite object now has a much larger volume and, consequently, a much larger optical force acting on it induced by the electric field of the NFT.

3.5 Conclusions

This chapter quantifies the optical force on a smear nanoparticle in the head-disk interface. The investigation of the relevant parameter space revealed conditions under which the optical force can have appreciable effects on smear formation. These factors can be categorized as smear and interface parameters.

The key smear parameters are the smear nanoparticle's shape, material, and volume. Increasing the volume of the particle results in larger forces. In the film-like head-disk spacing, the increase in volume is achieved by considering a disk/ellipsoidal-shaped smear flake. An ellipsoidal shape combined with appropriate permittivity in metals also allows for the Fröhlich condition to be satisfied, which enhances the effect by 3 to 6 times. Thus, metals experience a much higher optical force, even when present in relatively small quantities. Dielectrics such as silica and PFPE Lube do not experience field enhancement but rather see an attenuation. Nevertheless, in large quantities, dielectrics can experience significant optical forces.
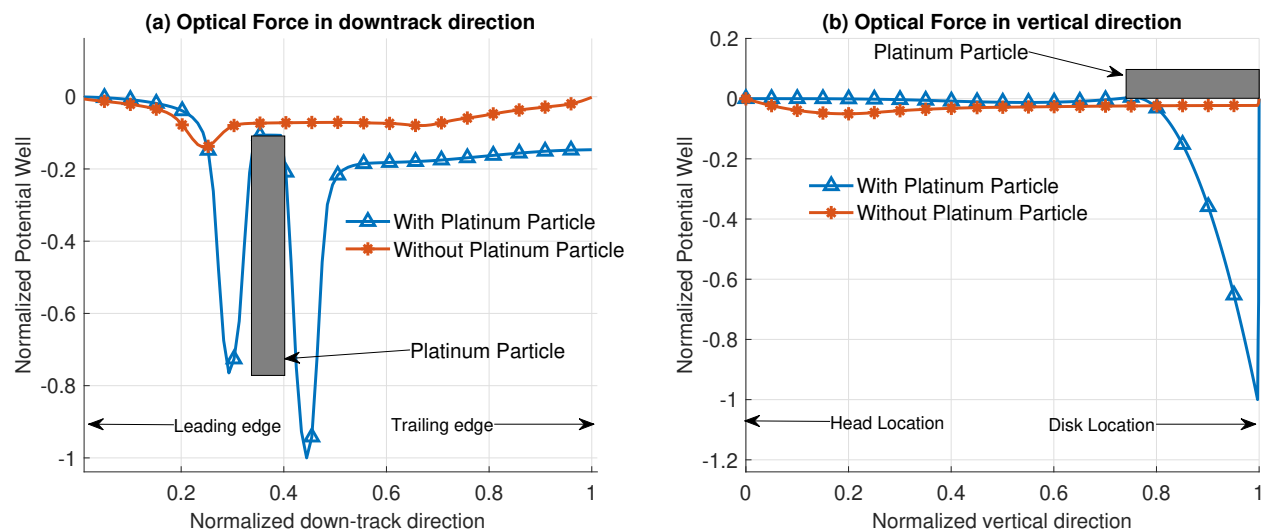
Figure 3.10: Normalized potential well along different directions for the case with and without a platinum particle contamination, (a) down-track direction, and (b) vertical direction

Further, lowering the head-disk spacing increases the optical force on a smear nanoparticle. Additionally, the presence of contaminants like an existing smear layer and a metallic particle can increase the optical force experienced by a secondary smear particle. Metallic contaminants have the greatest influence on optical forces. The force increase is more than an order of magnitude larger than the case without the particle. This is due to the formation of a secondary surface propagating plasmon at the metallic particle-to-air interface.

Since optical forces are dependent on the magnitude of the electric field gradient, a change in the NFT design may result in different optical forces. Nevertheless, when an NFT generates a surface plasmon, optical forces will be present near it. The magnitude of the force depends on the magnitude of the electric field gradient.

This chapter presents work published in *Scientific Reports* in 2023 (reprinted from [39] with a CC BY 4.0 license)

Chapter 4

Air Bearing Forces on PFPE Lubricants

4.1 Introduction

Many studies have shown that one of the major components of the smear on the head surface is the disk (PFPE) lubricant fragments [36, 69, 120]. As the head and the disk surfaces are separated by an air bearing, these lubricant fragments must travel through the bearing before they reach the head surface. The molecules from the air bearing can interact with these molecules, deflecting them in various directions. Therefore, we quantify the forces acting on a PFPE lubricant molecule. We develop the numerical model in Sec. 4.2. We start by considering that the air-bearing is made of helium. So, we describe the velocity distribution of the helium atoms by the Chapman-Enskog distribution. Then, we study the interaction between the helium atom and lubricant molecules by the scattering angle. This interaction quantifies the amount of momentum transferred when they collide. Finally, we combine the scattering angle and the velocity distribution to compute the force on a PFPE lubricant molecule. The equations reveal three forces: drag, thermophoresis, and lift forces. In Sec. 4.3, we calculate the force across the relevant parameter space to study the conditions where each force dominates. Finally, we conclude the chapter in Sec. 4.4.

4.2 Numerical Model

To quantify the air-bearing related forces, we approximate the lubricant shape to a cylinder defined by its length and radius. We also assume that the laser that heats the system has sufficient power to instantaneously bring the temperature of each particle to the local temperature.

4.2.1 The Chapman-Enskog Distribution

Since the forces on a PFPE molecule arise due to collisions with the helium atoms, we begin by determining the velocity distribution of the helium atoms. Kinetic theory predicts that in a stationary container with uniform temperature, the velocity distribution of an ideal gas is given by the Maxwell-Boltzmann distribution. However, there are large velocity and temperature gradients in the head-disk spacing. The Chapman-Enskog (CE) distribution is able to account for these gradients. The first order expansion of the CE distribution is given by [121]:

$$f = f_0 \left(1 - \frac{1}{n} \left(\frac{2k_B T}{m} \right)^{\frac{1}{2}} \boldsymbol{A} \cdot \boldsymbol{\nabla} \left(\ln T \right) - \frac{2}{n} \mathrm{B} : \boldsymbol{\nabla} \boldsymbol{v}_0 \right) \tag{4.1}$$

Here, n, m, T, and $\boldsymbol{v}_o$ are the number density, mass, temperature, and mean molecular velocity of the helium atom, respectively. f_0 and k_B are the Maxwell-Boltzmann distribution and the Boltzmann constant, respectively. $\boldsymbol{A}$, and B are expansion terms. The CE distribution contains three terms. The first term is simply the Maxwell-Boltzmann distribution. The second and third terms are the correction terms to account for the temperature and velocity gradients, respectively. Therefore, these three terms can give rise to three different forces in the head-disk spacing. In the literature, they are called the drag, thermophoresis, and Saffman lift forces. If κ and $\boldsymbol{v}$ are the thermal conductivity and molecular velocity of helium, the full expansion of these terms yields [121]:

$$f_0 = n \left(\frac{m}{2\pi k_B T} \right)^{3/2} \exp \left(-\frac{m(\boldsymbol{v})^2}{2k_B T} \right) \tag{4.2}$$

$$f_1 = f_0 \left(-\frac{2m\kappa}{5nk_B^2 T} \left(\frac{m\boldsymbol{v}^2}{2k_B T} - \frac{5}{2} \right) \boldsymbol{v} \cdot \boldsymbol{\nabla} \left(\ln T \right) \right) \tag{4.3}$$

$$f_2 = f_0 \left(-\frac{4m^2\kappa}{15nk_B^3 T^2} \left(\boldsymbol{v}^T \boldsymbol{v} - \frac{1}{3} \boldsymbol{v}^2 \boldsymbol{I} \right) : \boldsymbol{\nabla} \boldsymbol{v}_0 \right) \tag{4.4}$$

where f_0 corresponds to drag force, f_1 corresponds to thermophoresis, and f_2 corresponds to lift force. Further, the thermal conductivity of the gas can be calculated from its mass and diameter by [121]:

$$\kappa = \frac{75}{64d_g^2} \sqrt{\frac{k_B^3 T}{\pi m}} \tag{4.5}$$

where d_g is the diameter of the gas particle.

4.2.2 Helium and PFPE Interaction

The next step in calculating the force is to define the PFPE-helium interactions. We assume that the helium atoms are chemically inert and undergo no adsorption to the PFPE molecule.

In other words, the collision is purely specular. Then, the PFPE-helium interaction is modeled using a Lennard-Jones potential. For an n-alkane chain and helium, the potential function is given by [122]:

$$U(r) = \epsilon \left[0.676 \left(\frac{r - r_c}{\delta} \right)^{-11} - 1.031 \left(\frac{r - r_c}{\delta} \right)^{-5} \right] \qquad (4.6)$$

Here, r is the distance center-to-center between the alkane chain and the helium atom, and r_c is the radius of the alkane chain. The terms 0.676 and 1.031 are fitted from the general Lennard-Jones potential function summed from the individual atom-atom interactions. Further, $\epsilon = 3.404 \times 10^{-21}$ J and $\delta = 0.354$nm are appropriate Lennard-Jones parameters [122]. Due to the lack of literature about the interaction energy parameters of PFPE particles and considering the mutual cylindrical shape, we assume that the same potential function of n-alkanes applies to PFPE particles for this study.

Then, we calculate the momentum imparted by a helium atom to a PFPE nanoparticle upon collision. By applying the principle of conservation of momentum, we know that momentum gained by a PFPE nanoparticle is the momentum lost by the helium atom. We start by making a simplification. Since the length of the PFPE nanoparticle is much greater than the size of the helium atom, the specular reflection of the helium atom will not result in any momentum change along the axis of the nanoparticle. This is analogous to a particle having a specular (elastic) collision with a smooth wall; the momentum along the plane of the wall remains unchanged. Therefore, we only need to calculate the momentum change along the cross-sectional plane of the nanoparticle as shown in Fig. 4.1a.

(a) A 2D schematic view of a helium atom with the PFPE nanoparticle

(b) A 2D schematic of the trajectory of the helium atom with the scattering angle.
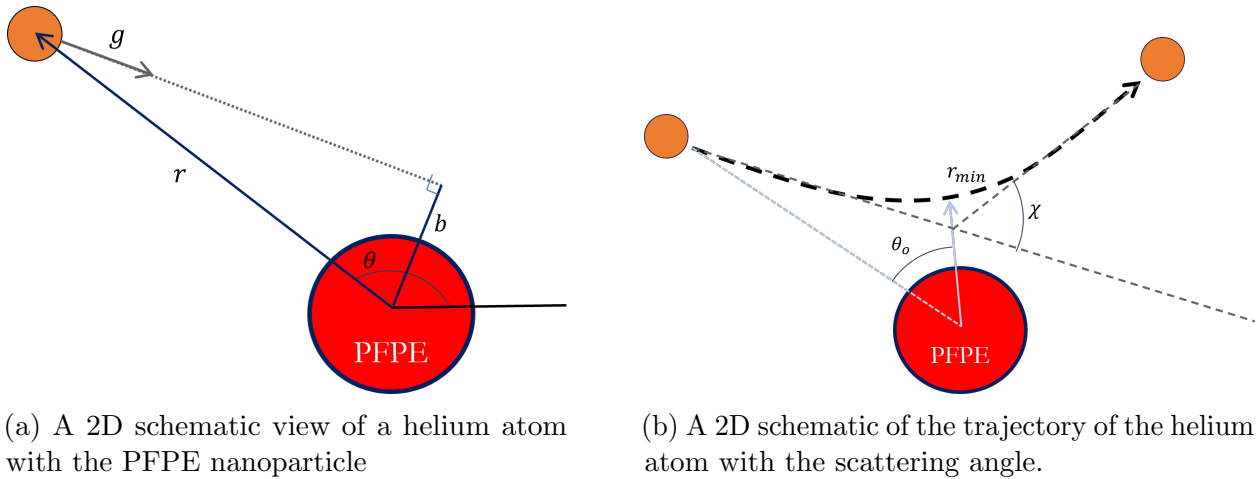
Figure 4.1: Interaction between a helium atom and a PFPE nanoparticle

If g is the in-plane speed of the helium atom, then a specular reflection would conserve its speed. The momentum change is only due to the change in the direction. The angle by which

the helium atom changes its velocity is the scattering angle, χ. To calculate the χ, we use a radial coordinate system with the center of the PFPE nanoparticle as the origin. The helium atom can be described by r and θ, which represent the distance from the original and the angle which it makes with a reference direction as shown in 4.1b. The impact parameter(b) is the perpendicular distance between the center of the PFPE nanoparticle and the undisturbed trajectory of the helium atom. Using the origin as the frame of reference, the conservation of angular momentum and energy are given by [121] (pg 170).

$$r^2 \frac{\partial \theta}{\partial t} = \text{const} \tag{4.7}$$

$$\frac{1}{2} \left(\left(\frac{\partial r}{\partial t} \right)^2 + r^2 \left(\frac{\partial \theta}{\partial t} \right) \right) + \frac{U(r)}{m_r} = \text{const} \tag{4.8}$$

where m_r is the reduced mass of the system to account for the motion of the PFPE nanoparticle. At $r = \infty$, the angular momentum is gb and the energy is $\frac{1}{2}g^2$. Therefore, Eqs 4.7 and 4.8 can be replaced by

$$r^2 \frac{\partial \theta}{\partial t} = gb \tag{4.9}$$

$$\frac{1}{2} \left(\left(\frac{\partial r}{\partial t} \right)^2 + r^2 \left(\frac{\partial \theta}{\partial t} \right) \right) + \frac{U(r)}{m_r} = \frac{1}{2}g^2 \tag{4.10}$$

Time, t, can be eliminated from Eqs 4.9 and 4.10 to derive the differential equation of the helium atom trajectory,

$$\frac{1}{2} \frac{g^2 b^2}{r^4} \left(\left(\frac{dr}{d\theta} \right)^2 + r^2 \right) = \frac{1}{2}g^2 - \frac{U(r)}{m_r} \tag{4.11}$$

Which can then be rearranged to get an analytical value of θ,

$$\frac{dr}{d\theta} = \frac{b^2}{r^4} \left(1 - \frac{U(r)}{m_r g^2} \right) - r^2 \tag{4.12}$$

$$\Rightarrow \Delta \theta = \int_{r_1}^{r_2} \left\{ \frac{b^2}{r^4} \left(1 - \frac{U(r)}{m_r g^2} \right) - r^2 \right\}^{-\frac{1}{2}} dr \tag{4.13}$$

If r_{min} is the radial distance of the helium atom when it is closest to the PFPE nanoparticle, then the trajectory would mirror images along the direction of r_{min}. Thus, the net change in the angle, θ_o, is given by:

$$\theta_o = \int_{r_{min}}^{\infty} \left\{ \frac{b^2}{r^4} \left(1 - \frac{U(r)}{m_r g^2} \right) - r^2 \right\}^{-\frac{1}{2}} dr \tag{4.14}$$

Then, from Fig. 4.1b, we can show that the scattering angle is given by:

$$\chi(g, b) = \pi - 2\theta_o = \pi - 2 \int_{r_{min}}^{\infty} \left[\frac{r^4}{b^2} \left(1 - \frac{2U(r)}{m_r g^2} \right) - r^2 \right]^{-\frac{1}{2}} dr \tag{4.15}$$

Furthermore, at r_{min}, the trajectory is tangential to the radial direction. Therefore, the value of $\frac{dr}{d\theta}$ must be zero there. So,

$$0 = \frac{b^2}{r_{min}^2} \left(1 - \frac{U(r_{min})}{m_r g2} \right) - 1 \tag{4.16}$$

The solution of Eq 4.16 gives the value of r_{min} in Eq. 4.15. If multiple solutions exist, then the largest value must be taken. Solving Eq. 4.15 can be complicated as the values for b, g, and r_{min} span several orders of magnitude. Therefore, the solution was calculated using several numerical tricks to ensure stable results. First, we remove the infinity in the integral through substitution. If $\nu = b/r$, then Eq. 4.15 can be replaced by:

$$= \pi - 2 \int_0^{\nu_0} \left\{ 1 - \nu^2 - \frac{2U(b/\nu)}{m_r g^2} \right\}^{-\frac{1}{2}} d\nu \tag{4.17}$$

where $\nu_0 = b/r_{min}$. Since the helium atoms with a very small value of g possess very low momentum, we can ignore its contribution to the total force. This increases the numerical stability of the integral as it prevents the singularities from occurring in the integration. We chose a value of 0.02 m/s as a reasonable cutoff.

Using the potential function (Eq. 4.6), we calculate the value of ν_0 by solving,

$$f(\nu) = 1 - \nu^2 - \frac{2 \left(A\nu^{11} (b - \nu r_c)^{-11} + B\nu^5 (b - \nu r_c)^{-5} \right)}{m_r g^2} \tag{4.18}$$

where $A = 0.676\epsilon\delta^{11}$ and $B = -1.031\epsilon\delta^5$. The polynomial function contains variables that are several orders of magnitude apart, so a numerical method such as Newton's algorithm needs to be used to find the root. Numerical methods require a good choice of the initial approximation to find the correct root consistently. When we examine the physical conditions behind Eq. 4.18, the terms ν^2, ν^{11}, and ν^5 correspond to the kinetic energy, the short-range repulsive forces, and the long-range attractive force, respectively. Since the short-range repulsive force is the primary cause of the deflection, isolating it yields the best approximation for the root. Therefore, Eq. 4.18 can be reduced to,

$$f(\nu) = 1 - \frac{2A\nu^{11} (b - \nu r_c)^{-11}}{m_r g^2} \tag{4.19}$$

$$\Rightarrow \nu_{0,approx} = b \left\{ \left(\frac{m_r g^2}{2A} + r_c \right) \right\}^{-1} \tag{4.20}$$

A subsequent root search using Newton's algorithm was found to be very reliable. However, two edge cases still need to be checked for. The first was due to numerical precision. Consider Fig. 4.2 that plots the $f(\nu)$ over a range of ν and the location of the calculated root. Although it may seem that the root was correctly found, a closer view reveals that the function value at the root was less than zero. Such a value eventually would cause Eq. 4.17 to have imaginary values due to the square root in the integrand. The cause of the issue is directly related to the magnitude of $f(\nu)$. The large powers cause values near the zero to be in the order of 10^9. Therefore, values in the order of 10^2 are approximated to be 0 by the numerical algorithm. Therefore, in such cases, a second iteration of Newton's algorithm was attempted to find the root at the positive side of the function.
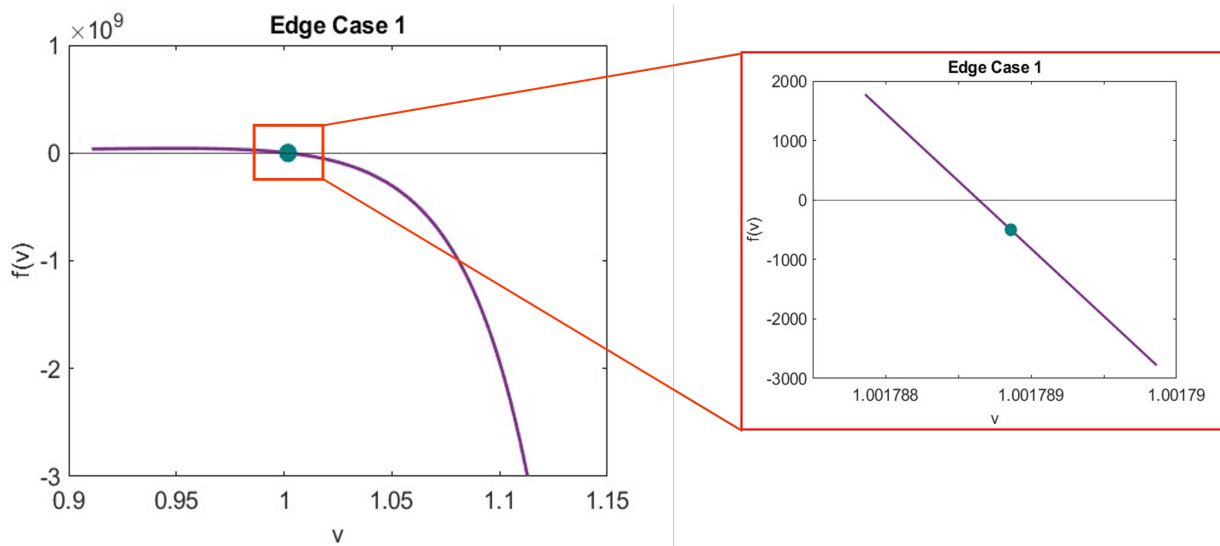
Figure 4.2: An example of the first edge case on account of the numerical precision

The second edge case occurred when the algorithm's precision was too small to detect a zero. Consider the function plot in Fig. 4.3 that shows $f(\nu)$ and a possible root. A close look near the beginning shows the existence of another smaller root. Since ν_0 needs to be the smallest root, it is physically incorrect to use the larger value. Instead of increasing the algorithm's precision, leading to an increased computational cost, we detected this edge case by a constrained minimum algorithm. Using the estimated root and 0 as the bound, the minima of $f(\nu)$ were calculated using a golden section search algorithm and checked if it was below 0. If yes, another attempt at Newton's algorithm was carried out, starting at the location of the minima. This was observed to be faster than directly increasing the precision of Newton's algorithm.

The scattering angle can then be calculated using any numerical scheme, such as the trapezoidal rule. The resulting scattering angle can be plotted as a function of the impact parameters, as shown in Fig. 4.4. We marked three zones that show various types of
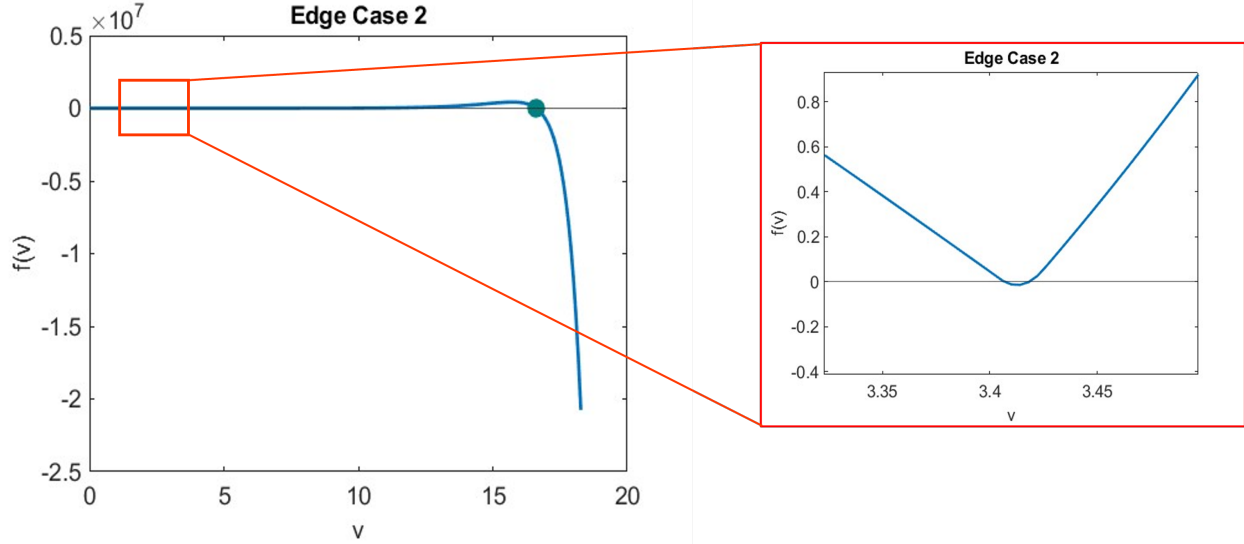
Figure 4.3: An example of the second edge case on account of the algorithm missing a zero

trajectories. Zone 1 refers to a simple bounce off the PFPE nanoparticles as shown in Fig. 4.5a. Zone 2 refers to the oscillatory trajectory between the helium atom and a PFPE nanoparticle. This trajectory is similar to how satellites orbit around a planet. Since the potential function between the two particles contains a long-range attractive element, it is theoretically possible to have such oscillatory force. However, due to the presence of the short-range repulsive element and other stabilities, it does not achieve full orbits as a planetary satellite would. However, it does show an interesting scenario. Finally, zone 3 contains particles that are not affected by the PFPE nanoparticle.

4.2.3 Quantifying Forces

Now that we know the deflection between a helium atom and a PFPE nanoparticle, given an incident velocity and impact parameters, we can quantify the force exerted on a PFPE nanoparticle. We start by defining a collision cross section Q_s as a function of the velocity, g as,

$$Q_{sp}(g) = \int_{-\infty}^{\infty} (1 - \cos \chi) db \tag{4.21}$$

Since $\chi(b) = \chi(-b)$, we can replace Eq. 4.21 with,

$$Q_{sp}(g) = 2 \int_{0}^{\infty} (1 - \cos \chi) db \tag{4.22}$$

In order to calculate the integral, Q_{sp}, we first define two terms based on Fig. 4.4. We first observe that below a critical value of b, the scattering angle is π, which is marked as Zone 1.
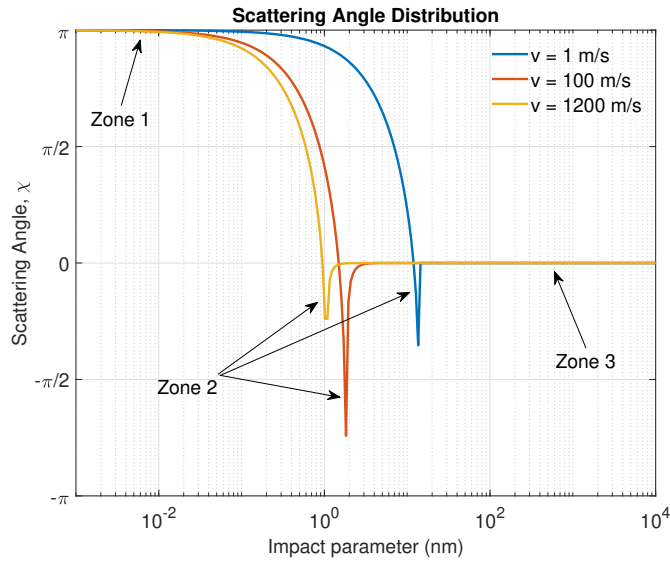
Figure 4.4: Scattering angle for various helium atom velocities
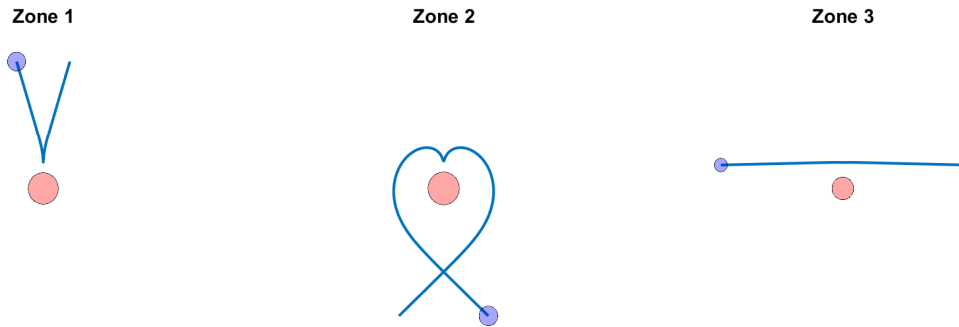
Figure 4.5: Trajectories for the helium atom traveling at 100 m/s at various zones. The particles in zone 3 are doubled in size for visualization

We denote this value as b_{min}. Further, we also observe that above a certain value of b, that is, zone 3, the scattering angle is 0. We denote this value as b_{max}. Then, the scattering Eq. 4.22 can be replaced by,

$$Q_{sp}(g) = 2b_{min}(1 - \cos \pi) + 2b_{max}(1 - \cos 0) + 2 \int_0^\infty (1 - \cos \chi)db \qquad (4.23)$$

$$\Rightarrow Q_{sp}(g) = 4b_{min} + 2 \int_{b_{min}}^{b_{max}} (1 - \cos \chi)db \qquad (4.24)$$

Therefore Eq. 4.24 can now be solved using any integral scheme. We used a trapezoidal rule with an adaptive step size that depends on the magnitude of b. Before proceeding further, we observe that for a given PFPE nanoparticle interacting with a helium atom, Q_{xp} is strictly a function of g. Therefore, instead of recalculating this value in the subsequent integrals, we make a table with discrete values of Q_{sp}. Then, we use an interpolation scheme on the table to calculate the value at a given g. Finally, we can calculate the three forces on a PFPE molecule as [123–125]:

$$\boldsymbol{F}_{i,\perp} = m_r \int_{\boldsymbol{v}} L' f_i g g_\perp Q_{sp} d\boldsymbol{v}, \ i = 0, 1, 2 \tag{4.25}$$

where the subscript $\perp$ refers to the component perpendicular to the axis of the PFPE molecule. The subscript i refers to the drag ($i = 0$), thermophoresis ($i = 1$), and lift ($i = 2$) forces. L' is the maximum distance beyond which the helium atom cannot collide with the PFPE molecule. Reference [123] estimates the L' by,

$$L' = L \sin\left(\zeta\right) \tag{4.26}$$

where, L is the length of the PFPE nanoparticle and ζ is the angle that the velocity of the helium atom (g) makes with the axis of the PFPE nanoparticle. Since we made no assumption on the size and mass of the helium atom, Eq. 4.25 can be used for any spherical atom or molecule using an appropriate $U(r)$. The integral in Eq. 4.25 can be calculated as follows. First, we define a prefactor, $P_{f,i}$:

$$P_{f,0} = m_r N \left(\frac{m_r}{2\pi k_B T}\right)^{(3/2)} \tag{4.27}$$

$$P_{f,1} = -\frac{2}{5} \frac{m_r^2 \kappa}{k_B^2 T^2} \left(\frac{m_r}{2\pi k_B T}\right)^{(3/2)} \tag{4.28}$$

$$P_{f,2} = -\frac{4}{15} \frac{m_r^3 \kappa}{k_B^3 T^2} \left(\frac{m_r}{2\pi k_B T}\right)^{(3/2)} \tag{4.29}$$

These prefactors come from the Chapman-Enskog distribution (Eq. 4.1). They can be taken outside the integral as they do not vary over the velocity space. Then, we expand Eq. 4.25 as,

$$\boldsymbol{F}_i = P_{f,i} \int_{-g_{max}}^{g_{max}} \int_{-g_{max}}^{g_{max}} \int_{-g_{max}}^{g_{max}} \Omega_j(\boldsymbol{g}) dg_1 dg_2 dg_3 \tag{4.30}$$

The subscript i refers to the type of force - drag, thermophoresis, and lift. And the subscript j refers to its direction. For a given type of force, the Ω_j is a vector with three terms corresponding to the three axes. Further,

$$\Omega_1(\boldsymbol{g}) = g_1 |\boldsymbol{g}| e^{-|\boldsymbol{g}|^2/D^2} Q_{sp}(g_1, g_2) \left(1 - 2\boldsymbol{V} \cdot \boldsymbol{g}/D^2\right) T_i \sin \zeta \tag{4.31}$$

$$\Omega_2(\boldsymbol{g}) = 0 \tag{4.32}$$

$$\Omega_3(\boldsymbol{g}) = g_3 |\boldsymbol{g}| e^{-|\boldsymbol{g}|^2/D^2} Q_{sp}(g_1, g_2) \left(1 - 2\boldsymbol{V} \cdot \boldsymbol{g}/D^2\right) T_i \sin \zeta \tag{4.33}$$

where, $D = \frac{2\pi k_B T}{m_r}$ and $\boldsymbol{V}$ is the velocity of the PFPE nanoparticle. The term T_i differentiates the different types of force (drag, thermophoresis, and lift) is given by:

$$T_{drag} = T_0 = 1 \tag{4.34}$$

$$T_{thermophoresis} = T_1 = \left(\frac{|\boldsymbol{g}|^2 + 2\boldsymbol{g} \cdot \boldsymbol{V}}{D^2} - \frac{5}{2} \right) (\nabla T \cdot \boldsymbol{g}^*) \tag{4.35}$$

$$T_{lift} = T_2 = (\boldsymbol{g}^*\boldsymbol{g}^* - \boldsymbol{I}\boldsymbol{g}^* \cdot \boldsymbol{g}^*) : \nabla C \tag{4.36}$$

$$\text{where, } \boldsymbol{g}^* = \boldsymbol{g} + \boldsymbol{V} \tag{4.37}$$

where T is the temperature and C is the mean flow velocity of the helium-bearing. The limits g_{max} are chosen such that the integrand, Ω_j, is numerically equal to zero. That occurs when its value is less than the precision of a double-sized variable (1×10^{-15}). Finally, we can calculate the drag, thermophoresis, and lift forces on a PFPE nanoparticle.

4.3 The Forces in the Head-Disk Interface

Next, we calculate and compare the magnitude of the three forces using the baseline values from Table 4.1. The results, tabulated in Table 4.2, show that the drag and thermophoretic force can be comparable, whereas the lift force is virtually zero. Therefore, we ignore the lift force for the remainder of this study.

Parameter	Value
Mass of helium molecule (m)	6.6395×10^{-27} kg
Diameter of helium molecule (σ)	260 pm
Temperature, T	700 K
Air-bearing velocity (v_0)	15 m/s
Velocity gradient (∇v_0)	$\begin{bmatrix} 0 & 2 & 0 \\ 0 & 0 & 0 \\ 0 & 0 & 0 \end{bmatrix} \times 10^9/s$
Temperature gradient, ∇T	5×10^9 K/m
Length of PFPE molecule	5 nm
Radius of PFPE molecule	0.5 nm
PFPE monomer mass	91 amu
PFPE monomer length	350 pm

Table 4.1: Baseline values for sensitivity analysis

Then we conduct a sensitivity analysis of the relevant parameter space. Using the baseline values from Table 4.1, we individually vary each parameter for the thermophoresis and drag forces. The results are compared and analyzed to understand the conditions for which each force dominates in the head-disk interface. We start with the dimensions of the PFPE

Type of Force	Absolute Force	Relative Contribution
Drag force	1.76 pN	1
Thermophoretic force	2.56 pN	1.46
Lift Force	1×10^{-10} pN	0

Table 4.2: Relative contribution of the three different forces

molecule - the radius and length. The comparisons are plotted in Fig 4.6. In both cases, there is a linear relationship between the force and the parameter for both thermophoresis and drag force. However, the thermophoresis force increases at a greater rate than the drag force. This indicates that for larger molecules, the thermophoresis force is more likely to be the dominating force.
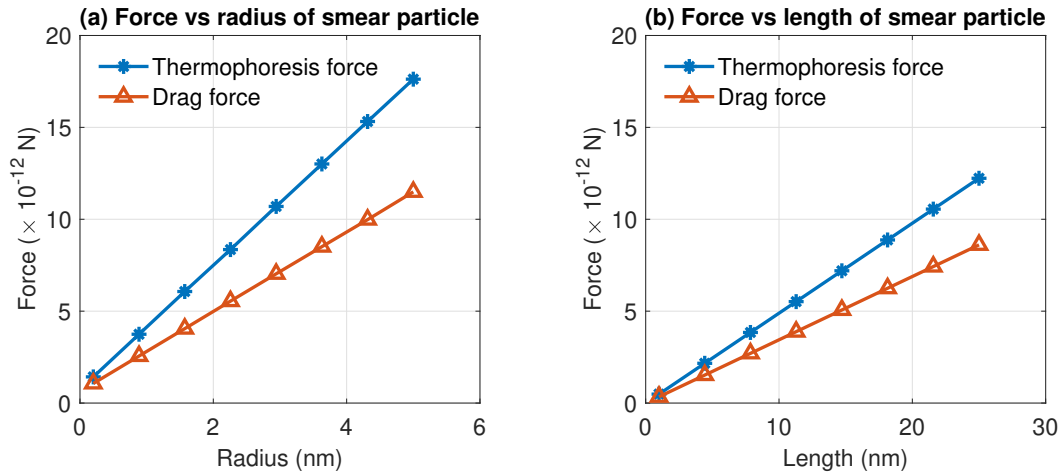
Figure 4.6: Comparison of thermophoresis and drag force for various PFPE molecule parameters, (a) variation with PFPE molecule radius keeping a constant length of 5 nm, (b) variation with PFPE molecule length keeping a constant radius of 0.5 nm.

In order to study how the air-bearing composition affects these forces, we vary the properties of the gas. We considered the mass and the diameter of the gas molecule as the key parameters to investigate. The results are plotted in Fig. 4.7. For increasing mass of the gas particle, the thermophoresis force remains approximately the same, whereas the drag force increases non-linearly. For the baseline case in Table 4.1, the drag force in heavier atoms is greater than in lighter atoms. Since the drag force aids in clearing the smear from the head, a gas medium with larger atoms/molecules appears to be more suitable for reducing smear. As a function of the molecular diameter, the drag force essentially remains the same, whereas the thermophoresis force decreases. Therefore, both graphs show that the drag force

tends to dominate for larger and heavier gas molecules, such as air. Whereas for smaller and lighter particles, such as helium, the thermophoresis force tends to dominate.
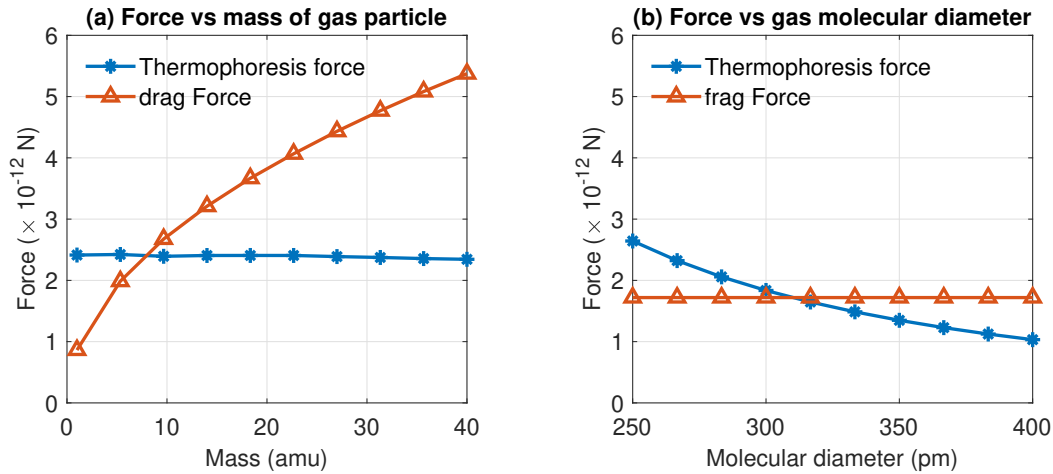
Figure 4.7: Comparison of thermophoresis and drag force for various gas particle parameters. (a) Variation with the mass of the gas-particle keeping a constant diameter of 260 pm, (b) Variation with the diameter of the gas-particle keeping a constant mass of 6.6395×10^{-27} kg.

Next, we consider the force dependence on the parameters in the head-disk interface. Four parameters are considered—the pressure, temperature, velocity of the disk, and temperature gradient. The results are plotted in Fig. 4.8. For the case of varying pressure (Fig 4.8a), the thermophoresis force remains constant, whereas the drag force increases linearly. This indicates that in areas of low pressure, the thermophoretic force dominates. For the case of varying temperature (Fig 4.8b), the thermophoresis force remains constant, whereas the drag force weakly increases with temperature. In the case of varying the temperature gradient (Fig 4.8c), the drag force is constant, whereas the thermophoretic force increases linearly, which is expected since the temperature gradient drives thermophoresis. In the case of varying disk velocity (Fig 4.8d), the drag force linearly increases, and the thermophoretic force remains constant. This is also expected since the moving disk generates drag force on a PFPE molecule.

4.4   Conclusions

This chapter quantified the air-related forces on PFPE nanoparticles in Sec 4.2. Instead of calculating the instantaneous force, we calculated the time-averaged force. The Chapman-Enskog distribution of velocities was used to calculate the momentum of the particle striking the nanoparticle. Several numerical techniques were used to integrate the momentum transfer accurately. We observed three zones of helium-PFPE interactions. First, total reflection
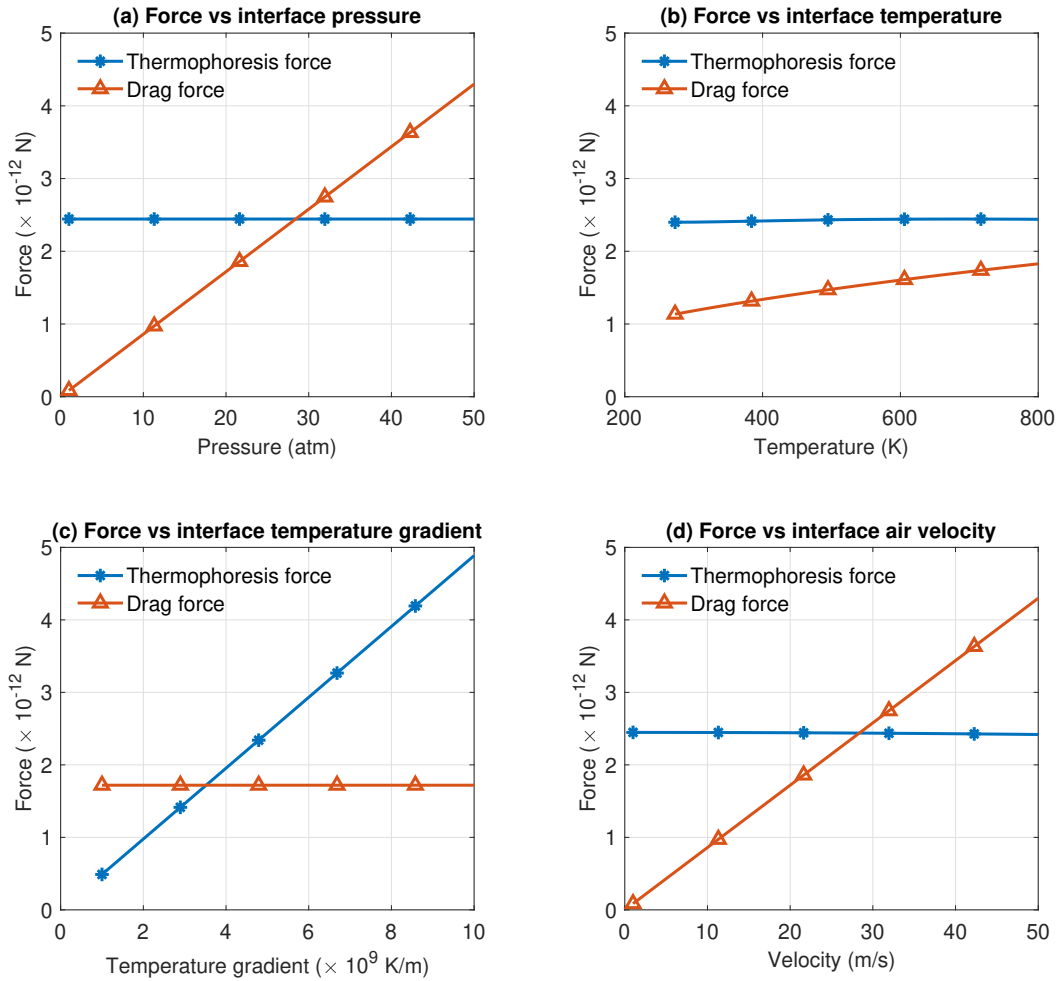
Figure 4.8: Comparison of thermophoresis and drag force for various head-disk interface parameters. (a) Variation with the head-disk interface pressure, (b) variation with the head-disk temperature, (c) Variation with the head-disk temperature gradient, (d) Variation with the velocity of the disk.

occurred at very low impact parameters. Second, oscillatory trajectory occurred at some critical impact parameter. Thirdly, negligible deflection occurred at large impact parameters. The total reflection was further integrated to calculate the total force on a PFPE nanoparticle. Three types of force were considered - drag, thermophoresis, and lift force. Of these, lift forces were supposed to be negligible. A subsequent sensitivity analysis of the forces showed the regions where drag and thermophoresis dominate the other.

First, we looked at the PFPE nanoparticle sizes. For smaller nanoparticles, the ther-

mophoretic and drag forces are close to one another. However, as the sizes grow, the thermophoretic forces rise more rapidly. Then, we looked at the gas particle size. For lighter gases, such as helium, the thermophoresis force dominates, whereas for heavier gases, such as air, the drag force dominates. Finally, we considered the head-disk interface conditions, which revealed that thermophoresis dominates in low-pressure and high-temperature gradient spots, whereas drag force dominates in high-pressure and high gas-bearing velocities.

A part of this chapter was published in *Tribology Letters* in 2024 (reprinted from [126] with a CC BY 4.0 license)

Chapter 5

PFPE Lubricant Kinetics in HAMR Air Bearing

5.1 Introduction

Having characterized the forces acting on a PFPE nanoparticle, we now begin studying the formation of smears. In particular, we focus on streak-like features found in Fig. 1.5. Although many experiments have looked at the evaporation and condensation mechanism behind it, to our knowledge, no simulation has yet studied the formation of these streaks. This chapter explains these features by focusing on the interaction between the air-bearing molecules and the PFPE molecules. Since molecular dynamics simulation is computationally intensive, we employ a novel simulation methodology to simulate the kinetics of these molecules. We track the trajectory of many lubricant molecules under the influence of the force field from chapter 4. Those that adsorb on the head are recorded, and a density map is generated. This map can be visualized to see the growth of head lubricant over time. In Sec. 5.2, we describe the method in detail and explain the theoretical rationale behind the technique. In Sec. 5.3, we conduct simulations under various initial conditions and explain the mechanics of smear formation. Finally, we summarize the method and results in Sec. 5.4.

5.2 Smear Growth Simulation Methodology

We postulate that the air-bearing contribution to smear formation is a three-step process. The first step is the breaking of PFPE-to-surface bonds. In this case, they adhere to the disk by van der Waals (vdW) forces. The rise in the local temperature breaks this bond. The second step is the transport of PFPE molecules towards the head. In this chapter, we will restrict the number of force fields causing the transport to thermophoresis and drag. In addition, other effects such as optical forces (Sec 3 [39]) and ballistic jumps (Sec. 7 [127]) can influence PFPE molecules. However, the conditions where they are significant, such as the presence of metallic nanoparticles or sub 4 nm spacing, are not present in this study. Hence,

we focus only on the forces originating from the interaction between the helium atoms and PFPE molecules. The third step is lubricant condensation/adsorption, where the van der Waal's forces from the head capture these molecules to form smear in patterns, as seen in Fig. 1.5.

5.2.1   Simulation Domain Conditions

The simulation box contains two plates. The top plate is stationary and represents a portion of the head. It has a dimension of 600 nm in the cross-track and down-track directions. The bottom plate moves at the velocity of 20 m/s in the down-track direction as it represents the disk. The dimensions of the bottom plate extend infinitely in both directions. However, the simulation is done only for locations directly below the head. This is possible because the forces are negligible at all other locations. Fig. 5.1 shows a schematic of the resulting air-bearing.
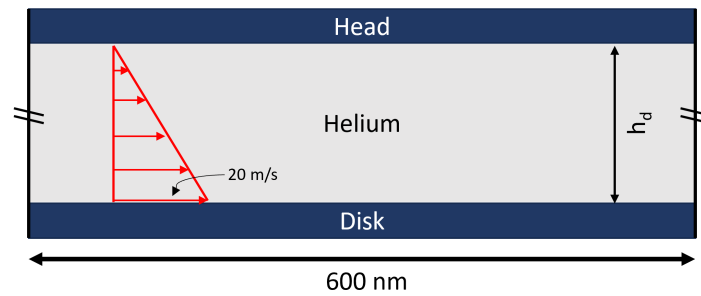
Figure 5.1: A schematic of the simplified air-bearing. It consists of flowing helium molecules at 20 atm pressure. Near the disk, the stream velocity is about 20 m/s, which then linearly tapers away to 0 m/s near the head. A reasonable assumption of the pitch is about 1×10^{-4} rad, which is less than 0.1 nm variation of spacing (h_d) over the length. Hence, we assume the air-bearing to the uniform along the track.

Solving the transient heat conduction equation calculates the temperature profiles at the head and disk surfaces (2.2). The laser heating was represented as a circular heat source with a diameter of 10nm, and the TFC heater was represented using joule heating of an element on the head. The head and the disk surface temperatures are shown in Fig. 5.2. As we observed in chapter 2, the peak temperature at the disk is about 800 K due to the heating from the laser, whereas the head has a peak temperature of 500 K due to the losses from the NFT/WG and the TFC heating. At points near the center, the disk is hotter than the head. However, towards the edges, the head is hotter because the TFC heating occurs over a much larger area [47]. The temperatures at points between the disk and the head are linear interpolations between the corresponding points at the two ends. Thus, there is a

temperature gradient in the vertical direction as well as in the in-plane directions. In the vertical direction, the force can be divided into two zones. First, near the NFT at distances < 200nm from the hotspot, the thermophoretic force is directed from the disk to the head. Second, at locations far from the NFT, the thermophoretic force is directed towards the disk as the head is slightly hotter there than the disk. The former is the smear formation zone, and the latter is the smear removal zone. It is so named because, in the smear formation zone, the molecules tend to move towards the head, forming smear, whereas, in the smear removal zone, the molecules tend to detach from the head and fall back to the disk. Furthermore, in the in-plane direction, the temperature gradient causes the molecules to drift away from the hotspot center.
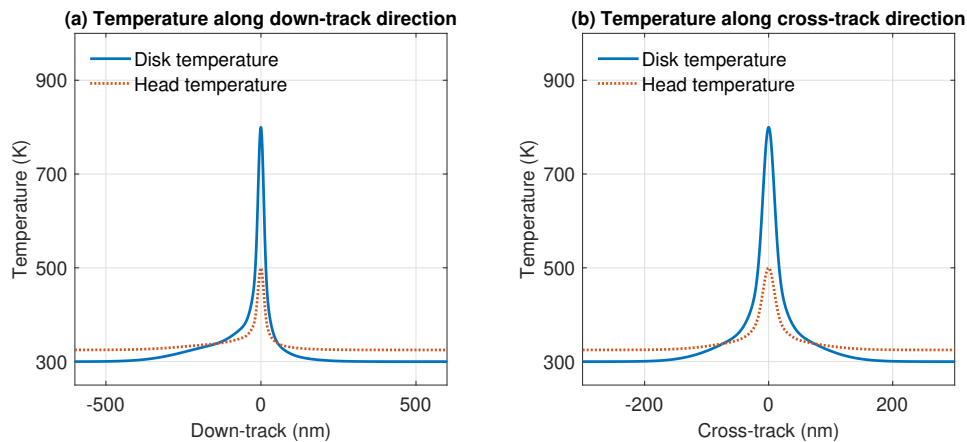
Figure 5.2: Prescribed temperature for the first set of simulations. (a) Along the down-track direction, (b) Along the cross-track direction

5.2.2 PFPE Nanoparticles Properties

The dimensions of the lubricant molecules that form smear can vary depending on the number of monomer units, end-groups, and whether it has undergone thermal decomposition. We use Waltman's estimation for Tetraol-GT, which has a monomer weight of 91 amu and length of 345 pm [128] with a molecular weight of 1200 - 2200 amu [129]. Assuming the monomers lie flat, then the estimated length is between 4.5 nm and 8.3 nm. The physical lower limit for the diameter of a PFPE lubricant chain is $7 - 0.8$ nm [130]. However, the effective monolayer thickness is found to be up to 2 nm [129]. Therefore, the actual radius of a lubricant molecule can be between 0.35 nm and 1 nm. In order to simplify the simulation, we specify the lubricant molecule to have a fixed length of 5 nm and a radius of 0.5 nm. The disk is then coated with a layer of these molecules.

Then, the van der Waals(vdW) interaction energy and the associated force between the lubricant molecule and the head or the disk are given by [131]:

$$E_{vdW} = \frac{A_{ham}}{12}\sqrt{\frac{r}{2d^3}}l \tag{5.1}$$

$$F_{vdw} = \frac{A_{ham}}{8}\sqrt{\frac{r}{2d^5}}l \tag{5.2}$$

Where A_{Ham} is the Hamaker constant, r, l are the radius and length of the smear particle, and d is the distance between the center of the molecule and the surface. The Hamaker constant is approximated to be around 1×10^{-20} J, similar to that of Marchon and Saito (2012) [132]. The particles initially possess kinetic energies defined by the Maxwell-Boltzmann distribution. As the disk moves, the particles move to locations with different temperatures. We adjust their energy by a corresponding amount given by:

$$E_{new} = E_{old} + \frac{3}{2}k_B\Delta T$$

where ΔT is the temperature change. Therefore, we can define the adsorption and desorption criteria for a particle by comparing its kinetic and vdW energies. If the vdW energy exceeds the kinetic energy, then the particle adsorbs, whereas if the kinetic energy exceeds the vdW energy, the particle desorbs.

The simulation starts with a layer of smear particles attached to the disk by vdW forces. The initial particle density of the smear particles on the disk is about 70000 particles/μm^2 or 25000 particles over the 600 nm $\times$ 600 nm disk inside the simulation box. As the simulation progresses in time, new portions of the disk enter the simulation domain, and new particles are created to fill it using the same particle density. If the disk has a velocity of 20 m/s, 840 particles are created every nanosecond. At each time step, the forces on each lubricant molecule are calculated, the adsorption/desorption criteria checked, and Newton's equation of motion determines the new position of each nanoparticle. Their orientation is assumed to be random. Finally, the molecules that adsorb on the head are recorded, and a density map is used to visualize the smear pattern.

5.3 Results and Discussion

Our simulation consists of a clean helium-filled interface at a pressure of 2 MPa. The spacing varies from 4 to 35 nm. The total time of simulation is 3 μs with a 10 ps time-step (The trial runs showed that the choice of the time-step had little effect on the results). We simulate two diameters of laser heaters, 10 nm and 20 nm. To study the mechanics of its formation, we plotted the smear patterns of the head at two timestamps: 100 ns and 3000 ns. The former represents the smear onset phase, and the latter represents the smear growth phase.

The results for the smear onset phase are plotted in Fig 5.3. In Figs 5.3a and 5.3c, we see a bright spot in the center (Features A and D). This occurs because the lower spacing

to hotspot ratio does not allow molecules to move around in the interface. The vertical thermophoretic force dominates and causes most particles to accumulate in the center. On the other hand, for Figs. 5.3b and 5.3d we see multiple interesting features. Instead of having a centralized bright spot, there are two peaks with a slight offset from the center (Features B and G). Furthermore, in Fig 5.3d, there is a streak in the cross-track direction (Feature E). These offsets arise because the spacing allows the in-plane thermophoretic force to separate the molecules from the center. In addition, we can also see two more spots farther away from the center (Features C and F). The trajectories that these particles take are more complicated. They arise from a delicate interplay between the thermophoretic and drag forces in different zones. After the molecule evaporates, it moves toward the head due to the vertical thermophoretic force. At the same time, since the molecule is upstream of the hotspot, the in-plane thermophoretic force pushes the molecule further upstream. As the molecule travels in this direction, it exits the smear formation zone and enters the smear removal zone. This effectively reverses the flow of the molecule, and it starts moving back to the disk. As it approaches the disk, it experiences the drag force and moves downstream. This causes the molecule to re-enter the smear formation zone and change its course toward the head. This time, the distance to the head is smaller, and the vertical thermophoretic force is sufficient to cause the molecule to reach the head. During this process, the molecule constantly faces an unhindered cross-track thermophoretic force. Since this process takes considerably longer, the molecule moves farther from the center, forming these additional spots. In our simulations, these additional dots were only observed for specific conditions. For the 10 nm hotspot, it was found to occur at a spacing between 8 to 10 nm. And for the 20 nm hotspot, it was found to be between 30 and 40 nm.

The results for the smear growth phase are plotted in Fig 5.4. They show the evolution of the streak from the dots seen in Fig 5.3. In the case of a lower spacing to hotspot ratio (Fig 5.4a-c), there is only one thick streak. Other published experiments, such as that by Kiely et al. [47] and Xiong et al. [110] with smaller hotspot sizes and spacing, show similar thick streaks. This qualitative similarity highlights the effectiveness of the simulation strategy in reproducing accurate patterns. Furthermore, in the case of a higher spacing to hotspot ratio (Fig 5.4d), multiple streaks are observed. Near the center, it is filled with smear as in the other three cases. However, farther downstream, the streak diverges into two thick streams. They originate from the nanoparticles evaporating normally (Features B and G in Fig 5.3). The thickness of these streaks for the larger hotspot is greater than those from the smaller hotspot since the area covered by the smear formation zone is greater if the hotspot is larger. Furthermore, Figs 5.4b & 5.4d show additional thinner streaks at the ends originating from the additional dots (Features C and F in Fig 5.3). The length of these thinner streaks was also found to be much greater. The presence of multiple streaks with varying thicknesses is consistent with the results of the experiments from Fig 1.5.

One important aspect to consider in the simulations is that we observe smear within a microsecond. However, in experiments, smear is observed only after a few seconds [40]. This disparity can be explained for two reasons. First, in the experiments, the smear volume measurements are taken after the disk and slider cool down. We know from simulations that
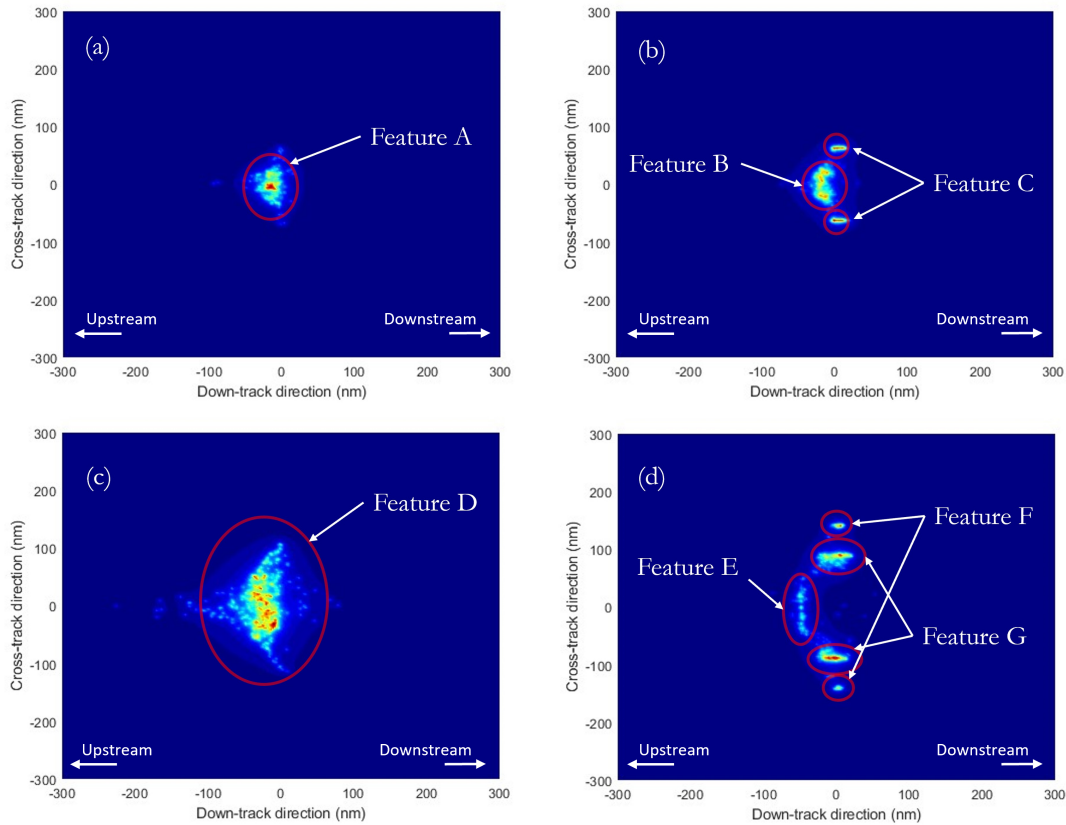
Figure 5.3: Smear onset patterns for various parameters. (a) 10 nm hotspot and 4 nm spacing, (b) 10 nm hotspot and 10 nm spacing, (c) 20nm hotspot and 10 nm spacing, (d) 20 nm hotspot and 30 nm spacing

the NFT temperature cools much slower than the disk [110]. Thus, it is possible that during this brief period, many of the particles loosely stuck to the head fall back to the disk. This means that the smear seen on an actual head is lower than the real-time smear in simulations. Also, in our evaporation criteria, we did not consider the bonding between the polar ends of the PFPE lubricant and the disk. We also did not consider the pressure caused by the helium molecules pressing down on the lube. These factors can reduce the evaporation rate and, subsequently, the smear volume.

5.4 Conclusions

In this chapter, we presented a hybrid smear growth simulation strategy in Sec. 5.2. The novel smear strategy utilizes the framework of molecular dynamics by accurately tracking the
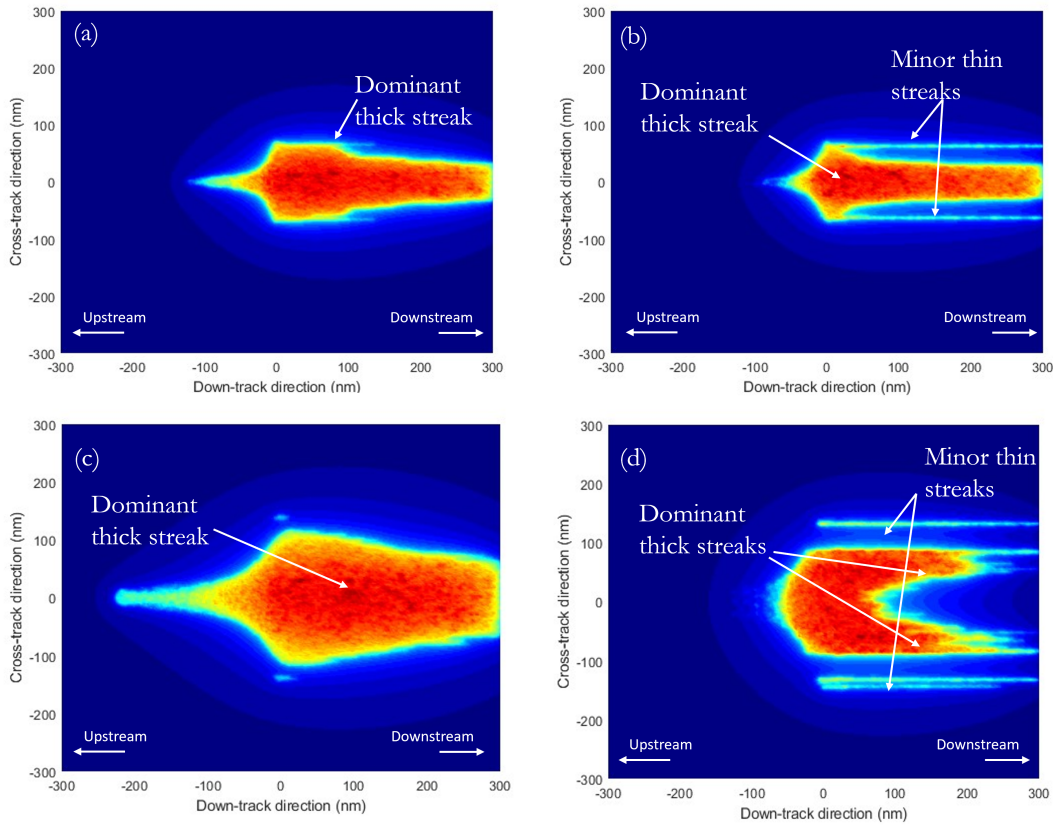
Figure 5.4: Smear growth pattern for various parameters. (a) 10 nm hotspot and 4 nm spacing, (b) 10 nm hotspot and 10 nm spacing, (c) 20nm hotspot and 10 nm spacing, (d) 20 nm hotspot and 30 nm spacing

trajectory of PFPE nanoparticles. However, we used the time-averaged force field instead of calculating the instantaneous force on each nanoparticle in each timestep. This significantly reduced the computational time, allowing the simulation to reach the microsecond regime. We considered that van der Waals forces govern the evaporation and condensation in the head and disk surfaces. The nanoparticles that adsorb on the head were visualized to obtain the smear patterns.

The results from the simulation provided extensive similarity with experiments. This method resulted in patterns that qualitatively matched the experiments. Further, we studied the behavior in two cases: smear onset and smear growth. Smear onset occurs instantaneously at timescales less than 100 ns. For most conditions, it starts near the center, except for large spacing when multiple smear dots are observed away from the center. Further, due to an oscillatory trajectory, additional smaller dots are observed further away from the center. Smear growth occurs after 3000 ns of simulation when the PFPE nanoparticle accumulates near the head. The dots seen at the onset grow into streaks, similar to those found in

experiments. Therefore, the simulation method can be an effective tool to study smear growth in HAMR head-disk interfaces.

A part of this chapter was published in *Tribology Letters* in 2024 (reprinted from [126] with a CC BY 4.0 license) and presented in Intermag-2023 [49]

Chapter 6

Environmental Effects on Nanoscale Gas-Bearings

6.1 Introduction

In chapters 3 to 5, we observed a head-disk spacing between several nanometers and tens of nanometers. In many cases, such an assumption is reasonable given the surface roughness of the disk and the head itself can cause variation of several nanometers [133]. Nevertheless, the minimum clearance between the head surface and disk spacing can be as low as 1 nm. A helium atom is roughly 0.26 nm in diameter, which is roughly a quarter of the minimum head-disk space. The behavior of the gas-bearing in this regime can potentially be different than at larger spacing. Therefore, understanding the effects of the head and disk temperature and ultra-low spacing on the air-bearing is important for the design of a reliable head-disk interface. This chapter aims to quantify the pressure, temperature, and density variations in the air-bearing due to the HAMR laser hotspot.

Additionally, we will also study the effect of humidity, as it has been proven to affect the reliability of hard disk drives. It has been shown to induce a water monolayer on the disk surface [134, 135], decrease the tribocharge in the slider-disk interface [136], influence the lubricant transfer between the head and the disk [137], enhance the heat transfer between the protrusions from the head in contact with the disk when the RH is greater than 75% [138], affect the spreading rate and chemisorption of the lubricants on the disk surface [139], reduce the vaporization energy and thus increase evaporation of lubricants during thermal desorption [140, 141], and promote corrosion of the recording layers [142]. These results show a clear relationship between humidity and the reliability of hard disk drives. Therefore, controlling humidity is vital in HAMR, where the temperatures exceed 500 K. Humidity, commonly known as relative humidity (RH or ϕ), is given by:

$$\phi = \frac{p_{H_2O}}{p*_{H_2O}} \tag{6.1}$$

where p_{H_2O} is the partial pressure of water vapor in the gas and $p*_{H_2O}$ is the saturation vapor pressure of water in the gas. Usually, RH is defined for air; however, the definition applies to any gas mixture. This study will focus on studying the partial pressure of water in high-pressure gas-bearing.

Gas bearings can be designed by solving the molecular gas-film lubrication (MGL) equations [143]. However, Huang et al. [144] showed that the direct simulation Monte Carlo (DSMC) method provides results that agree with the MGL theory. Due to the relative simplicity of setting up a DSMC simulation and the ability to study gas mixtures, we use a modified DSMC to study the gas-bearing. We first describe the DSMC method in Sec. 6.2. Then, we modify the DSMC method to account for dense flows by applying the consistent Boltzmann algorithm (CBA) [145]. Then, we present a simplified 2D channel design as a representative HAMR gas-bearing in Sec. 6.3. Careful iterations fix the dimensions of the channel to maintain proper boundary conditions. Then, in Sec. 6.4, we conduct simulations using a hotspot with down-track and vertical temperature gradients. The results show a vertical temperature and density gradient. Further, a 20% ambient humidity is introduced to calculate the humidity change in the head-disk interface in each simulation. Finally, we discuss the results and present the conclusions in Sec. 6.5.

6.2 Simulation Method

6.2.1 Direct Simulation Monte Carlo (DSMC)

Boltzmann's kinetic theory describes the microscopic evolution of gases. The governing equation is called the Boltzmann transport equation (BTE) given by:

$$\frac{df}{dt} = \left(\frac{\partial f}{\partial t}\right)_{\text{force}} + \left(\frac{\partial f}{\partial t}\right)_{\text{diff}} + \left(\frac{\partial f}{\partial t}\right)_{\text{coll}}, \qquad (6.2)$$

where f represents the probability distribution function. The *force*, *diff*, and *coll* terms refer to the contribution by the external force, diffusion of particles, and the collision between particles. This equation is so powerful that BTE reproduces the famed Navier-Stokes equation at the microscope level [146]. The recent work by Chapman and Cowling [146] establishes the theory and method for handling the BTE, even in the case of non-uniform gases. Unfortunately, solving BTE analytically is nearly impossible for all meaningful problems. However, with the advent of computers, numerical techniques have been developed to yield accurate solutions. Two popular particle-based methods are the molecular dynamics (MD) and direct simulation Monte Carlo (DSMC). These methods essentially follow the trajectory of a large number of molecules across the simulation box. Macroscopic results can then be extracted using statistical averages. Due to the relative simplicity in setting up the simulation and the speed, this study uses the DSMC method.

The DSMC method was popularized by G.A. Bird in the book, *Molecular gas dynamics and the direct simulation of gas flows* [147]. It solves BTE using a probabilistic theory. It is

so named because it uses a Monte Carlo-based theory, describing the position, velocity, and collisions of a particle using a probability function. It is a direct simulation in the sense that it uses a physical model of the fluid rather than traditional mathematical models. This method has been thoroughly tested in high Knudsen-number flows [148], and excellent agreement has been found with experiments [149]. The method starts with a random distribution of the particles in the system. It must be noted that these particles do not represent real particles but are statistical equivalents of real particles. Therefore, each simulated particle may represent more or less than one real particle. The velocity of each particle is defined by the Maxwell-Boltzmann distribution (f) given by:

$$f(\boldsymbol{v}) = \left[\frac{m}{2\pi k_B T} \right]^{3/2} \exp\left(-\frac{m\boldsymbol{v}^2}{2k_B T} \right) \tag{6.3}$$

where m, k_B, T, and v are the particle mass, the Boltzmann constant, the local temperature, and the particle velocity. The state of the system at a given time can now be defined by the position and velocities of all the particles $\{\boldsymbol{p}_i, \boldsymbol{v}_i\}$. In DSMC, at every time-step (dt), the position of the ith particle ($\boldsymbol{p}_i$) is advected along the direction of the velocity by Newtonian mechanics,

$$\boldsymbol{p}_{i+1} = \boldsymbol{p}_i + \boldsymbol{v}_i dt \tag{6.4}$$

The velocity can change either due to collision with other particles or the system boundaries. The collision between other particles can be calculated after the advection process. Since the particles that are separated by a distance much greater than their mean free paths (MFP) are unlikely to collide with each other, the system is divided into cells whose dimensions are approximately the MFP. Ideally, a good cell size is roughly half of the MFP [150]. The cell size also informs the choice of other parameters. The ratio between the real particles and simulated particles should be such that each cell contains roughly 20 to 50 particles [148, 151]. The time step, dt, should be such that no particle moves more than one cell length in each time step. The probability that two particles will collide is proportional to their relative speed [148],

$$P_{coll}(i, j) = \frac{|\boldsymbol{v}_i - \boldsymbol{v}_j|}{\sum_m^{N_c} \sum_{n=1}^{m-1} |\boldsymbol{v}_m - \boldsymbol{v}_n|} \tag{6.5}$$

Clearly, it is computationally intensive to calculate Eq. 6.5 at each time step for every particle pair. Therefore, a stochastic acceptance-rejection scheme is used to calculate the number of collisions. First, two pairs are randomly chosen in a cell. They are accepted or rejected according to the relative speed given by:

$$\frac{|\boldsymbol{v}_i - \boldsymbol{v}_j|}{v_{r,max}} > r \tag{6.6}$$

where r is a randomly chosen value between 0 and 1. $v_{r,max}$ is a value larger than the greatest relative speed. The benefit is that Eq 6.5 and 6.6 yield the same results even if $v_{r,max}$ is overestimated. The number of pairs chosen for collision is given by [148],

$$M_{\text{cand}} = \frac{N_c^2 \pi \sigma^2 v_{r,max} N_e dt}{2 V_c} \tag{6.7}$$

where N_c, σ, N_e, V_c are the number density of the particles in the cell, the diameter of the particle, the number of particles in the cell, and the volume of the cell. Each collision between two simulated particles follows some potential function. The hard sphere model is the most basic. Here, as the name suggests, the particles are assumed to be spheres that undergo elastic collision. The post-collision velocities are given by [151],

$$\boldsymbol{v}_i = \boldsymbol{v}_{cm} + \frac{1}{2} \boldsymbol{v}_r \tag{6.8}$$

$$\boldsymbol{v}_j = \boldsymbol{v}_{cm} - \frac{1}{2} \boldsymbol{v}_r \tag{6.9}$$

where v_{cm} and v_r are the velocities of the center of mass and relative velocity, respectively. The conservation of energy principle only dictates that the magnitude of the relative velocity be conserved. Therefore, the other two unknowns are computed using a probability function [151]. Several other more advanced models have also been proposed, such as the soft sphere model [147], variable soft sphere model [152], and generalized hard sphere model [153] are some of the major ones. Additionally, the collision of the particles and the walls of the system is calculated exactly using the user's choice of boundary condition, such as specular or diffusive.

6.2.2 Consistent Boltzmann Algorithm

The solution from DSMC agrees with the ideal gas law that ignores the finite volume of gas particles. This contradicts the inherent assumption of the diameter of the gas particle in the equation that governs the collisions of particles in DSMC [145]. In many applications, especially in rarefied gas dynamics, the error induced is negligible. However, when the number density increases, the error can build up. For example, let us consider pressure. The relationship between number density and pressure for a gas with a diameter of 4Å is plotted in Fig. 6.1 for the ideal gas law and the theoretical hard sphere model. As the pressure exceeds 10 bars, a deviation can be observed. It arises because the calculation of the number of collisions (Eq. 6.7) and the advection distance (Eq. 6.4) do not account for the finite volume of the gas. Since HAMR operates at peak pressures that exceed 20 bars, there is a need to address this issue.

Alexander and Garcia developed the consistent Boltzmann algorithm (CBA) to address this error [145]. CBA involves two correction terms. First, it increases the number of collisions to account for the enhanced collision rate due to the finite volume of gas. The enhancement
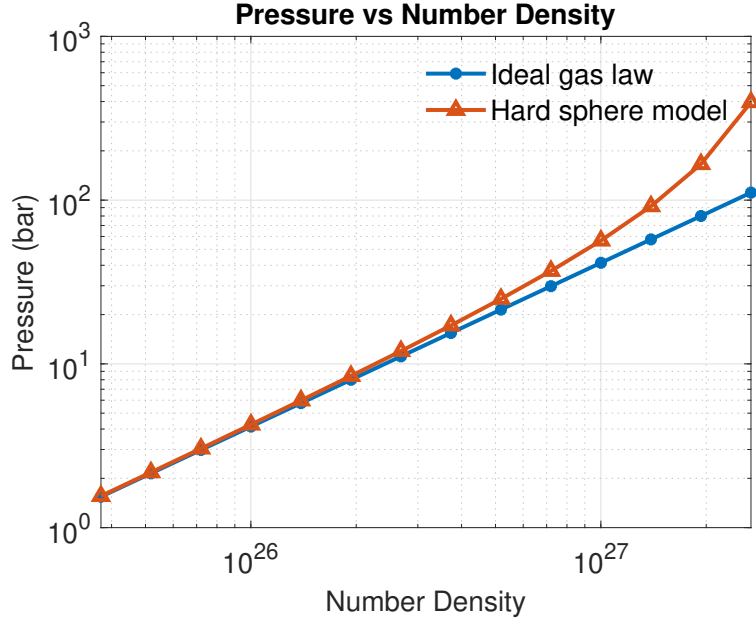
Figure 6.1: The relationship between number density and pressure

factor (Y) is given by [154, 155],

$$Y = \frac{1 + 0.0555678 b_2 n + 0.013944551 b_2^2 n^2 - 0.0013396 b_2^3 n^3}{1 - 0.56943218 b_2 + 0.08289011 b_2^2 n^2} \tag{6.10}$$

where $b_2 = \frac{2}{3}\pi\sigma^3$, σ is the collision diameter and n is the number density. The second correction factor is given by a displacement correction term $\boldsymbol{d}_{cba}$ given by [154],

$$\boldsymbol{d} = \frac{\boldsymbol{v}_r' - \boldsymbol{v}_r}{|\boldsymbol{v}_r' - \boldsymbol{v}_r|}\sigma \tag{6.11}$$

The need for displacement correction can be explained by a schematic in Fig. 6.2. On the left side (Fig. 6.2a), we track the trajectory of two particles (red dots) separated by a distance x and moving towards each other with speed v. As these particles are assumed to be point particles, at $t = x/2v$, the particles collide and change the direction of travel. Then, at $t = x/v$, they return to their initial positions, which are x units away. Then, Fig. 6.2b shows the collision of the same particles but with a diameter, d. Since they possess a finite diameter, the center-to-center distance between the two particles is equal to d. Therefore, the collision happens at $t = \frac{x-d}{2v}$. Then, after the collision, they retrace their path. However, at $t = x/v$, the final positions are separated by a distance d from their initial position. This extra displacement is captured by Eq. 6.11.
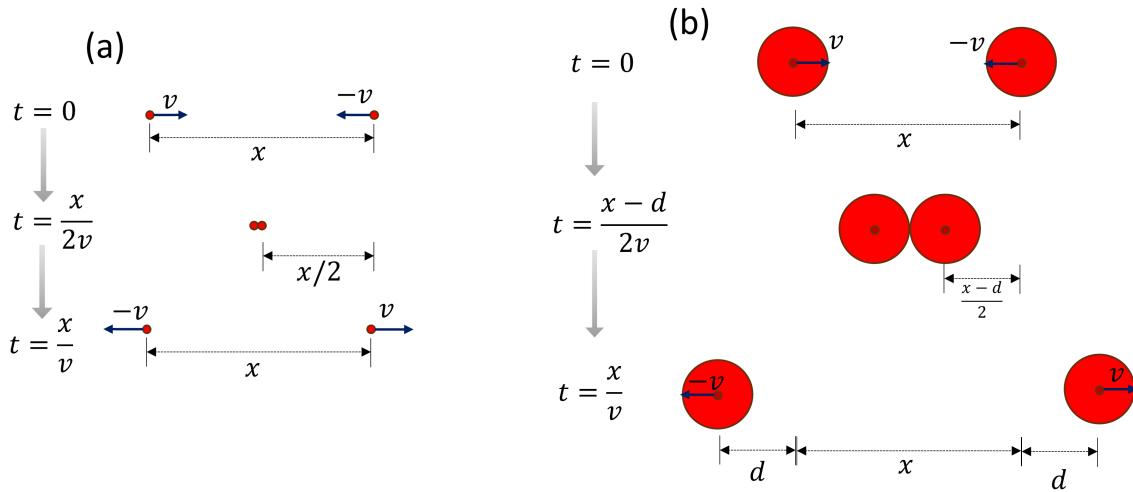
Figure 6.2: A schematic to illustrate the necessity of the displacement correction factor. (a) Gas particles colliding as points. (b) Gas particles colliding as rigid spheres with diameter d

6.2.3   Stochastic Parallel Rarefied-gas Time-accurate Analyzer

Stochastic Parallel Rarefied-gas Time-accurate Analyzer or SPARTA is an open-source software to conduct DSMC simulations [156]. It is written in C++ and supports the MPI message-passing library. Due to the relative simplicity and efficiency in setting up simulations, SPARTA is used to conduct all the DSMC simulations in this chapter. Since SPARTA was designed for rarefied gases, it does not currently support CBA. Therefore, SPARTA needed to be modified to study the non-ideal gas effects.

6.3   Simulation Assumptions

A typical hard drive slider has special etching on the ABS to produce the precise lift force required to counter the suspension load. Several reasons prevent the simulation of these sliders. First, the dimensions that exceed several hundred microns are too large for the simulation to run in a reasonable amount of time. Further, the precision required to model the slider's flying behavior would require very small surface elements. It would lead to large memory consumption and extensive debugging. Finally, the scope of this investigation is to find features applicable to HDI's in general rather than a specific slider design. Therefore, we used a simplified model that captures the necessary characteristics of a HAMR HDI. We focus on two specific factors - pressure and temperature. A 2D channel with varying cross-sections approximates the HDI. As the cross-section reduces along the flow, the flow velocity increases; thus, the dynamic pressure also increases. The domain boundaries can

then be specified with a temperature to imitate the HAMR laser temperatures. The side view of the cross-section is shown in Fig. 6.3. Seven parameters control the shape of the channel. The maximum spacing S_m and the gap (G_p) control the maximum and minimum spacing over the channel lengths. G_p controls the pressure as the maximum spacing is set to 50 nm for all the simulations. The length parameters (L_{1-5}) control the points along the downstream where the spacings change. The boundary conditions at the inflow and the outflow boundaries should satisfy three conditions. First, the pressure at both ends should be 1 atm. Second, the inlet horizontal streaming velocity should be 50 m/s. Third, the pressure gradient should be 0. Since the pressure and streaming conditions are the easiest to implement, they are set at the outset of the simulation. DSMC does not allow the setting of all three boundary conditions simultaneously. Hence, the length parameters are chosen to satisfy the remaining condition.
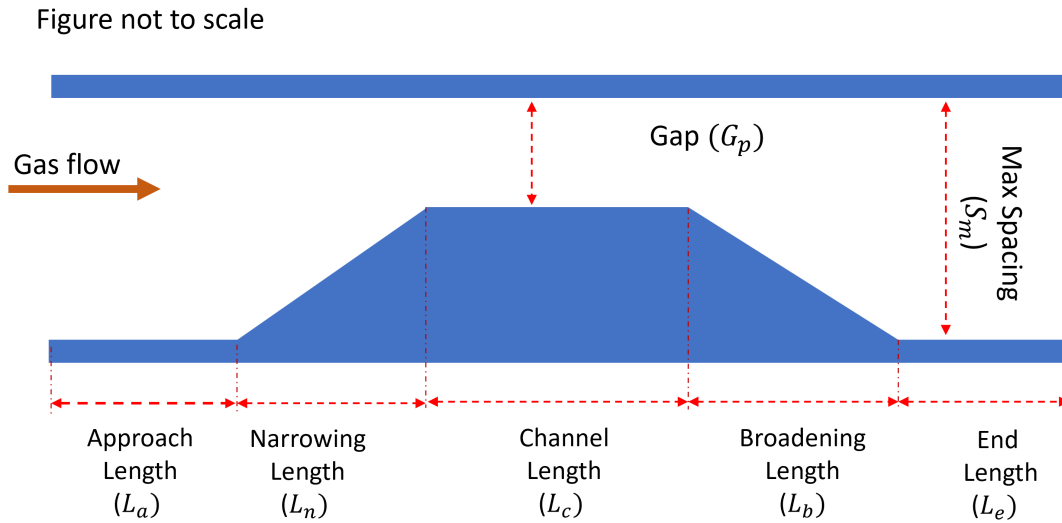
Figure 6.3: Simplified gas-bearing with high-pressure zone

The dimension of a cell must be less than the mean free path (mfp) of a particle so that the probability of collision with a particle outside the cell is minimal. The mean free path of a particle based on kinetic theory is given by:

$$\lambda = \frac{k_B T}{\sqrt{2}\pi d^2 P} \tag{6.12}$$

where d and P are the kinetic diameters and pressure. The temperature can range from 300 K to 600 K. The kinetic diameters of gases range from 2.5 Å to 4.5 Å. And the pressure can range from 1 to 25 bars. Therefore, the MFP can be anywhere between 3.5 nm and 300 nm.

Although a fixed cell size of 3.5 nm can be sufficient to get accurate results, such a choice has several disadvantages. To satisfy the requirement of at least 20 particles per cell, the number of particles would exceed the number of real particles in areas of lower pressure. This leads to additional computational costs that would make the DSMC simulation less efficient than a molecular dynamics (MD) simulation. Therefore, an adaptive grid is employed to account for those variations. The simulation starts with a fixed cell size of 25 nm. As the system reaches equilibrium, the MFP of a particle in each cell is calculated. Then, a conditional statement decides whether to refine or coarsen a grid. Adjacent cells are merged if the ratio between the cell dimension and the MFP is greater than 5. The cells are refined (divided) if the ratio is less than 1. In all other cases, the cells are not changed. This method ensures that cell size remains between 20 to 100 % of the mean free path.

The simulation's timestep (dt) needs to be less than the mean collision time (sometimes referred to as the relaxation time, τ) of a particle. The mean collision time is given by:

$$\tau = \frac{\lambda}{v_{avg}} \tag{6.13}$$

$$v_{avg} = \sqrt{\frac{8k_BT}{\pi m}} \tag{6.14}$$

where m is the mass of a particle. For the pressure and temperature ranges considered earlier, we can calculate the τ for helium to be between 20 ps (picosecond) and 31 ps. In the case of argon, it is between 29 ps and 41 ps. A conservative value of 10 ps is chosen as the timestep for the simulations.

6.3.1 Setting the Length Parameters

The length parameters (L_{1-5}) are set by a trial-and-error method. We start with baseline parameters from Table. 6.1. Starting with L_1, we vary each parameter until we find appropriate values for the length parameters.

Parameters	Value
L_1	50 nm
L_2	100 nm
L_3	200 nm
L_4	100 nm
L_5	50 nm
G_p	10 nm
Test Gas	H_2O

Table 6.1: Baselines values for setting length parameters

Approach length (L_1)

The approach length is the space before the channel starts to change its cross-section. With a L_1 value of 50 nm, successive simulations were conducted, each with increasing values of L_1 until the pressure gradient boundary condition was satisfied. Each simulation was allowed to run for 25,000 timesteps before computing the pressure. The pressure was averaged over 20,000 steps. Although obtaining any quantity with appreciable precision requires it to be averaged over a larger number of timesteps, 20,000 timesteps were sufficient for setting L_1 as we only need to check if the pressure gradient approaches zero. The pressure gradient was calculated using an average value over 10% of the approach length. Fig. 6.4b shows that obtaining zero pressure gradient boundary conditions requires at least 4000 nm of approach length. Therefore, all successive simulations had an approach length of 4000 nm.
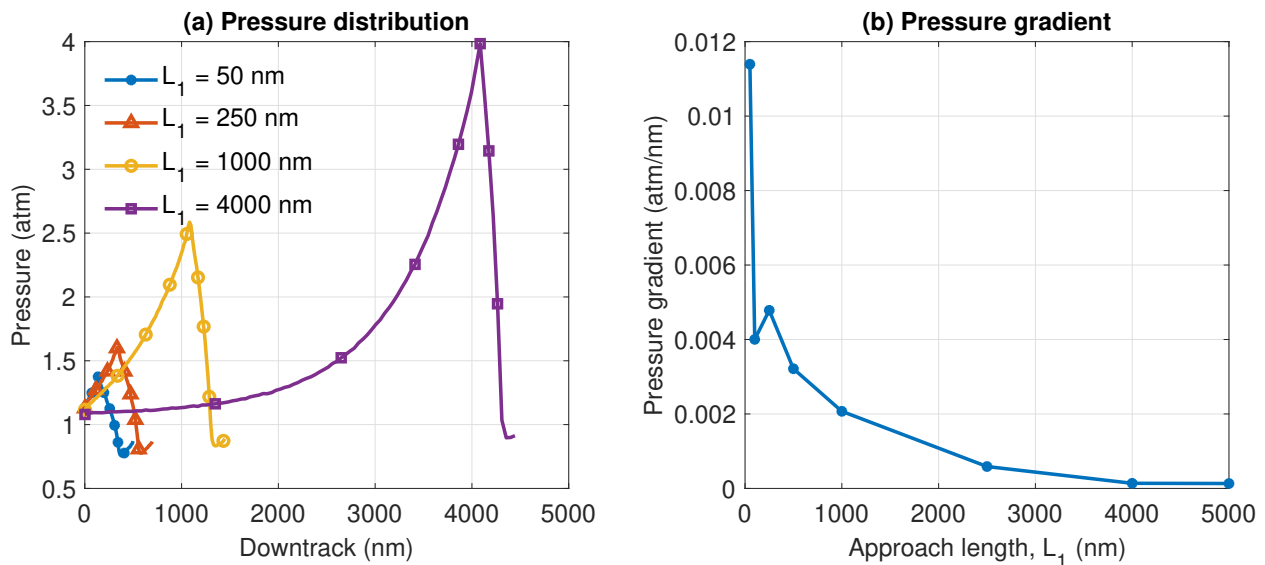
Figure 6.4: Iterations to determine L_1 values. (a) Pressure distributions at various L_1. (b) Pressure gradient at the entrance.

Narrowing length (L_2)

The narrowing length is the region where the cross-section linearly reduces. The length of this area controls the peak pressure, which occurs near the end of this space. The simulation was allowed to run for 50,000 timesteps before computing the pressure, which was then averaged over 25,000 timesteps. The results are plotted in Fig. 6.5. They show that a L_2 of at least 2500 nm is required to achieve the maximum pressure possible. Therefore, a narrowing length of 2500 nm will be used for all subsequent simulations.
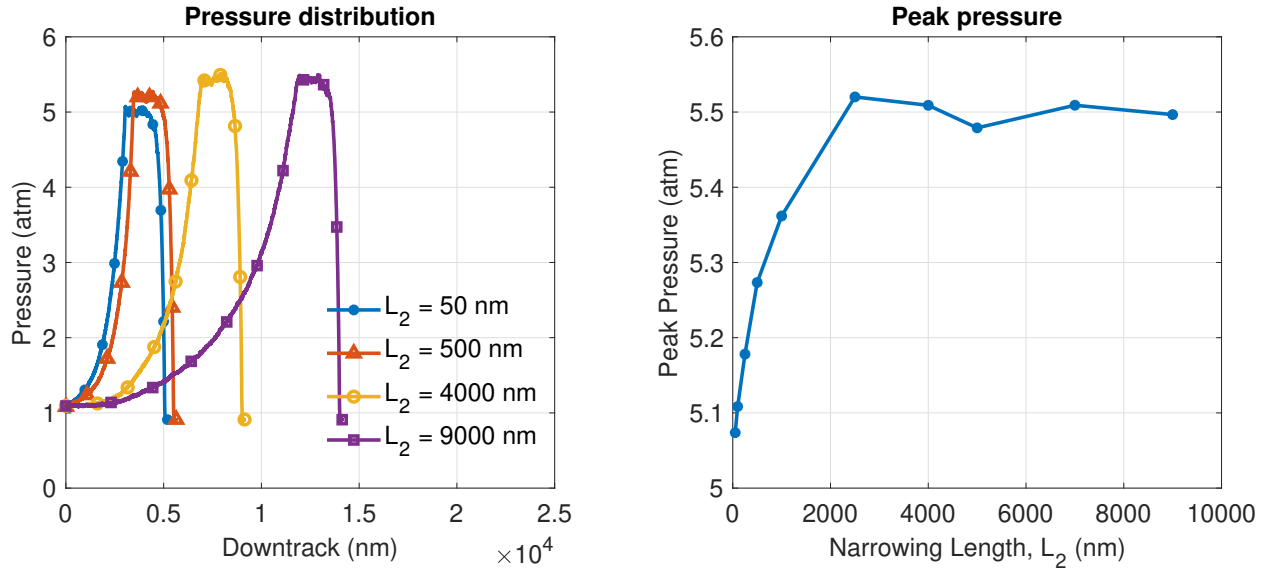
Figure 6.5: Iterations to determine L_2 values. (a) Pressure distributions at various L_2. (b) Peak pressure attained at different L_2 values

Channel length (L_3)

The channel length is the region where the spacing is the minimum. Since the simulation domain is relatively large, the simulation was allowed to run for 100,000 timesteps before the pressure was averaged over 25,000 timesteps. The pressure distribution is plotted in Fig. 6.6. The results show that the peak pressure in the simulation domain is maintained in this region. Therefore, a long channel length can increase the area over which the pressure is averaged, leading to lower statistical errors. Therefore, we will use a channel length of 2500 nm for the remaining simulations.

Broadening length (L_4)

The broadening length is the region over which the spacing gradually increases until the value at the outflow boundary. The simulation was run for 100,000 timesteps before pressure was averaged over 25,000 timesteps. The pressure distributions are plotted in Fig. 6.7. The results show that the L_4 value does not affect the peak pressure; it only modifies how the pressure dies off towards the outflow. Since that does not affect the aim of this study, we will consider a broadening length of 1000 nm. Furthermore, an end length of 500 nm is assumed for the same reasons.
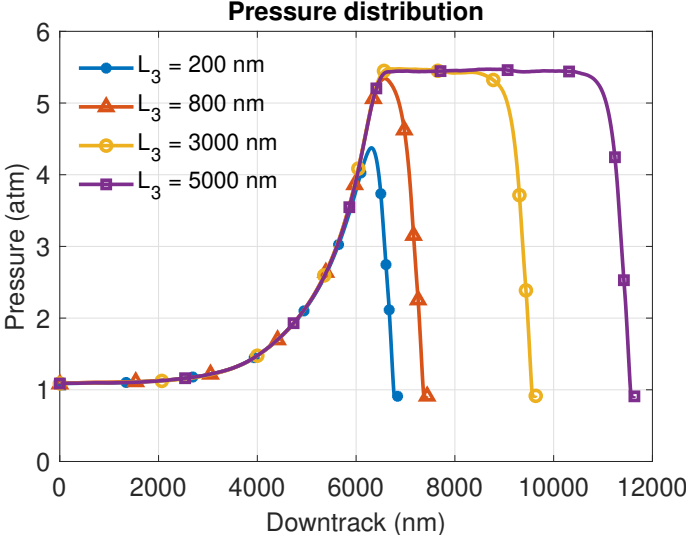
Figure 6.6: Pressure distribution at various L_3 values
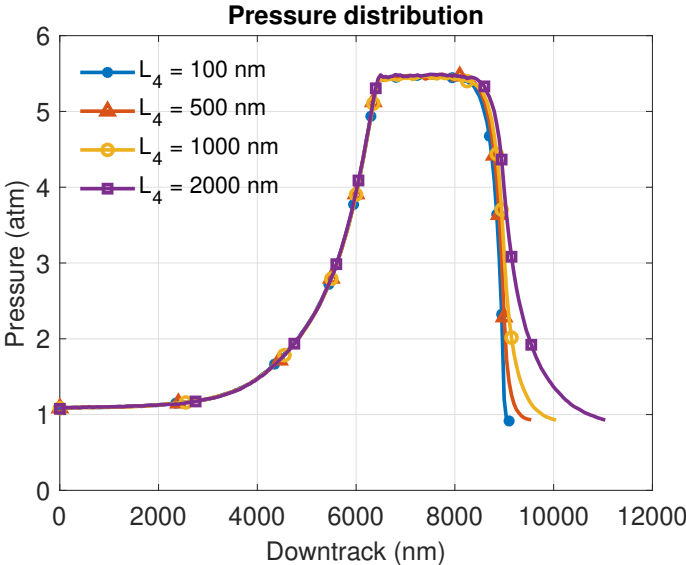
Figure 6.7: Pressure distribution at various L_4 values

Other gases

A similar simulation was conducted for three other gases - helium, oxygen, and nitrogen. This was to check if the simulation domain is sufficient to maintain a zero pressure gradient boundary condition at the inflow boundary. The results are plotted in Fig. 6.8. All the gases demonstrate that the 11000 nm simulation length is sufficient to maintain the proper

boundary conditions. Helium shows a slight deviation in peak pressure from the other gases. Although the pressure gradient near the entry looks to be zero, all length parameters were increased by 50% to further reduce any errors.
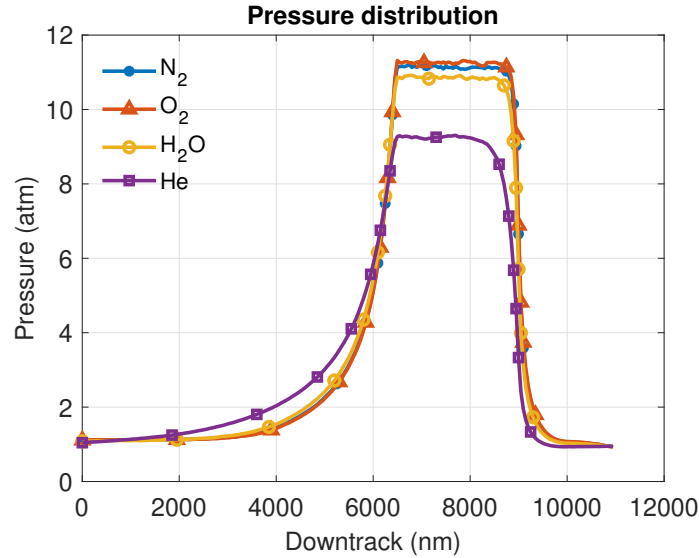
Figure 6.8: Pressure distribution for various gases

Time of simulation

Adding up the total length, we need a simulation domain of about 10,000 nanometers. It results in an aspect ratio of 200:1. Since the airflow is only on the channel ends, it would take a long time before the system reaches equilibrium. So, monitoring the simulation before any parameters are averaged to reduce statistical error is important. Fig. 6.9 shows a simulation in which the pressure distributions are plotted against the number of timesteps before an average was taken. The results show that the peak pressure reaches a steady state after about 60000 steps for all the gap (G_l) values. Therefore, all subsequent simulations will start calculating the averages after at least $75,000$ timesteps to ensure a safe margin.

6.4 Results and Discussion

6.4.1 Simulation at Room Temperature

The first simulation is at 300 K in three different environments - helium, nitrogen, and oxygen. In all three cases, the pressure at the entrance and exit was fixed at 1 bar, and the humidity level was kept at 20%. At 300 K, the saturation pressure of water is approximately 3510 Pa; therefore, 20% humidity corresponds to around 700 Pa. The top and bottom sides of
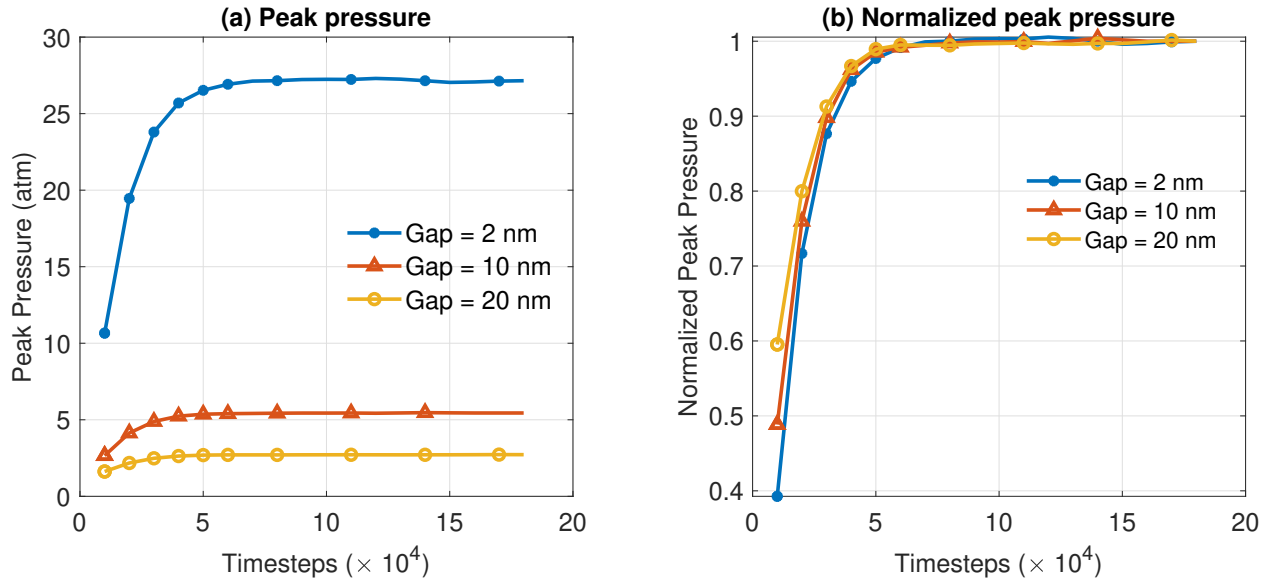
Figure 6.9: (a) The peak pressure calculated at various timesteps for gap values between 2 nm to 20 nm. (b) The same graph but normalized to aid in analysis

the channel were covered with 1000 surface elements. The pressure on each surface element was quantified to generate the pressure distribution curve along the length of the channel. The simulation was first allowed to run for 200,000 timesteps to reach equilibrium. Then, all quantities were calculated by averaging over 400,000 timesteps. For each gas-bearing, 12 simulations were performed with varying gap (G_p) values ranging from 1 nm to 50 nm. In each case, two values were quantified - the total pressure and the water vapor pressure. The total pressure arises from all particles that collide with the boundary, whereas the water vapor pressure comes from only the water molecules. The total and water vapor pressure were then further averaged over the surface elements in the channel length zone (Fig. 6.3). Fig 6.10 shows the total pressure as a function of the gap value. Fig 6.11a shows the water vapor pressure as a function of the total pressure. Although fig 6.11a implies that the water vapor pressure exceeds 3500 Pa at elevated pressures, the actual pressure would only reach 3510 Pa since we do not account for condensation. Therefore, using 3510 Pa as a ceiling for the absolute water vapor pressure, we plot the humidity as a function of pressure in Fig. 6.11b.

We observe that the pressure in the channel increases with decreasing gap (Fig. 6.10a). At 1 nm spacing, the pressure exceeds 40 bars. Oxygen and nitrogen show near-identical behavior due to the similarity in the diameter and weight of the respective molecules. On the other hand, helium exhibits significantly less pressure for the same gap value (Fig. 6.10a). This is related to the non-ideal gas effect, as seen in Fig. 6.10b. We also see that the partial pressure of the water molecules correspondingly rises with the total gas-bearing pressure. At about 5 bars of pressure, the partial pressure of water reaches the saturation pressure. This
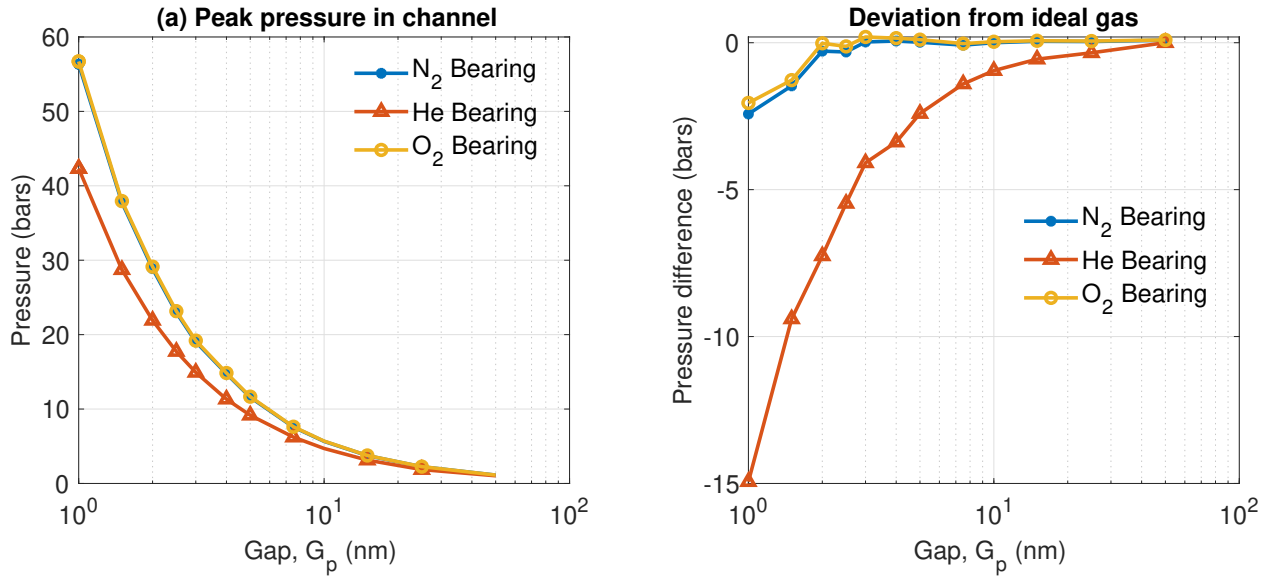
Figure 6.10: (a) Peak gas-bearing pressure in the channel at 300 K for a-bearing consistent of three different gases.(b) The deviation of the pressure from an ideal gas due to the consistent Boltzmann algorithm

would lead to the formation of a water layer on the disk and head surface [134]. The point at which the bearing approaches 100% humidity is 4.6 bars for helium and 5.4 bars for nitrogen and oxygen.

6.4.2 Simulation with Thermal Spot

The same simulation as in Sec. 6.4.1 was conducted again, except the surface temperature was varied along the channel, as shown in Fig. 6.12. It was raised to 800 K to prevent the saturation pressure from causing condensation on the surface. This allows for the existence of very high partial pressures at low humidity levels. Fig. 6.12 shows the total pressure as a function of the gap value, Fig. 6.13a plots the maximum pressure as a function of the gap value, and Fig. 6.13b plots the water vapor pressure as a function of the total pressure.

Fig. 6.13 shows that having an 800 K hotspot at the center of the channel results in an increase in the pressure, with the peak pressure being greater than 60 bars at 2 nm spacing. Further, since the saturation pressure at 800 K does not limit the water partial pressure, it can increase indefinitely. Fig. 6.12b shows a partial pressure greater than 50 kPa at 60 bars of pressure. The water vapor content is 15 times greater than in the room temperature simulation. Helium also deviates from nitrogen and oxygen by exerting lower pressure at a similar spacing. This also leads to the partial pressure being slightly higher at a given pressure. Ultimately, in both cases, the higher absolute pressure indicates that humidity plays a more significant role in HAMR, where disk surface temperatures exceed 600 K.
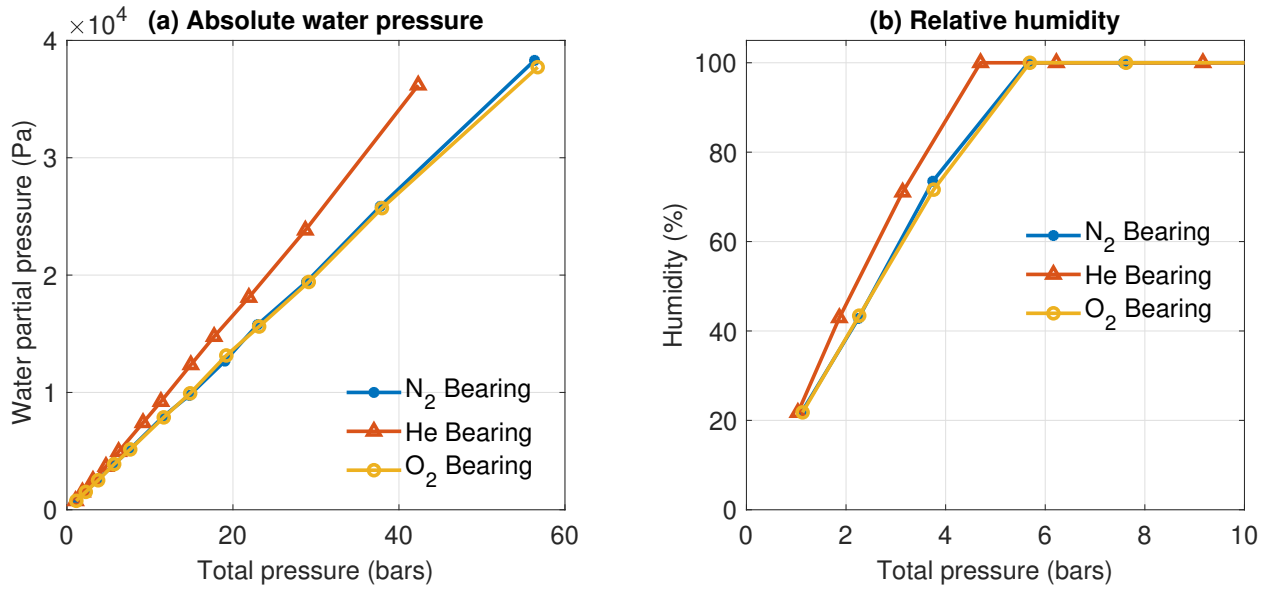
Figure 6.11: (b) Partial pressure of water as a function of the gas-bearing pressures at 300 K (b) Humidity level in the gas-bearing of different gases
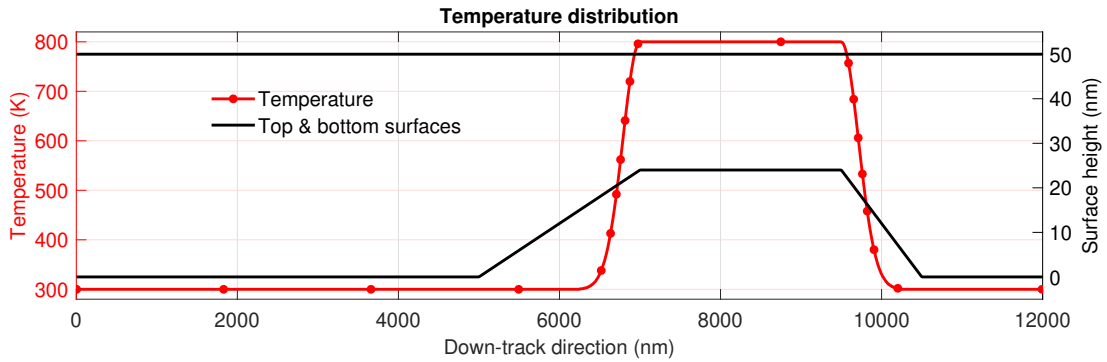
Figure 6.12: The temperature distribution in the channel (red) along with the channel cross-section (black)

6.4.3 Simulation with Head-Disk Temperature Gradient

In HAMR drives, a temperature gradient exists between the head and the disk as well. The head temperature is recorded to be around 500 K [88], and the disk temperature can be greater than 700 K [88]. Therefore, the same simulation as in Sec. 6.4.1 is conducted except that the peak temperature on the bottom surface was 500 K and the peak temperature at the top surface was 800 K. Since oxygen and nitrogen show similar behavior, only nitrogen and helium bearings were simulated. First, we plotted the total pressure and the water vapor
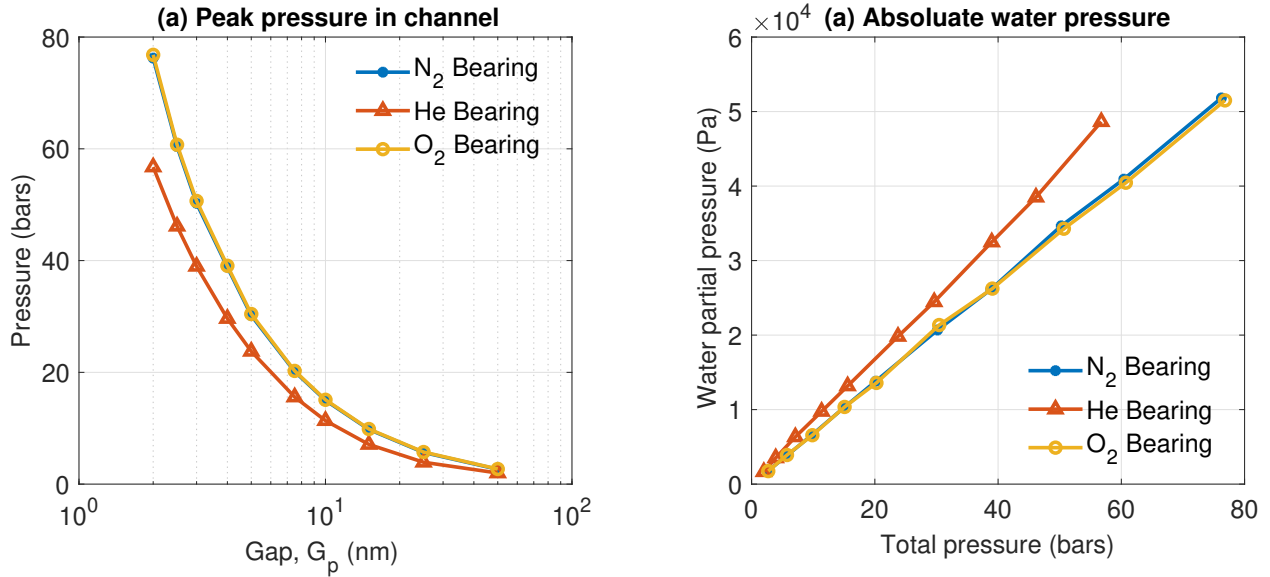
Figure 6.13: (a) Peak pressure in the channel with 800 K spot, (b) Partial pressure of water at various total pressures

partial pressure as in Sec. 6.4.2. We see a similar trend as earlier. The peak pressures do not reach as high as in Sec. 6.4.2, but still are higher than when the system is at room temperature. The humidity also increases to several kPA, indicating a higher concentration of water vapor molecules.

To investigate further, we plot the total pressure distribution at the top and bottom surfaces in Fig. 6.15. We observe that the pressure distributions on both surfaces are identical for helium and nitrogen. This must happen as any pressure gradient would lead to a net flux of particles to reach equilibrium. However, since the temperatures at the two surfaces differ by 400 K, the composition of the bearing at the two ends must differ to maintain equal pressure. The pressure depends on four quantities - the particle's mass, the number density, the temperature, and the correction term to account for non-ideal effects. The correction term, in our case, is the diameter of the particle (Eq. 6.11). Since the particle's properties are constant throughout each simulation, the only variation that accounts for the constant pressure is the gas temperature and number density. At the particle level, the temperature and number density make sense only in a non-zero volume rather than at a surface or a point. Therefore, we calculate these quantities at the grid cell adjacent to each surface element. The adaptive grid algorithm of Sec. 6.3 ensures that the dimension of the cell does not exceed the mean free path of a gas particle. Fig. 6.16 plots nitrogen bearings' number density and temperature distribution at 4 nm spacing. The solid lines mark the quantity along the bottom surface, and the dashed lines mark the quantity along the top surface. They show that the temperature and number density profiles follow different distributions at the top and bottom surfaces around the hotspot. This ensures that the pressure is equal even if
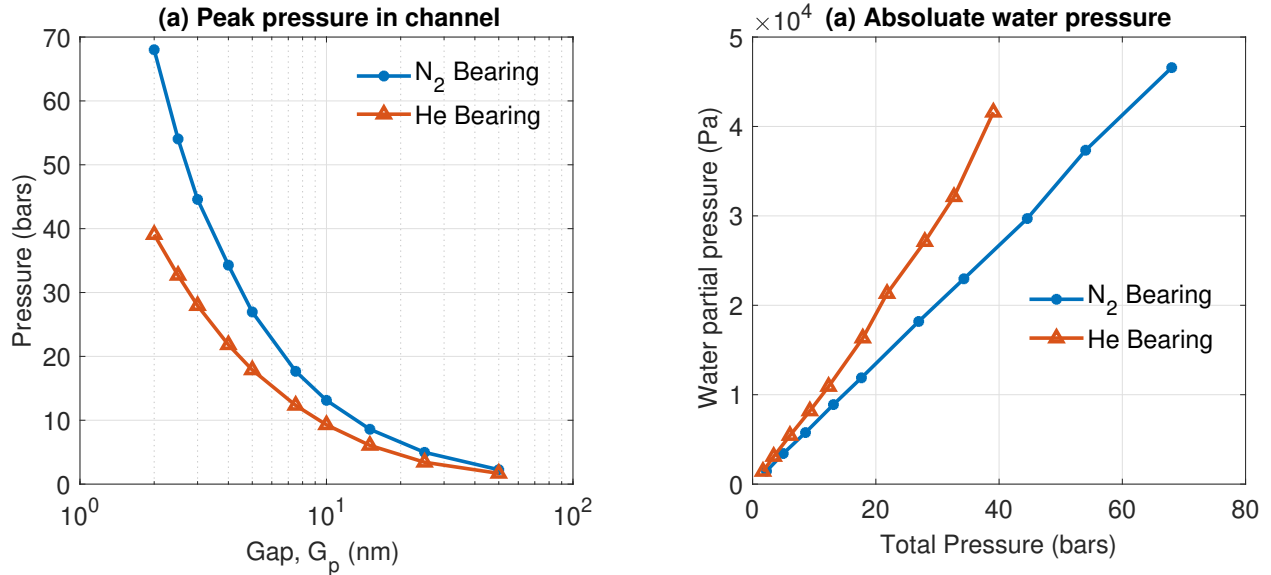
Figure 6.14: (a) Peak pressure in the channel with hotspot, (b) Partial pressure of water at various total pressures

the surface temperatures differ. In Fig. 6.17a, we plot the difference in number density at the top and bottom surface over a range of gaps. It shows that as the gap decreases, the difference increases between the two ends increases. As particles bounce off the surface, the diffusive boundary condition at the surfaces ensures that the kinetic energy of the particles corresponds to the surface temperature. Consequently, the particles bouncing off the hotter side have an average higher velocity than those from the cooler side. We can observe this in Fig. 6.18, where we plot the vertical component of the velocity along the down-track direction. As the particles traveling from the hotter to the colder surface have a larger mean speed than those traveling from the colder to the hotter surface the gas flow has a positive vertical drift, which ensures that the number density at the colder end remains the same. As the gap reduces, the absolute number density also increases, leading to an increase in number density jump between the ends.

Further, Fig. 6.17b shows the temperature difference between the two sides. We observe a consistent 20 to 40 Kelvin temperature difference between the two ends, with the gas temperature at the top being the higher. This contrasts the difference in the top and bottom surface temperatures of 800 K and 500 K, respectively. This is because the mean free path of the particles is limited by the gap. For example, at 600 K, the mean free path of helium gas at 40 bars pressure is around 9 nm (Eq. 6.12), lower than the corresponding gap of 2 nm. As a result, many particles undergo a ballistic trajectory from each surface. Therefore, regardless of the point along the vertical direction, the velocity distribution of the molecules is defined by the ratio of particles that ballistically travel from the top and bottom surface. Since the trajectory of the particles is almost ballistic, this ratio does not vary significantly
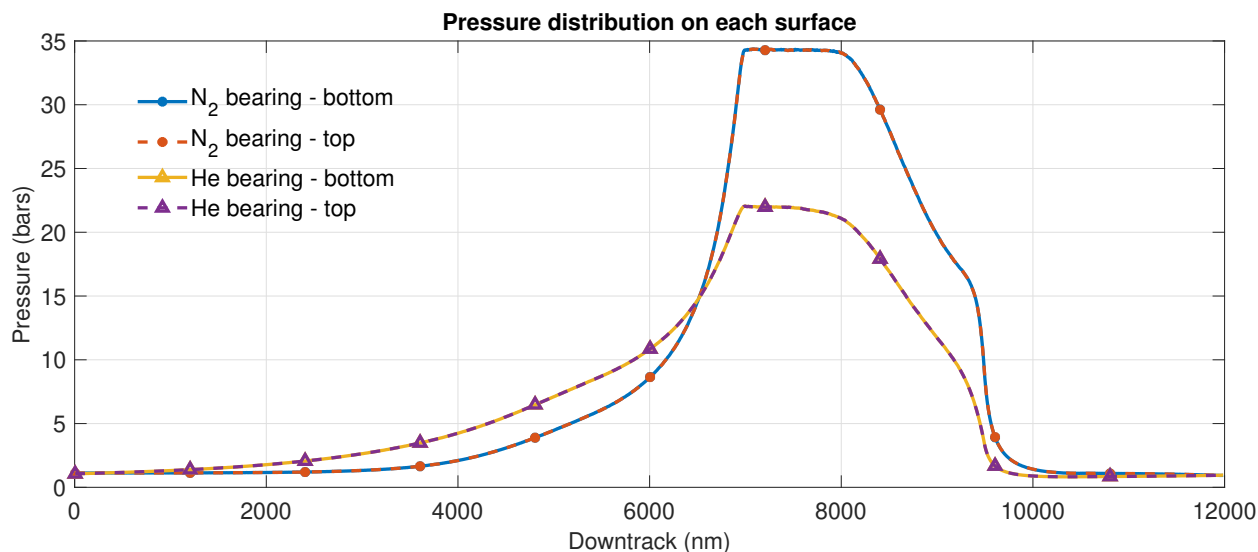
Figure 6.15: Pressure distribution along the top and bottom surface for helium and nitrogen bearings at 4 nm gap

along the vertical direction. This results in the temperature being approximately the average of the top and bottom surfaces.

6.5 Conclusions

This chapter studied the effects of the head and disk hotspots on the gas-bearing with nanoscale gaps using a modified direct simulation Monte Carlo. A 2D channel was developed to represent a simplified head-disk interface. Appropriate boundary and initial conditions were imposed to conduct simulations. Three sets of simulations were conducted. First, a simulation at room temperature, which simulates conventional hard disk drives. Second, a simulation with an 800 K hotspot at the center of the channel. Finally, we conducted the simulation using conditions found in HAMR drives - a hotspot in the center with 800 K at the top and 500 K at the bottom. That is, with temperature gradients in the horizontal and vertical direction.

The first simulation at room temperature indicated that a 20% ambient humidity resulted in a 100% relative humidity at the bearing pressures greater than 5 bars. The limiting factor was the saturation pressure of water. Therefore, in g bearings with pressures exceeding 20 bars, the relative humidity under the sliders can be 100%, even at low ambient humidity. This would lead to water vapor condensing on the disk and head surface. In contrast, placing a hot spot at the center of the channels allows for the existence of very high partial pressure of water vapor due to the elevated saturation pressure of water at high temperatures. The peak water pressure was about 40 kPa, which is several times the maximum water content at
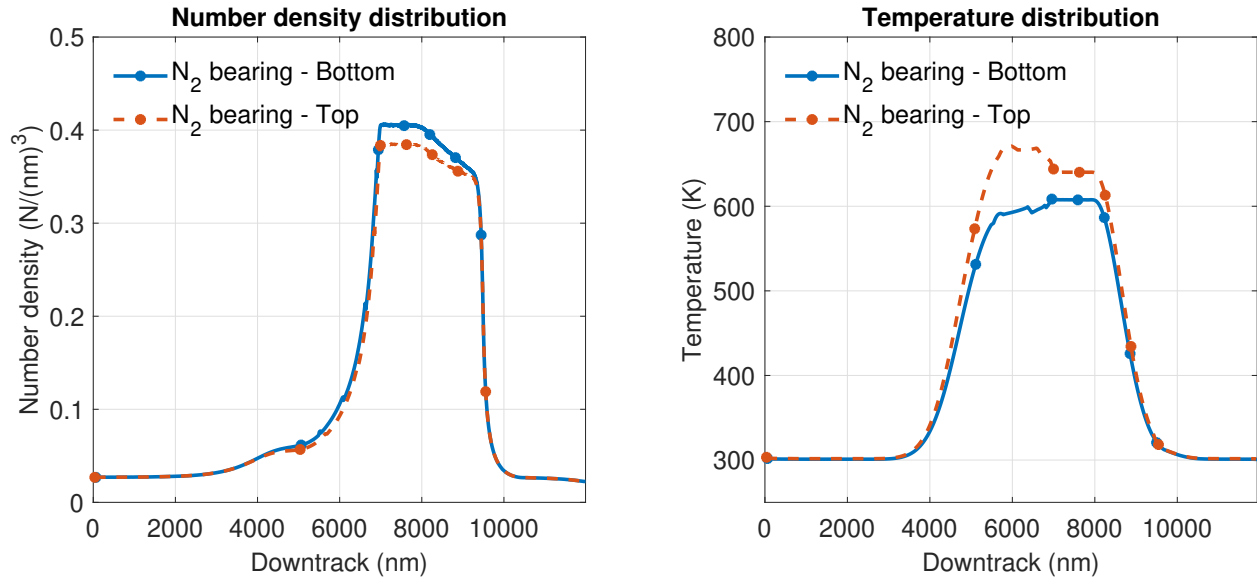
Figure 6.16: (a) Number density distribution along the top and bottom surface for nitrogen-bearing with 4 nm gap (b) Temperature distribution along the top and bottom surface for nitrogen-bearing with 4 nm gap

room temperature.

Finally, in the HAMR-like simulation, we observed that pressure at each surface remains exactly the same. However, to account for the different surface temperatures, the number density and temperature at a grid cell adjacent to the surfaces were different. The temperature difference (and gradient) in the gas itself was found to be less than the surface temperature differences due to the very short mean free path. Further, each end also contains a different number of densities due to a vertical drift. This drift equalizes the pressure on each surface. This drift is also observed for water molecules, indicating its increased presence near the cooler surface. Since in HAMR, the head is cooler than the disk; there can be a vertical drift from the disk surface that can carry other particles along. The cooler head can also lead to condensation that initiates smear buildup. Therefore, this drift is one possible mechanism that can drive smear growth in HAMR head-disk interfaces.
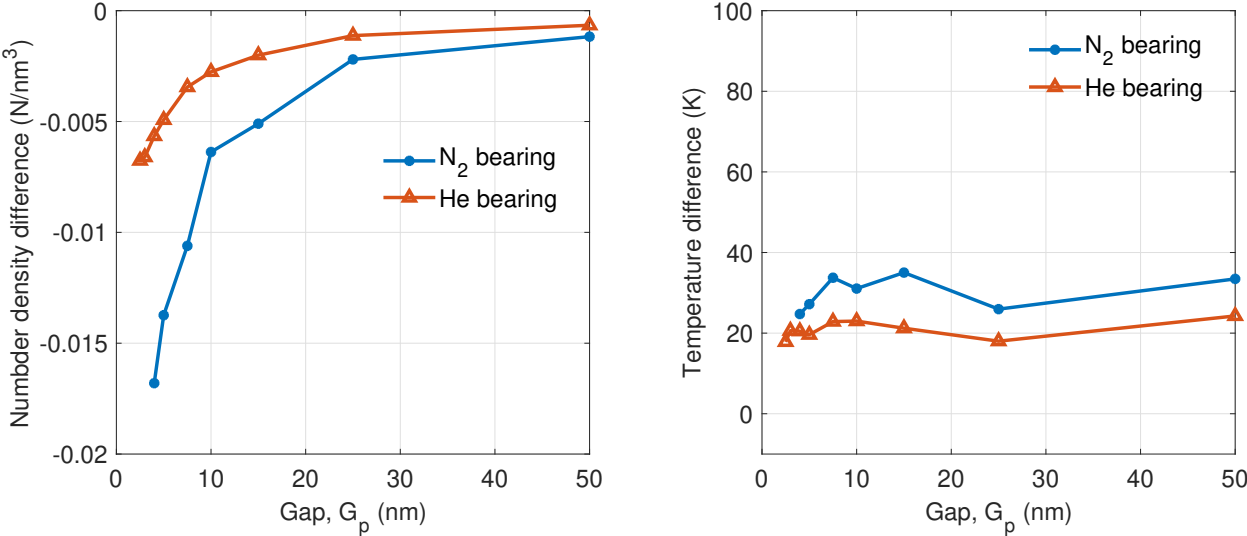
Figure 6.17: (a) The average difference in the number density for gas bearings at different gap values (b) The average temperature difference for gas bearings at different gap values
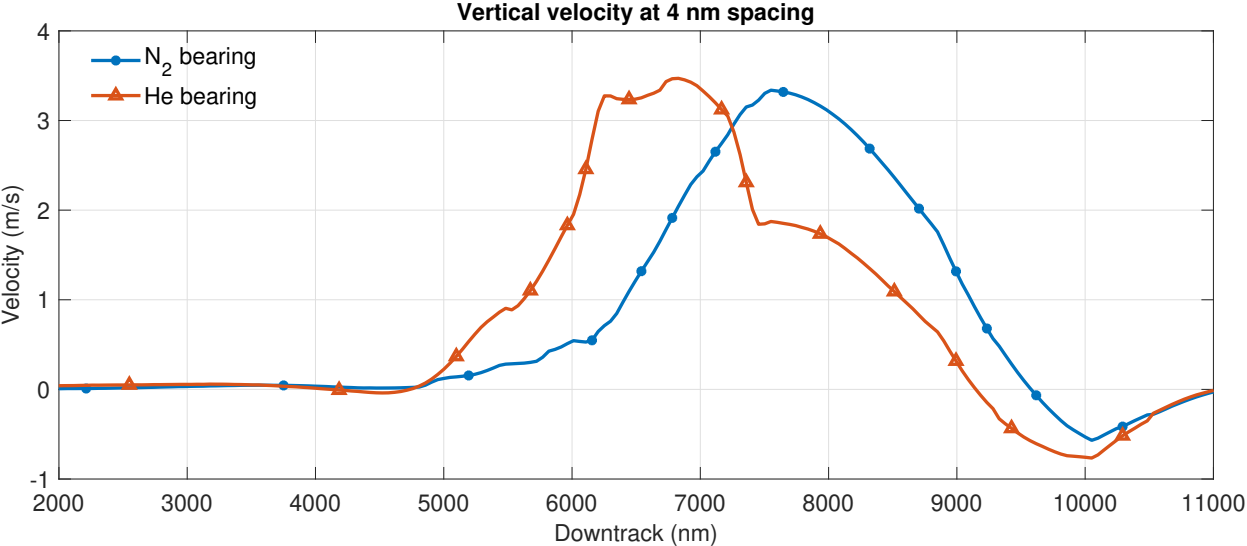
Figure 6.18: The vertical component of the gas velocity for nitrogen and helium bearings at 4 nm gap

Chapter 7

Ballistic Jumps in the Head-Disk Interface

7.1 Introduction

Chapters 3 and 4 considered the scenario with a head-disk spacing that allows sufficient air molecules to exist. Further, chapter 6 showed that in the head-disk spacing of less than a few nanometers, the air molecules ballistically travel between the head and disk surfaces. Any collisions of smear particles with the gas molecules will be negligible compared to collisions with the head and disk surface. The head disk space will behave like a rarified gas, with particles traveling ballistically between surfaces. In the absence of gas molecules, the dominant forces will be forces from the head and disk surfaces. In chapter 3, we investigated one kind of electromagnetic force - the optical force arising from the electric field gradient. However, the optical force also was calculated to be highly dependent on the volume of the nanoparticle. Under very small spacing, the nanoparticles are a single atom/molecule with negligible volume. Therefore, optical forces may not be relevant in these cases. However, the close spacing gives rise to another electromagnetic force - van der Waals interactions. These short-range forces can act over distances of a few nanometers. Since the head is cooler than the disk, the van der Waals forces can be much higher, resulting in the contaminant being picked up by the head as it flies over the disk. In Sec. 7.2, we describe the model to quantify the disk-to-head ballistic jumps. Then, in Sec. 7.3, we conduct a parametric analysis over various materials to understand the conditions where they can be significant. Finally, we draw some conclusions that affect the pick-up of smear in Sec. 7.4. A part of this chapter was presented in TMRC 2023 [127].

7.2 Modeling

We analyze the phenomenon by modeling it as a three-body problem. The head and the disk are modeled as smooth half spaces separated by a distance h_d. Then, a spherical nanoparticle

with a radius R is placed between the half-spaces, as shown in Fig 7.1.
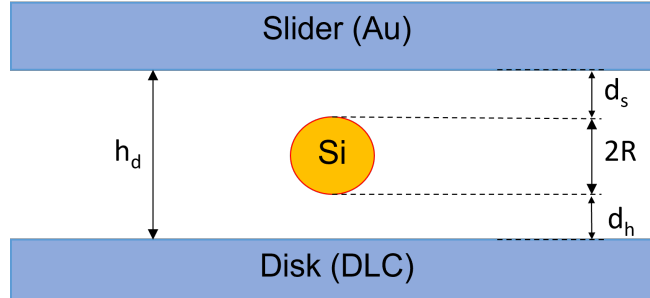
Figure 7.1: Schematic of the 3-body problem

where ϵ is the dispersion energy (the depth of the potential well) and σ is the distance at which the potential is zero (referred to as the kinetic radius of the particle).

$$V = 4\epsilon \left[\left(\frac{\sigma}{r} \right)^{12} - \left(\frac{\sigma}{r} \right)^{6} \right] = \frac{C_1}{r^{12}} - \frac{C_2}{r^6} \tag{7.1}$$

By applying the principle of superimposition, we can calculate the interactions between macro-sized bodies. For a sphere and a surface. separated by a distance D, the interaction energy U between them can be calculated as [131]:

$$U(D) = \frac{\pi^2 \rho_1 \rho_2 R}{D} \left(\frac{C_1}{1260 D^6} - \frac{C_2}{6} \right) \tag{7.2}$$

where ρ_i is the molecular number density (moles per unit volume) of the two bodies. In our case, the two half-spaces exert a force on the spherical nanoparticle. Hence, the net energy of interaction is given by:

$$U_{net} = U_1(d_h) + U_2(d_s) \tag{7.3}$$

In our analysis, we considered the lower half-space to be made of carbon (representing the DLC layer) and the upper half-space to be made of gold (representing the NFT). For simplicity, the spherical particle was assumed to be pure silicon. Then, using the parameters taken from various literature (Table 7.1), the potential for a head-disk spacing of 4 nm is plotted in Fig. 7.2.

The graph shows the existence of two potential wells in the head-disk interface. One is near the disk, and the other is near the head. The respective locations are marked d_1 and d_3 in Fig 7.2. A particle that travels from the disk to the head needs to overcome the barrier energy, which is the difference in the potential at the minima (d_1 or d_2) and the maxima (d_2). The approximate solutions for d_i can be calculated by appropriate simplifications. Since d_1 is

Material	C_1 (J/mol nm^{12})	C_2 (J/mol nm^6)	ρ (kmol/m^3)
Silicon [157]	7.7177e-4	0.7188	82.64
Gold [158]	9.65e-3	29.22	98.04
Carbon [159]	1.07e-2	3.5143	188.68

Table 7.1: Material properties to calculate potential well in Fig. 7.2
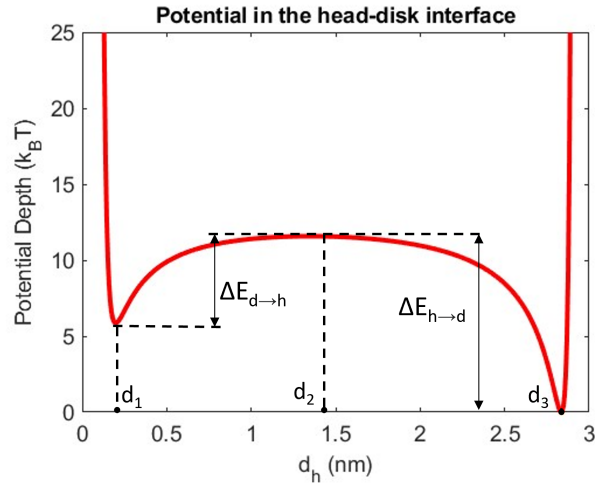
Figure 7.2: Potential of a spherical particle in the head-disk interface

located near the disk, the disk surface atoms will dominate the forces. So, we can assume that $U_1(d_h) >> U_2(d_s)$ and write,

$$U_{net} \approx U_1(d_h) \tag{7.4}$$

$$\Rightarrow d_1 = \min\left(U_1(d_h)\right) \tag{7.5}$$

Then, by differentiating the potential function over distance, we can calculate the minima to be,

$$d_1 = \sqrt[6]{\frac{C_{d,1}}{30C_{d,2}}} \tag{7.6}$$

$$\tag{7.7}$$

where the subscript d refers to the disk. Using similar reasoning on the other of the plot in Fig. 7.2, we can calculate d_3 by replacing U_2 in Eq. 7.4 to get

$$d_3 = h_d - \sqrt[6]{\frac{C_{s,1}}{30C_{s,2}}} \tag{7.8}$$

the subscript s refers to the slider. The location d_2 then is approximately the between d_1 and d_2. The energy barriers can then be calculated to be.

$$\Delta E_{d \to h} = 7.78 k_B T_{room} \tag{7.9}$$

$$\Delta E_{h \to d} = 15.62 k_B T_{room} \tag{7.10}$$

where $d \to h$ refers to the barrier for a particle traveling from the disk to the head and $h \to d$ refers to the barrier for a particle traveling from the head to the disk. k_B and T are the Boltzmann constant and temperature. If we consider that the particle follows Boltzmann law, then the probability that the particle has the required energy to complete the jump is given by:

$$P(E > E_0) = e^{-\Delta E / k_B T} \tag{7.11}$$

But, even if a particle possesses enough energy, it is possible that it encounters collisions with other particles in the air bearing. Therefore, we adjust this probability by a factor that accounts for possible collisions. Analogous to the Beer-Lambert law, if l_p is the free path, and l is the mean free path, then the probability that a particle's free path is greater than the head-disk spacing is given by:

$$P(l_p > h_d) = e^{-h_d / l} \tag{7.12}$$

We make a reasonable assumption that the event of a nanoparticle possessing sufficient energy $(P(E > E_0))$ and the event that a trajectory is ballistic $P(l_p > h_d)$ are independent. The total probability that a nanoparticle travels from the disk to the head is the product of the individual probabilities and is given by,

$$P_{net} = e^{-\Delta E_{d \to h} / k_B T_{disk} - h_d / l} \tag{7.13}$$

If we know the nanoparticle density on the disk surface (N per unit area), the peak temperature radius of R_T, and a slider velocity, v, then the rate of particles being transported from the disk to the head is:

$$r = 2 R_T v N P_{net} \tag{7.14}$$

7.3   Results

We begin our simulation by considering the different kinds of smears on the head surface. Experiments have revealed a variety of components. For example, Lee et al. [160] found the presence of fluorine, iron, chromium, aluminum, platinum, and silicon. Xiong et al. [48] found iron, magnesium, sodium, and PFPE lubricants. Kiely et al. [36] found silica. To simplify the analysis, we classify the materials into three categories. The first is a metallic smear, which is characterized by a large density (ρ) and dispersion energy (ϵ) but with a very

Material	M (g/Mol)	σ (Å)	ϵ/k_B (K)	ρ (kg/m^3)
Head (Au)	197	2.569	5310.1	19300
Disk (C)	12.011	3.385	30.6	3530
Metals (Fe)	59	2.319	4658	7800
Organics	75	5.85	45	1850
Inorganics (SiO$_2$)	60	3.2	294	2650

Table 7.2: Representative properties of the head, disk, and nanoparticles. Values taken from [161] and [162]

small molecular size (r). The second category is organic smear, which includes the PFPE molecules. They are characterized by a large molecular size (r), small dispersion energy (ϵ), and low density (ρ). Finally, the third category is an inorganic smear, mainly composed of silicon (Si) or silica (SiO$_2$) with properties that are intermediate from metallic and organic smear. The representative properties are tabulated in Table 7.2

We then prescribe the head and disk temperature to be 800 K and 500 K, respectively. The air bearing pressure was taken to be 20 bars, which corresponds to a mean free path of 3.25 nm. The size of the nanoparticle was kept at 4 Å. Then, the fraction of particles that ballistically travel to the head was calculated for a given head-disk spacing and plotted in Fig. 7.3. We immediately see that at very low spacing (< 1.5Å), the head picks all of the nanoparticles up. Metallic particles show the steepest gradient, with particles being picked up when the spacing is less than a critical value. For nonmetals (organics and inorganics), the increase is more gradual. Organic nanoparticles are picked up in the least amount. Metals have this sudden jump because of the large potential depth induced by the large dispersion energy.

7.3.1 Effect of Size

Since the nanoparticles in the air bearing and the disk surface can have a range of sizes, we perform a simulation to see the effect of particle sizes on the smear pickup. We consider metallic and organic nanoparticles of sizes varying from 2Å and 10Å in similar head-disk interface conditions as earlier. The results, plotted in Fig. 7.4, show that increasing the particle size increases the critical head-disk spacing at which the head picks the particle up. This is primarily because increasing the particle size decreases the clearance (d_h, d_s in fig. 7.1) between the nanoparticle and either surface. The critical head-disk spacing, therefore, also increases with nanoparticle size to maintain a similar clearance. We also notice the gradient increases with increasing size of organic particles.
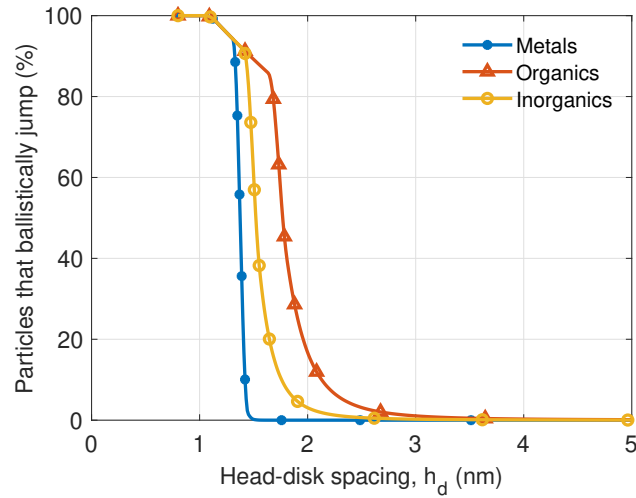
Figure 7.3: Percentage of particles that travel ballistically to the head at various head-disk spacing. The radius of the particle is 4 Å
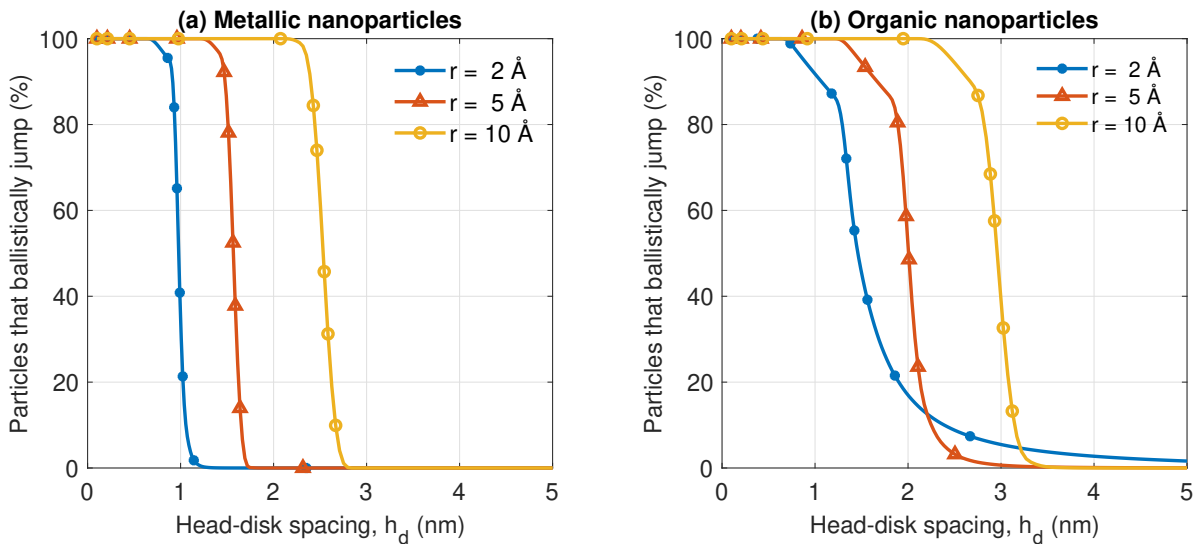
Figure 7.4: Dependence of size on particles that travel ballistically to the head. (a) Metallic nanoparticles, (b) Organic nanoparticles

7.3.2   Effect of Existing Layer of Smear

Just as in section 3.4.3, we now simulate the nanoparticle pickup probability when the head is covered with a layer of smear. We consider two kinds of smear layers - organic and inorganic. The parameters from Table. 7.2 differentiates the two layers. The fraction of particles that ballistically jump to the head is plotted in Fig. 7.5. We also plot the case without a smear

layer (Clean Head) for comparison, along with the two kinds of smear layers. The critical head-disk spacing for metallic nanoparticles increases by 1Å for the organic layer and 0.4Å for the inorganic layer. Meanwhile, the difference is slightly higher for organic particles at about 5Å. We also observe that the plots are much sharper in the presence of the smear layer. In the case of the organic nanoparticle with an organic layer on the head, we must consider other intermolecular forces as they are more influential than van der Waals forces.
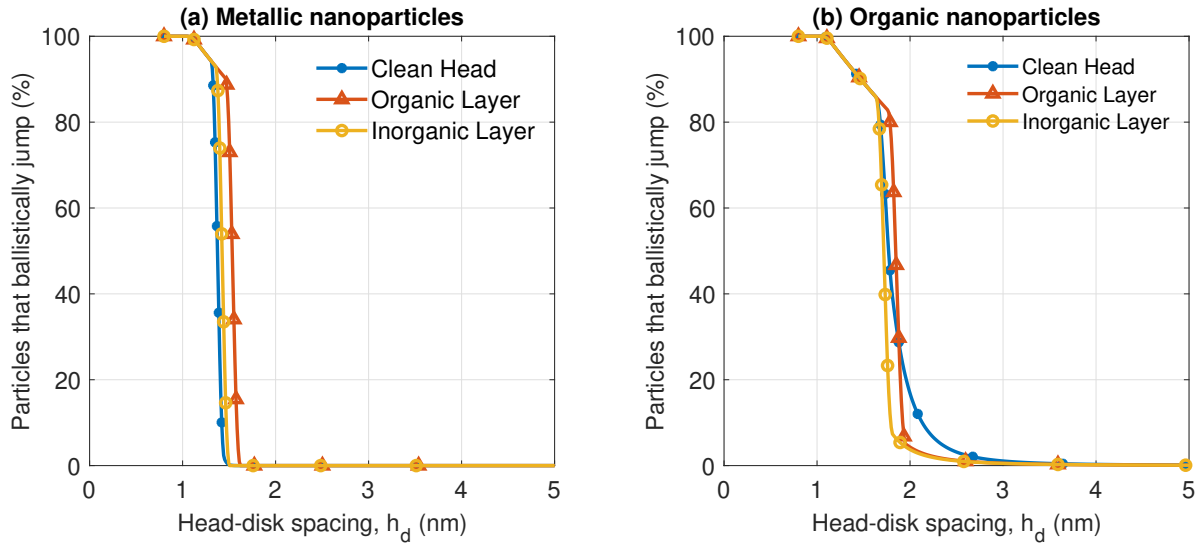
Figure 7.5: Dependence of head smear on particles that travel ballistically to the head. (a) metallic nanoparticles, (b) organic nanoparticles

7.4 Conclusions

In this chapter, we studied the case when smear pickup occurs at ultra-low spacing in the form of ballistic jumps from the disk to the head. We modeled the system as a three-body problem and applied the Lennard-Jones potential to quantify the interactions between the different bodies. We found that the existence of a critical head-disk spacing below which a majority of nanoparticles would be ballistic. The relatively cooler head would then readily pick up these contaminants. A sensitivity analysis of the size revealed that larger particles are more susceptible to these pickups due to the lower clearance. We also saw that the probability of ballistic transport remains the same in the presence of an existing smear layer on the head.

Chapter 8

Conclusions

8.1   Summary of Results

This dissertation advances the understanding of smear buildup in the head-disk interface. We focused on quantifying the forces and tracking smear buildup using a particle-level view of smear. Chapter 1 introduced the technology behind hard disk drives, focusing on heat-assisted magnetic recording. Then, we showed the importance of studying smear and the challenges associated with the continuum analysis and molecular dynamics methods.

Then, in chapter 2, we described classical continuum analysis to study the disk temperature, the head temperatures, and the head protrusion. The temperature spikes on the head and disk were observed in several hundred Kelvin. Further, we quantified the head surface protrusion to several angstroms. However, the magnitude of the temperature spots was observed to be more significant than the protrusion.

Chapter 3, we introduced the concept of smear nanoparticles and studied a novel force in the head-disk interface. Along with the temperature field, the head-disk interface was also found to contain a large electric field gradient on account of the surface plasmon on the NFT. This force, called optical force, was found to be able to generate a trap right under the NFT. We discovered metallic and highly eccentric particles are more susceptible to being trapped than spherical and dielectric particles. Furthermore, the area around larger metallic particles generated an optical trap that can even attract non-metallic contaminants.

Then, in Chapter 4, calculated the thermophoretic, drag, and lift forces on a smear nanoparticle. Then, in Chapter 5 we used the resulting force field to conduct a novel simulation to track the trajectory of smear nanoparticles on the head. The smear buildup that was observed was the first numerical method to generate smear patterns observed in experiments. The various patterns were explained, which can help the design reduce smear buildup in the head-disk interface.

In Chapter 6, we used the DSMC method to study the gas-bearing characteristics under very low spacing and high temperatures. We observed that the temperature of the gas bearing itself is the average of the disk and head temperatures. This occurs as the gas-bearing

molecules are effectively rarefied in ultra-low spacing conditions. Thus, most of the molecules travel ballistically between the two surfaces. Further, two distinguishing features were the presence of a vertical drift that would allow more airborne particles to aggregate the cooler head and high water vapor pressures.

Finally, in chapter 7, we looked at the case of ultra-low flying conditions where the head-disk interface is absent of air-bearing atoms/molecules due to the lack of space. We developed the idea of the imbalance of van der Waals forces on the head and disk surface. The rate equations showed that the ballistic jumps can significantly cause particles to accumulate on the head. This effect is very significant when the spacing is less than 2 nm.

8.2 Smear Mitigation Strategies

The summary of the results clearly shows that various mechanisms can be responsible for the buildup of smears. We see that thermophoresis, drag force, optical, and van der Waals forces can contribute to the growth of smear. Each force dominates in a specific scenario. There are many more mechanisms to investigate, including thermal decomposition, rogue pickup of contaminants, etc. However, the clear conclusion is that there is more than one method of smear formation.

This also means that the smear mitigation strategies must be much more robust. Passive designs of smear mitigation may not be sufficient. Instead, active cleaning of the head-disk interface is required. Multiple active cleaning mechanisms have been suggested [51]. However, the lack of widespread commercialization implementation indicates the need for further development.

We know that in an actual head-disk interface, various parameters, such as pressure, temperature, and head-disk spacing, vary greatly at different locations. Since the sensitivity analysis and smear growth simulations show that these parameters are critical in determining the dominant force and growth characteristics, proper tuning can aid in controlling the growth of smear. Since thermophoresis grows faster than drag force with PFPE molecule dimensions, mechanisms such as thermal decomposition that break smear particles can help reduce smear buildup. Further, larger and heavier gas molecules show a net decrease in thermophoresis and an increase in drag force. Therefore, having such molecules can suppress smear buildup. Next, since pressure increases the drag force, designing the air-bearing surface (ABS) to give higher peak pressures in areas with higher susceptibility for smear will be helpful. Further, reducing the temperature gradient and increasing the speed of disk rotation can also reduce smear. Finally, from the smear simulation study, we notice that the smear streaks caused by the oscillations in temperature gradient are much thinner than central streaks. Therefore, designing such oscillations may be helpful. However, care must be taken to avoid other secondary effects from such oscillations.

The optical forces show yet another potential area to utilize to control smear growth. One candidate is the presence of a secondary surface plasmon on the large metallic contaminant. This secondary plasmon exhibits a very strong optical trap. Therefore, if a controlled metallic

particle or protrusion exists on the disk surface, then it would cause the head smear to transfer to the protrusion when the head flies over it. This would effectively clean the head surface. We would have an active cleaning mechanism if this periodic cleaning occurs during HAMR operation.

8.3 Future Research

Several challenges remain in understanding smear and controlling. Future research in smear control must integrate simulation and experiments. A close relationship between them can lead to better results. Although the methods presented in this dissertation generally agree with experiments, the author believes that a continuous iteration between experiments can refine the simulation methods to the point where they can accurately predict the behavior of the HDI for a given design.

This dissertation quantified forces on thermophoresis, drag, lift, optical, and van der Waals forces. However, only the first three were used to determine PFPE lubricant kinetics and growth. Therefore, incorporating all the forces can yield a more comprehensive view of smear growth. Further, we can obtain the smear's distribution if we include nanoparticles of different materials, sizes, and shapes. Here, experimental analysis of smear can further increase the reliability of the simulation method. For example, A TOF-SIMS analysis of the contribution of the smear observed in experiments can inform the rate of evaporation, van der Waals forces, etc. The physical characteristics of smear, such as the size of its constituents, can inform the initial conditions.

Further studies are needed to understand how optical forces depend on NFT designs. Future investigations can also explore more complex optical force models with additional considerations. One crucial consideration is the permittivity of the different materials. We assumed the smear nanoparticles have the same permittivity as their bulk counterparts. However, the extremely small size of the particle would alter the permittivity. The effect of the modified permittivity values would be of interest. Another area to investigate would be to look beyond the Rayleigh approximation to calculate the exact force on a smear nanoparticle. Maxwell's equations can be used to calculate the scattered electric and magnetic fields. These fields can then be used to calculate the exact optical force using Maxwell's stress tensor method (Eq 3.2). The results can then be used to compare the validity of the Rayleigh approximation used here.

The existence of the vdW-induced jumps presents exciting potential for further development. Even though the disk surface's smoothness is state-of-the-art, surface roughness remains in the order of a few nanometers. Therefore, the nanometer-level flying slider can occasionally fly over the peak. The relatively cooler head can pick up materials due to the high van der Waals force. The numerical method can be further tuned using more accurate material parameters and diffusion conditions of the materials. Of particular importance would be calculating the van der Waals forces on PFPE nanoparticles, especially the long chains that may 'catch' the head and be dragged along with it.

The author wishes to close this dissertation by expressing appreciation for the hard work of engineers and scientists in developing this remarkable technology. It is exciting that Seagate has finally introduced HAMR to select enterprise customers. The author eagerly waits for the day when HAMR can be purchased from Best Buy and integrated into a home network-attached storage (NAS) system.

Bibliography

[1] Market Trends. *What's the Next Step for the Data-Driven World? 2022 and Beyond.* 2020. URL: https://www.analyticsinsight.net/whats-the-next-step-for-the-data-driven-world-2022-and-beyond/ (visited on 01/10/2024).

[2] Petroc Taylor. *Amount of data created, consumed, and stored 2010-2020, with forecasts to 2025.* 2023. URL: https://www.statista.com/statistics/871513/worldwide-data-created/ (visited on 01/05/2024).

[3] Seagate. *Why HDDs Dominate Hyperscale Cloud Architecture.* 2020. URL: https://www.seagate.com/blog/why-hdds-dominate-hyperscale-cloud-architecture/ (visited on 01/10/2024).

[4] Computer History Museum. *1956: first commercial hard disk drive shipped.* 2024. URL: https://www.computerhistory.org/storageengine/first-commercial-hard-disk-drive-shipped/ (visited on 01/10/2024).

[5] Western Digital. *Ultrastar DC HC680 Data Center HDD.* 2023. URL: www.westerndigital.com/products/internal-drives/data-center-drives/ultrastar-dc-hc680-hdd?sku=ultrastar-dc-hc680-26tb-se (visited on 01/05/2024).

[6] Siddhesh V. Sakhalkar. "Nanoscale Lubricant Flow and Heat Transfer at the Head-Disk Interface in Hard Disk Drives". English. PhD thesis. 2020, p. 155. URL: https://www.proquest.com/dissertations-theses/nanoscale-lubricant-flow-heat-transfer-at-head/docview/2554459439/se-2.

[7] S. N. Piramanayagam. "Perpendicular recording media for hard disk drives". In: *Journal of Applied Physics* 102.1 (July 2007). ISSN: 1089-7550. DOI: 10.1063/1.2750414. URL: http://dx.doi.org/10.1063/1.2750414.

[8] Adrian Cho. "Effect that Revolutionized Hard Drives Nets a Nobel". In: *Science* 318.5848 (Oct. 2007), pp. 179–179. ISSN: 1095-9203. DOI: 10.1126/science.318.5848.179. URL: http://dx.doi.org/10.1126/science.318.5848.179.

[9] Bor-Yuan Jiang et al. "Tunneling magnetoresistive devices as read heads in hard disk drives". In: *Journal of Magnetism and Magnetic Materials* 571 (Apr. 2023), p. 170546. ISSN: 0304-8853. DOI: 10.1016/j.jmmm.2023.170546. URL: http://dx.doi.org/10.1016/j.jmmm.2023.170546.

[10] Akihiko Aoyagi et al. "Helium sealed hard disk drive". In: *Journal of Magnetism and Magnetic Materials* 564 (Dec. 2022), p. 170146. ISSN: 0304-8853. DOI: `10.1016/j.jmm m.2022.170146`. URL: `http://dx.doi.org/10.1016/j.jmmm.2022.170146`.

[11] Vineet Gupta. "Air bearing slider dynamics and stability in hard disk drives". PhD thesis. University of California, Berkeley, 2007.

[12] Jinglin Zheng and David B. Bogy. "Investigation of Flying-Height Stability of Thermal Fly-Height Control Sliders in Lubricant or Solid Contact with Roughness". In: *Tribology Letters* 38.3 (Apr. 2010), pp. 283–289. ISSN: 1573-2711. DOI: `10.1007/s11249-010-9 607-3`. URL: `http://dx.doi.org/10.1007/s11249-010-9607-3`.

[13] Nikhil Potu Surya Prakash and Roberto Horowitz. "Data-Driven Robust Feedback Control Design for Multi-Actuator Hard Disk Drives". In: *IFAC-PapersOnLine* 55.37 (2022), pp. 131–138. ISSN: 2405-8963. DOI: `10.1016/j.ifacol.2022.11.173`. URL: `http://dx.doi.org/10.1016/j.ifacol.2022.11.173`.

[14] Zhi Chen, Nikhil Potu Surya Prakash, and Roberto Horowitz. "Adaptive Feedforward Reference Design for Active Vibration Rejection in Multi-Actuator Hard Disk Drives". In: *2022 American Control Conference (ACC)*. IEEE, June 2022. DOI: `10.23919/acc53 348.2022.9867241`. URL: `http://dx.doi.org/10.23919/ACC53348.2022.9867241`.

[15] Nikhil Potu Surya Prakash, Zhi Chen, and Roberto Horowitz. *System Identification in Multi-Actuator Hard Disk Drives with Colored Noises using Observer/Kalman Filter Identification (OKID) Framework*. 2021. DOI: `10.48550/ARXIV.2109.12460`. URL: `https://arxiv.org/abs/2109.12460`.

[16] Kaizhong Gao. "Architecture for Hard Disk Drives". In: *IEEE Magn. Lett.* 9 (2018), pp. 1–5.

[17] Nikhil Potu Surya Prakash et al. "Clustering Techniques for Stable Linear Dynamical Systems with applications to Hard Disk Drives". In: *IFAC-PapersOnLine* 56.3 (2023), pp. 529–534. ISSN: 2405-8963. DOI: `10.1016/j.ifacol.2023.12.078`. URL: `http://d x.doi.org/10.1016/j.ifacol.2023.12.078`.

[18] R. Wood. "The feasibility of magnetic recording at 1 Terabit per square inch". In: *IEEE Transactions on Magnetics* 36.1 (2000), pp. 36–42. DOI: `10.1109/20.824422`.

[19] Vassil Skumryev et al. "Beating the superparamagnetic limit with exchange bias". In: *Nature* 423.6942 (June 2003), pp. 850–853. ISSN: 1476-4687. DOI: `10.1038/nature016 87`. URL: `http://dx.doi.org/10.1038/nature01687`.

[20] Yunfei Ding et al. "Sub-Nanosecond Switching of Spin-Transfer-Torque Device for Energy-Assisted Perpendicular Magnetic Recording". In: *IEEE Transactions on Magnetics* 58.4 (Apr. 2022), pp. 1–6. ISSN: 1941-0069. DOI: `10.1109/tmag.2021.3121812`. URL: `http://dx.doi.org/10.1109/TMAG.2021.3121812`.

[21] Anand Suresh, Garth Gibson, and Greg Ganger. "Shingled magnetic recording for big data applications". In: *Carnegie Mellon University Parallel Data Lab Technical Report CMU-PD L-12–105* (2012).

[22] Chris Mellor. *Western Digital spins out 10-platter drives*. 2022. URL: `https://bloc ksandfiles.com/2022/05/09/western-digital-10-platter-drives/` (visited on 06/28/2024).

[23] R.E. Rottmayer et al. "Heat-Assisted Magnetic Recording". In: *IEEE Transactions on Magnetics* 42.10 (Oct. 2006), pp. 2417–2421. ISSN: 0018-9464. DOI: `10.1109/tmag .2006.879572`. URL: `http://dx.doi.org/10.1109/TMAG.2006.879572`.

[24] Jian-Gang Zhu, Xiaochun Zhu, and Yuhui Tang. "Microwave Assisted Magnetic Recording". In: *IEEE Transactions on Magnetics* 44.1 (Jan. 2008), pp. 125–131. ISSN: 0018-9464. DOI: `10.1109/tmag.2007.911031`. URL: `http://dx.doi.org/10.1109 /TMAG.2007.911031`.

[25] H. J. Richter et al. "Recording potential of bit-patterned media". In: *Applied Physics Letters* 88.22 (May 2006). ISSN: 1077-3118. DOI: `10.1063/1.2209179`. URL: `http://d x.doi.org/10.1063/1.2209179`.

[26] C. D. Fuerst and E. G. Brewer. "High-remanence rapidly solidified Nd-Fe-B: Die-upset magnets (invited)". In: *Journal of Applied Physics* 73.10 (May 1993), pp. 5751–5756. ISSN: 1089-7550. DOI: `10.1063/1.353563`. URL: `http://dx.doi.org/10.1063/1.35 3563`.

[27] M.M. Yang et al. "Laminated CoPtCr/Cr films for low noise longitudinal recording". In: *IEEE Transactions on Magnetics* 27.6 (Nov. 1991), pp. 5052–5054. ISSN: 1941-0069. DOI: `10.1109/20.278737`. URL: `http://dx.doi.org/10.1109/20.278737`.

[28] H.Z. Yang et al. "Measurement of magnetic property of FePt granular media at near Curie temperature". In: *Journal of Magnetism and Magnetic Materials* 423 (Feb. 2017), pp. 27–33. ISSN: 0304-8853. DOI: `10.1016/j.jmmm.2016.09.071`. URL: `http://dx.doi.org/10.1016/j.jmmm.2016.09.071`.

[29] M.H. Kryder et al. "Heat Assisted Magnetic Recording". In: *Proceedings of the IEEE* 96.11 (Nov. 2008), pp. 1810–1835. ISSN: 1558-2256. DOI: `10.1109/jproc.2008.20043 15`. URL: `http://dx.doi.org/10.1109/JPROC.2008.2004315`.

[30] Nguyen Thanh Binh et al. "Influence of finite-size effects on the Curie temperature of $L1_0-$FePt". In: *Phys. Rev. B* 106 (5 Aug. 2022), p. 054421. DOI: `10.1103/PhysRev B.106.054421`. URL: `https://link.aps.org/doi/10.1103/PhysRevB.106.054421`.

[31] Barry C. Stipe et al. "Magnetic recording at 1.5 Pb m2 using an integrated plasmonic antenna". In: *Nature Photonics* 4.7 (May 2010), pp. 484–488. ISSN: 1749-4893. DOI: `10.1038/nphoton.2010.90`. URL: `http://dx.doi.org/10.1038/nphoton.2010.90`.

[32] Joanna Bechtel Dahl and David B. Bogy. "Static and Dynamic Slider Air-Bearing Behavior in Heat-Assisted Magnetic Recording Under Thermal Flying Height Control and Laser System-Induced Protrusion". In: *Tribology Letters* 54.1 (Feb. 2014), pp. 35–50. ISSN: 1573-2711. DOI: `10.1007/s11249-014-0305-4`. URL: `http://dx.doi.org /10.1007/s11249-014-0305-4`.

[33] Takuya Matsumoto et al. "Integrated head design using a nanobeak antenna for thermally assisted magnetic recording". In: *Optics Express* 20.17 (Aug. 2012), p. 18946. ISSN: 1094-4087. DOI: `10.1364/oe.20.018946`. URL: `http://dx.doi.org/10.1364/OE.20.018946`.

[34] Andreas Moser et al. "Magnetic recording: advancing into the future". In: *Journal of Physics D: Applied Physics* 35.19 (Sept. 2002), R157–R167. ISSN: 0022-3727. DOI: `10.1088/0022-3727/35/19/201`. URL: `http://dx.doi.org/10.1088/0022-3727/35/19/201`.

[35] Anton Shilov. *Seagate Ships First Comercial HAMR Hard Drives*. 2023. URL: `https://www.anandtech.com/show/18984/seagate-ships-first-commercial-hamr-hard-drives` (visited on 01/09/2024).

[36] James D. Kiely, Paul M. Jones, and Joel Hoehn. "Materials challenges for the heat-assisted magnetic recording head–disk interface". In: *MRS Bulletin* 43.2 (Feb. 2018), pp. 119–124. ISSN: 1938-1425. DOI: `10.1557/mrs.2018.4`. URL: `http://dx.doi.org/10.1557/mrs.2018.4`.

[37] T.W. McDaniel, W.A. Challener, and K. Sendur. "Issues in heat-assisted perpendicular recording". In: *IEEE Transactions on Magnetics* 39.4 (July 2003), pp. 1972–1979. ISSN: 0018-9464. DOI: `10.1109/tmag.2003.813752`. URL: `http://dx.doi.org/10.1109/TMAG.2003.813752`.

[38] Erhard Schreck et al. "Thermal Aspects and Static/Dynamic Protrusion Behaviors in Heat-Assisted Magnetic Recording". In: *IEEE Transactions on Magnetics* 50.3 (Mar. 2014), pp. 126–131. ISSN: 1941-0069. DOI: `10.1109/tmag.2013.2283715`. URL: `http://dx.doi.org/10.1109/TMAG.2013.2283715`.

[39] Roshan Mathew Tom et al. "Optical forces in heat-assisted magnetic recording head-disk interface". In: *Scientific Reports* 13.1 (May 2023). ISSN: 2045-2322. DOI: `10.1038/s41598-023-35126-3`. URL: `http://dx.doi.org/10.1038/s41598-023-35126-3`.

[40] Qilong Cheng and David B. Bogy. "Experimental study of smear formation and removal in heat-assisted magnetic recording". In: *Tribology International* 165 (Jan. 2022), p. 107258. ISSN: 0301-679X. DOI: `10.1016/j.triboint.2021.107258`. URL: `http://dx.doi.org/10.1016/j.triboint.2021.107258`.

[41] Shaomin Xiong et al. "Material Transfer From Media to Head in Heat Assisted Magnetic Recording (HAMR)". In: *ASME 2021 30th Conference on Information Storage and Processing Systems*. ISPS2021. American Society of Mechanical Engineers, June 2021. DOI: `10.1115/isps2021-64984`. URL: `http://dx.doi.org/10.1115/ISPS2021-64984`.

[42] Norio Tagawa et al. "Experimental Study on Smear Characteristics Upon Laser Heating in Air and Helium in Heat-Assisted Magnetic Recording". In: *IEEE Transactions on Magnetics* 57.2 (Feb. 2021), pp. 1–5. ISSN: 1941-0069. DOI: `10.1109/tmag.2020.3012979`. URL: `http://dx.doi.org/10.1109/TMAG.2020.3012979`.

[43] Qilong Cheng et al. "Measurement of angstrom-level laser induced protrusion using touchdown in heat-assisted magnetic recording". In: *Applied Physics Letters* 117.15 (Oct. 2020), p. 153105. DOI: 10.1063/5.0029051. URL: https://doi.org/10.1063/5.0029051.

[44] Kenji Yakata et al. "Smear and Decomposition Mechanism of Magnetic Disk PFPE Lubricant Film by Laser Heating in Air and Helium Conditions". In: *Tribology Online* 15.3 (June 2020), pp. 186–193. DOI: 10.2474/trol.15.186. URL: https://doi.org/10.2474/trol.15.186.

[45] Alejandro Rodriguez Mendez and David B. Bogy. "Lubricant Flow and Accumulation on the Slider's Air-Bearing Surface in a Hard Disk Drive". In: *Tribology Letters* 53.2 (Dec. 2013), pp. 469–476. DOI: 10.1007/s11249-013-0285-9. URL: https://doi.org/10.1007/s11249-013-0285-9.

[46] Siddhesh V. Sakhalkar and David B. Bogy. "Viscoelastic Lubricant Deformation and Disk-to-Head Transfer During Heat-Assisted Magnetic Recording". In: *IEEE Transactions on Magnetics* 55.7 (2019), pp. 1–6. DOI: 10.1109/TMAG.2018.2885434.

[47] James D. Kiely et al. "Write-Induced Head Contamination in Heat-Assisted Magnetic Recording". In: *IEEE Transactions on Magnetics* 53.2 (Feb. 2017), pp. 1–7. DOI: 10.1109/tmag.2016.2618842. URL: https://doi.org/10.1109/tmag.2016.2618842.

[48] Shaomin Xiong et al. "Experimental Study of Material Pick Up on Heat-Assisted Magnetic Recording (HAMR) Heads". In: *Tribology Letters* 69.2 (May 2021). DOI: 10.1007/s11249-021-01455-5. URL: https://doi.org/10.1007/s11249-021-01455-5.

[49] Roshan Mathew Tom, Qilong Cheng, and David B. Bogy. "A Hybrid Simulation For Smear Growth On HAMR Heads". In: *2023 IEEE International Magnetic Conference - Short Papers (INTERMAG Short Papers)*. IEEE, May 2023. DOI: 10.1109/intermagshortpapers58606.2023.10228588. URL: https://doi.org/10.1109/intermagshortpapers58606.2023.10228588.

[50] Jun Aoyama et al. "A head cleaning procedure for heat-assisted magnetic recording". In: *IEEE Transactions on Magnetics* 53.11 (2017), pp. 1–4.

[51] Qilong Cheng, Roshan Mathew Tom, and David B. Bogy. "Two Strategies to Mitigate Thermally-Induced Material Buildup in Heat-Assisted Magnetic Recording". In: *Tribology Letters* 71.2 (Apr. 2023). DOI: 10.1007/s11249-023-01723-6. URL: https://doi.org/10.1007/s11249-023-01723-6.

[52] Xingliang He and Bala Krishna Pathem. *High temperature lubricants for magnetic media.* US Patent 11,572,519. Feb. 2023.

[53] John L Brand and James D Kiely. *Heat-assisted removal of head contamination.* US Patent 10,373,632. Aug. 2019.

[54]   Vlad Novotny and Roger Hajjar. *Optical storage system with head cleaning mechanism based on a position-controllable optical interfacing surface in an optical head.* US Patent 6,307,832. Oct. 2001.

[55]   James Gary Wessel and Sarbeswar Sahoo. *Near-field transducer peg encapsulation.* US Patent App. 14/083,845. Dec. 2014.

[56]   Yuichi Aoki et al. *HAMR media to assist optically transparent build-up on NFT to improve reliability.* US Patent 10,950,267. Mar. 2021.

[57]   Sukumar Rajauria et al. *In-situ NFT pre-treatment to accumulate optically transparent material on NFT to improve reliability.* US Patent 11,244,703. Feb. 2022.

[58]   Sukumar Rajauria et al. *In-situ NFT pre-treatment to accumulate optically transparent material on NFT to improve reliability.* US Patent 10,950,266. Mar. 2021.

[59]   Jason W Riddering. *Head-medium contact sensor cleaning for heat-assisted magnetic recording device.* US Patent 9,875,764. Jan. 2018.

[60]   Tan Duy Trinh et al. *Heat-assisted magnetic recording (hamr) media with dual-layer media carbon overcoat.* US Patent App. 18/093,596. July 2023.

[61]   Sukumar Rajauria. *In-situ smear detection and mitigation in heat-assisted magnetic recording head-disk interface.* US Patent 9,601,140. Mar. 2017.

[62]   Qing Dai et al. *Reducing carbonaceous smear at the NFT area on HAMR head.* US Patent App. 15/232,889. Aug. 2017.

[63]   Shaomin Xiong et al. *Smear removal/mitigation by approaching head disk proximity.* 2016.

[64]   John L Brand. *Disk drive with oxygen diffusion unit.* US Patent 10,957,363. Mar. 2021.

[65]   Robert Smith et al. "Opto-Thermal Simulation of Metallic Smear's Impact on Hamr Technology". In: *2021 IEEE 32nd Magnetic Recording Conference (TMRC).* 2021, pp. 1–2. DOI: 10.1109/TMRC53175.2021.9605106.

[66]   Lin Wu and Frank E. Talke. "Modeling laser induced lubricant depletion in heat-assisted-magnetic recording systems using a multiple-layered disk structure". In: *Microsystem Technologies* 17.5–7 (May 2011), pp. 1109–1114. ISSN: 1432-1858. DOI: 10.1007/s00542-011-1300-4. URL: http://dx.doi.org/10.1007/s00542-011-1300-4.

[67]   Soroush Sarabi and David B. Bogy. "Effect of Viscoelasticity on Lubricant Behavior Under Heat-Assisted Magnetic Recording Conditions". In: *Tribology Letters* 66.1 (Jan. 2018). ISSN: 1573-2711. DOI: 10.1007/s11249-017-0979-5. URL: http://dx.doi.org/10.1007/s11249-017-0979-5.

[68]   Siddhesh V. Sakhalkar and David B. Bogy. "A Model for Lubricant Transfer from Media to Head During Heat-Assisted Magnetic Recording (HAMR) Writing". In: *Tribology Letters* 65.4 (Nov. 2017). ISSN: 1573-2711. DOI: 10.1007/s11249-017-0952-3. URL: http://dx.doi.org/10.1007/s11249-017-0952-3.

[69] Siddhesh V. Sakhalkar and David B. Bogy. "Effect of Rheology and Slip on Lubricant Deformation and Disk-to-Head Transfer During Heat-Assisted Magnetic Recording (HAMR)". In: *Tribology Letters* 66.4 (Oct. 2018). DOI: 10.1007/s11249-018-1100-4. URL: https://doi.org/10.1007/s11249-018-1100-4.

[70] Tan Shu et al. "Dynamic performance of head–disk interface in HAMR using molecular dynamics simulation method". In: *IEEE Transactions on Magnetics* 54.11 (2018), pp. 1–5.

[71] Qingkang Liu et al. "Study on the thermal decomposition of D-4OH PFPE lubricant by reactive molecular dynamic simulation for HAMR". In: *IEEE Transactions on Magnetics* 59.3 (2022), pp. 1–7.

[72] Young Woo Seo, Andrey Ovcharenko, and Frank E Talke. "Simulation of hydrocarbon oil contamination at the head–disk interface using molecular dynamics". In: *Tribology Letters* 61 (2016), pp. 1–10.

[73] Deng Pan et al. "Investigation of lubricant transfer between slider and disk using molecular dynamics simulation". In: *Tribology Letters* 53 (2014), pp. 373–381.

[74] B Marchon and Y Saito. "Lubricant thermodiffusion in heat assisted magnetic recording". In: *IEEE transactions on magnetics* 48.11 (2012), pp. 4471–4474.

[75] Yoko Saito, Naoya Sasaki, and Tokutaro Komatsu. "Molecular dynamics simulation for lubricant shear properties during heating". In: *IEEE transactions on magnetics* 48.6 (2011), pp. 2009–2015.

[76] Xiaobin Wang et al. "HAMR Recording Limitations and Extendibility". In: *IEEE Transactions on Magnetics* 49.2 (Feb. 2013), pp. 686–692. ISSN: 1941-0069. DOI: 10.1109/tmag.2012.2221689. URL: http://dx.doi.org/10.1109/TMAG.2012.2221689.

[77] Qilong Cheng. "Thermal Transport, Thermal Protrusion, and Thermally-Induced Material Transfer in the Head-Disk Interface of Heat-Assisted Magnetic Recording". English. PhD thesis. 2021, p. 119. URL: https://www.proquest.com/dissertations-theses/thermal-transport-protrusion-thermally-induced/docview/2741318041/se-2.

[78] Zhenghua Li, Dan Wei, and Fulin Wei. "Micromagnetic modeling for heat-assisted magnetic recording". In: *Journal of Magnetism and Magnetic Materials* 320.22 (Nov. 2008), pp. 3108–3112. ISSN: 0304-8853. DOI: 10.1016/j.jmmm.2008.08.085. URL: http://dx.doi.org/10.1016/j.jmmm.2008.08.085.

[79] X. W. Wu et al. "Nonmagnetic shell in surfactant-coated FePt nanoparticles". In: *Journal of Applied Physics* 95.11 (May 2004), pp. 6810–6812. ISSN: 1089-7550. DOI: 10.1063/1.1667803. URL: http://dx.doi.org/10.1063/1.1667803.

[80] Ashutosh Giri et al. "Influence of chemical ordering on the thermal conductivity and electronic relaxation in FePt thin films in heat assisted magnetic recording applications". In: *Scientific Reports* 6.1 (Aug. 2016). ISSN: 2045-2322. DOI: 10.1038/srep32077. URL: http://dx.doi.org/10.1038/srep32077.

[81] Alex Chernyshov et al. "Measurement of FePt thermal properties relevant to heat-assisted magnetic recording". In: *Journal of Applied Physics* 115.17 (Feb. 2014). ISSN: 1089-7550. DOI: 10.1063/1.4866519. URL: http://dx.doi.org/10.1063/1.4866519.

[82] S. V. Hainsworth and N. J. Uhure. "Diamond like carbon coatings for tribology: production techniques, characterisation methods and applications". In: *International Materials Reviews* 52.3 (May 2007), pp. 153–174. ISSN: 1743-2804. DOI: 10.1179/174328007x160272. URL: http://dx.doi.org/10.1179/174328007X160272.

[83] Jia-Yang Juang and David B. Bogy. "Air-Bearing Effects on Actuated Thermal Pole-Tip Protrusion for Hard Disk Drives". In: *Journal of Tribology* 129.3 (Feb. 2007), pp. 570–578. ISSN: 1528-8897. DOI: 10.1115/1.2736456. URL: http://dx.doi.org/10.1115/1.2736456.

[84] Lihong Gao, Fabien Lemarchand, and Michel Lequime. "Exploitation of multiple incidences spectrometric measurements for thin film reverse engineering". In: *Optics Express* 20.14 (June 2012), p. 15734. ISSN: 1094-4087. DOI: 10.1364/oe.20.015734. URL: http://dx.doi.org/10.1364/OE.20.015734.

[85] Mikhail N. Polyanskiy. "Refractiveindex.info database of optical constants". In: *Scientific Data* 11.1 (Jan. 2024). ISSN: 2052-4463. DOI: 10.1038/s41597-023-02898-2. URL: http://dx.doi.org/10.1038/s41597-023-02898-2.

[86] W. A. Challener et al. "Heat-assisted magnetic recording by a near-field transducer with efficient optical energy transfer". In: *Nature Photonics* 3.4 (Mar. 2009), pp. 220–224. ISSN: 1749-4893. DOI: 10.1038/nphoton.2009.26. URL: http://dx.doi.org/10.1038/nphoton.2009.26.

[87] Qilong Cheng, Siddhesh V. Sakhalkar, and David B. Bogy. "Direct measurement of disk-to-head back-heating in HAMR using a non-flying test stage". In: *Applied Physics Letters* 120.24 (June 2022). ISSN: 1077-3118. DOI: 10.1063/5.0092170. URL: http://dx.doi.org/10.1063/5.0092170.

[88] S. Sakhalkar et al. "Investigation of heat transfer across a nanoscale air gap between a flying head and a rotating disk". In: *Journal of Applied Physics* 128.8 (Aug. 2020). ISSN: 1089-7550. DOI: 10.1063/5.0012516. URL: http://dx.doi.org/10.1063/5.0012516.

[89] S. Zhang and D.B. Bogy. "A heat transfer model for thermal fluctuations in a thin slider/disk air bearing". In: *International Journal of Heat and Mass Transfer* 42.10 (May 1999), pp. 1791–1800. ISSN: 0017-9310. DOI: 10.1016/s0017-9310(98)00267-1. URL: http://dx.doi.org/10.1016/S0017-9310(98)00267-1.

[90] Du Chen, Nan Liu, and David B. Bogy. "A phenomenological heat transfer model for the molecular gas lubrication system in hard disk drives". In: *Journal of Applied Physics* 105.8 (Apr. 2009). ISSN: 1089-7550. DOI: 10.1063/1.3098231. URL: http://dx.doi.org/10.1063/1.3098231.

[91] Bair V. Budaev and David B. Bogy. "Heat transport by phonon tunneling across layered structures used in heat assisted magnetic recording". In: *Journal of Applied Physics* 117.10 (Mar. 2015). ISSN: 1089-7550. DOI: 10.1063/1.4914871. URL: http://dx.doi.org/10.1063/1.4914871.

[92] Bair V. Budaev and David B. Bogy. "Thermal rectification in inhomogeneous nanotubes". In: *Applied Physics Letters* 109.23 (Dec. 2016). ISSN: 1077-3118. DOI: 10.1063/1.4971390. URL: http://dx.doi.org/10.1063/1.4971390.

[93] Bair V. Budaev and David B. Bogy. "A wave theory of heat transport with applications to Kapitsa resistance and thermal rectification". In: *Proceedings of the Royal Society A: Mathematical, Physical and Engineering Sciences* 473.2198 (Feb. 2017), p. 20160584. ISSN: 1471-2946. DOI: 10.1098/rspa.2016.0584. URL: http://dx.doi.org/10.1098/rspa.2016.0584.

[94] S. Sakhalkar et al. "Numerical and experimental investigation of heat transfer across a nanoscale gap between a magnetic recording head and various media". In: *Applied Physics Letters* 115.22 (Nov. 2019). ISSN: 1077-3118. DOI: 10.1063/1.5119721. URL: http://dx.doi.org/10.1063/1.5119721.

[95] Siddhesh V. Sakhalkar, Qilong Cheng, and David B. Bogy. "Numerical and Experimental Investigation of Nanoscale Heat Transfer Between a Flying Head Over a Rotating Disk". In: *ASME 2020 29th Conference on Information Storage and Processing Systems*. ISPS2020. American Society of Mechanical Engineers, June 2020. DOI: 10.1115/isps2020-1906. URL: http://dx.doi.org/10.1115/ISPS2020-1906.

[96] Sha Lu. "Numerical simulation of slider air bearings". English. PhD thesis. 1997, p. 119.

[97] Tim Rausch et al. "Spin stand characterization of dielectric optical waveguides fabricated on AlTiC sliders for heat-assisted magnetic recording". In: *Optical Data Storage 2004*. Ed. by B. V. K. Vijaya Kumar and Hiromichi Kobori. SPIE, Sept. 2004. DOI: 10.1117/12.556004. URL: http://dx.doi.org/10.1117/12.556004.

[98] M. Kurita et al. "Flying-height reduction of magnetic-head slider due to thermal protrusion". In: *IEEE Transactions on Magnetics* 41.10 (Oct. 2005), pp. 3007–3009. ISSN: 0018-9464. DOI: 10.1109/tmag.2005.855240. URL: http://dx.doi.org/10.1109/TMAG.2005.855240.

[99] Brian Schultz. *Thermal Fly-height Control (TFC) Technology in Hitachi Hard Disk Drives*. 2007. URL: https://betasoft-outlet.com/ML/TFC_whitepaper041807.pdf (visited on 01/30/2024).

[100] Julien G. Noel. "Review of the properties of gold material for MEMS membrane applications". In: *IET Circuits, Devices, and Systems* 10.2 (Mar. 2016), pp. 156–161. ISSN: 1751-8598. DOI: 10.1049/iet-cds.2015.0094. URL: http://dx.doi.org/10.1049/iet-cds.2015.0094.

[101] Wenyi Zhang, Benjamin A. Friedman, and James A. Bain. "Simulation of a Thermally Efficient HAMR Ridge Waveguide NFT on an AIN Heat Sink". In: *2021 IEEE 32nd Magnetic Recording Conference (TMRC)*. IEEE, Aug. 2021. DOI: 10.1109/tmrc5317 5.2021.9605115. URL: http://dx.doi.org/10.1109/TMRC53175.2021.9605115.

[102] Chuan Zhong et al. "Effective heat dissipation in an adiabatic near-field transducer for HAMR". In: *Optics Express* 26.15 (July 2018), p. 18842. ISSN: 1094-4087. DOI: 10.1364/oe.26.018842. URL: http://dx.doi.org/10.1364/OE.26.018842.

[103] Qilong Cheng et al. "Experimental Study on Laser-Induced Protrusion in Heat-Assisted Magnetic Recording". In: *ASME 2020 29th Conference on Information Storage and Processing Systems*. ISPS2020. American Society of Mechanical Engineers, June 2020. DOI: 10.1115/isps2020-1903. URL: http://dx.doi.org/10.1115/ISPS2020-1903.

[104] Shaomin Xiong et al. "Spacing Control in Heat-Assisted Magnetic Recording". In: *IEEE Transactions on Magnetics* 55.3 (2019), pp. 1–6. DOI: 10.1109/TMAG.2018.286 8737.

[105] A. Ashkin. "Acceleration and Trapping of Particles by Radiation Pressure". In: *Phys. Rev. Lett.* 24 (4 Jan. 1970), pp. 156–159. DOI: 10.1103/PhysRevLett.24.156. URL: https://link.aps.org/doi/10.1103/PhysRevLett.24.156.

[106] Maurizio Righini et al. "Surface Plasmon Optical Tweezers: Tunable Optical Manipulation in the Femtonewton Range". In: *Phys. Rev. Lett.* 100 (18 May 2008), p. 186804. DOI: 10.1103/PhysRevLett.100.186804. URL: https://link.aps.org/doi/10.11 03/PhysRevLett.100.186804.

[107] Baoxi Xu et al. "HAMR Media Design in Optical and Thermal Aspects". In: *IEEE Transactions on Magnetics* 49.6 (June 2013), pp. 2559–2564. DOI: 10.1109/tmag.201 3.2257703. URL: https://doi.org/10.1109/tmag.2013.2257703.

[108] Siddhesh V. Sakhalkar and David B. Bogy. "Viscoelastic Lubricant Deformation and Disk-to-Head Transfer During Heat-Assisted Magnetic Recording". In: *IEEE Transactions on Magnetics* 55.7 (2019), pp. 1–6. DOI: 10.1109/TMAG.2018.2885434.

[109] Hiroshi Tani et al. "Investigation of mechanism of smear formation from diamond-like carbon films on heating". In: *Microsystem Technologies* 27.6 (Sept. 2020), pp. 2243–2255. DOI: 10.1007/s00542-020-05041-y. URL: https://doi.org/10.1007/s0054 2-020-05041-y.

[110] Shaomin Xiong et al. "Material Transfer Inside Head Disk Interface for Heat Assisted Magnetic Recording". In: *Tribology Letters* 65.2 (Apr. 2017). DOI: 10.1007/s11249-0 17-0860-6. URL: https://doi.org/10.1007/s11249-017-0860-6.

[111] Yuquan Zhang et al. "Plasmonic tweezers: for nanoscale optical trapping and beyond". In: *Light: Science & Applications* 10.1 (Mar. 2021). DOI: 10.1038/s41377-021-0047 4-0. URL: https://doi.org/10.1038/s41377-021-00474-0.

[112] Yasuhiro Harada and Toshimitsu Asakura. "Radiation forces on a dielectric sphere in the Rayleigh scattering regime". In: *Optics Communications* 124.5-6 (Mar. 1996), pp. 529–541. DOI: 10.1016/0030-4018(95)00753-9. URL: https://doi.org/10.1016/0030-4018(95)00753-9.

[113] R. Gans. "Über die Form ultramikroskopischer Goldteilchen". In: *Annalen der Physik* 342.5 (1912), pp. 881–900. DOI: 10.1002/andp.19123420503. URL: https://doi.org/10.1002/andp.19123420503.

[114] Uwe Kreibig and Michael Vollmer. *Optical Properties of Metal Clusters*. Springer Berlin Heidelberg, 1995. DOI: 10.1007/978-3-662-09109-8. URL: https://doi.org/10.1007/978-3-662-09109-8.

[115] Stefan A. Maier. *Plasmonics: Fundamentals and Applications*. Springer US, 2007. DOI: 10.1007/0-387-37825-1. URL: https://doi.org/10.1007/0-387-37825-1.

[116] M. Gallis, D. Rader, and J. Torczynski. "DSMC simulations of the thermophoretic force on a spherical macroscopic particle". In: *35th AIAA Thermophysics Conference*. American Institute of Aeronautics and Astronautics, June 2001. DOI: 10.2514/6.2001-2890. URL: https://doi.org/10.2514/6.2001-2890.

[117] Paul S. Epstein. "On the Resistance Experienced by Spheres in their Motion through Gases". In: *Phys. Rev.* 23 (6 June 1924), pp. 710–733. DOI: 10.1103/PhysRev.23.710. URL: https://link.aps.org/doi/10.1103/PhysRev.23.710.

[118] P. B. Johnson and R. W. Christy. "Optical constants of transition metals: Ti, V, Cr, Mn, Fe, Co, Ni, and Pd". In: *Phys. Rev. B* 9 (12 June 1974), pp. 5056–5070. DOI: 10.1103/PhysRevB.9.5056. URL: https://link.aps.org/doi/10.1103/PhysRevB.9.5056.

[119] Wolfgang S. M. Werner, Kathrin Glantschnig, and Claudia Ambrosch-Draxl. "Optical Constants and Inelastic Electron-Scattering Data for 17 Elemental Metals". In: *Journal of Physical and Chemical Reference Data* 38.4 (Dec. 2009), pp. 1013–1092. DOI: 10.1063/1.3243762. URL: https://doi.org/10.1063/1.3243762.

[120] Qingkang Liu et al. "Study on the Thermal Decomposition of D-4OH PFPE Lubricant by Reactive Molecular Dynamic Simulation for HAMR". In: *IEEE Transactions on Magnetics* 59.3 (Mar. 2023), pp. 1–7. ISSN: 1941-0069. DOI: 10.1109/tmag.2022.3211698. URL: http://dx.doi.org/10.1109/TMAG.2022.3211698.

[121] Sydney Chapman and T. G. Cowling. *Cambridge mathematical library: The mathematical theory of non-uniform gases*. en. Cambridge, England: Cambridge University Press, 1991. ISBN: 9780521408448.

[122] Changran Liu et al. "Theory and Experiment of Binary Diffusion Coefficient of n-Alkanes in Dilute Gases". In: *The Journal of Physical Chemistry A* 120.41 (Oct. 2016), pp. 8065–8074. DOI: 10.1021/acs.jpca.6b08261. URL: https://doi.org/10.1021/acs.jpca.6b08261.

[123] Changran Liu, Zhigang Li, and Hai Wang. "Drag force and transport property of a small cylinder in free molecule flow: A gas-kinetic theory analysis". In: *Physical Review E* 94.2 (Aug. 2016). DOI: `10.1103/physreve.94.023102`. URL: `https://doi.org/10.1103/physreve.94.023102`.

[124] Jun Wang, Shuang Luo, and Guodong Xia. "Thermophoretic force on nanocylinders in the free molecule regime". In: *Physical Review E* 95.3 (Mar. 2017). DOI: `10.1103/physreve.95.033101`. URL: `https://doi.org/10.1103/physreve.95.033101`.

[125] Shuang Luo et al. "Shear lift forces on nanocylinders in the free molecule regime". In: *Journal of Fluid Mechanics* 846 (May 2018), pp. 392–410. DOI: `10.1017/jfm.2018.295`. URL: `https://doi.org/10.1017/jfm.2018.295`.

[126] Roshan Mathew Tom, Qilong Cheng, and David B. Bogy. "A Numerical Simulation of PFPE Lubricant Kinetics in HAMR Air Bearing". In: *Tribology Letters* 72.2 (Apr. 2024). ISSN: 1573-2711. DOI: `10.1007/s11249-024-01853-5`. URL: `http://dx.doi.org/10.1007/s11249-024-01853-5`.

[127] Roshan Mathew Tom and David B. Bogy. "Ballistic material transport in HAMR head-disk interface". In: *2023 IEEE 34th Magnetic Recording Conference (TMRC)*. IEEE, July 2023. DOI: `10.1109/tmrc59626.2023.10264026`. URL: `https://doi.org/10.1109/tmrc59626.2023.10264026`.

[128] Robert Waltman and Connie Wiita. "Main Chain Effects in Tetraol-Functionalized Perfluoropolyethers". In: *Tribology Online* 10.4 (2015), pp. 262–272. DOI: `10.2474/trol.10.262`. URL: `https://doi.org/10.2474/trol.10.262`.

[129] R. J. Waltman and H. Deng. "Low Molecular Weight Z-Tetraol Boundary Lubricant Films in Hard Disk Drives". In: *Advances in Tribology* 2012 (2012), pp. 1–7. DOI: `10.1155/2012/964089`. URL: `https://doi.org/10.1155/2012/964089`.

[130] G.W. Tyndall et al. "Interfacial interactions of perfluoropolyether lubricants with magnetic recording media". In: *Tribology Letters* 4.2 (1998), pp. 103–108. DOI: `10.1023/a:1019199004170`. URL: `https://doi.org/10.1023/a:1019199004170`.

[131] Jacob N. Israelachvili. "Van der Waals Forces between Particles and Surfaces". In: *Intermolecular and Surface Forces*. Elsevier, 2011, pp. 253–289.

[132] B. Marchon and Y. Saito. "Lubricant Thermodiffusion in Heat Assisted Magnetic Recording". In: *IEEE Transactions on Magnetics* 48.11 (Nov. 2012), pp. 4471–4474. DOI: `10.1109/tmag.2012.2194138`. URL: `https://doi.org/10.1109/tmag.2012.2194138`.

[133] James D. Kiely et al. "Media Roughness and Head-Media Spacing in Heat-Assisted Magnetic Recording". In: *IEEE Transactions on Magnetics* 50.3 (2014), pp. 132–136. DOI: `10.1109/TMAG.2013.2291684`.

[134] Qilong Cheng, Yuan Ma, and David Bogy. "Effect of Humidity on the Nanoscale Heat Transfer at the Head-Media Interface". In: *ASME 2019 28th Conference on Information Storage and Processing Systems* (June 2019). DOI: 10.1115/isps2019-7449. URL: http://dx.doi.org/10.1115/ISPS2019-7449.

[135] Nisha Shukla et al. "Effect of Humidity on Lubricated Carbon Overcoats". In: *Tribology Letters* 12.2 (2002), pp. 105–109. DOI: 10.1023/a:1014085517456. URL: https://doi.org/10.1023/A:1014085517456.

[136] Dae-Young Lee et al. "Effect of relative humidity and disk acceleration on tribocharge build-up at a slider–disk interface". In: *Tribology International* 40.8 (Aug. 2007), pp. 1253–1257. DOI: 10.1016/j.triboint.2006.11.006. URL: https://doi.org/10.1016/j.triboint.2006.11.006.

[137] Sang Hoon Kim et al. "Humidity effects on lubricant transfer in the head-disk interface of a hard disk drive". In: *Journal of Applied Physics* 105.7 (2009). DOI: 10.1063/1.3061704.

[138] Qilong Cheng et al. "Dependence of nanoscale heat transfer across a closing gap on the substrate material and ambient humidity". In: *Applied Physics Letters* 116.21 (May 2020). DOI: 10.1063/5.0010286. URL: https://doi.org/10.1063/5.0010286.

[139] Thomas E. Karis. "Water Adsorption on Thin Film Media". In: *Journal of Colloid and Interface Science* 225.1 (May 2000), pp. 196–203. DOI: 10.1006/jcis.2000.6745. URL: https://doi.org/10.1006/jcis.2000.6745.

[140] Ryan Z. Lei and Andrew J. Gellman. "Humidity Effects on PFPE Lubricant Bonding to a-CHx Overcoats". In: *Langmuir* 16.16 (July 2000), pp. 6628–6635. DOI: 10.1021/la9915973. URL: https://doi.org/10.1021/la9915973.

[141] G. W. Tyndall, R. J. Waltman, and J. Pacansky. "Effect of adsorbed water on perfluoropolyether-lubricated magnetic recording disks". In: *Journal of Applied Physics* 90.12 (Dec. 2001), pp. 6287–6296. DOI: 10.1063/1.1413946. URL: https://doi.org/10.1063/1.1413946.

[142] R. R. Dubin et al. "Degradation of Co-based thin-film recording materials in selected corrosive environments". In: *Journal of Applied Physics* 53.3 (Mar. 1982), pp. 2579–2581. DOI: 10.1063/1.330913. URL: https://doi.org/10.1063/1.330913.

[143] Abdullah Al Mamun, GuoXiao Guo, and Chao Bi. *Hard Disk Drive: Mechatronics and Control.* Dec. 2017. DOI: 10.1201/9781420004106. URL: http://dx.doi.org/10.1201/9781420004106.

[144] Weidong Huang, David B. Bogy, and Alejandro L. Garcia. "Three-dimensional direct simulation Monte Carlo method for slider air bearings". In: *Physics of Fluids* 9.6 (June 1997), pp. 1764–1769. ISSN: 1089-7666. DOI: 10.1063/1.869293. URL: http://dx.doi.org/10.1063/1.869293.

[145] Francis J. Alexander, Alejandro L. Garcia, and Berni J. Alder. "A Consistent Boltzmann Algorithm". In: *Physical Review Letters* 74.26 (June 1995), pp. 5212–5215. ISSN: 1079-7114. DOI: 10.1103/physrevlett.74.5212. URL: http://dx.doi.org/10.1103/PhysRevLett.74.5212.

[146] Sydney Chapman and T G Cowling. *Cambridge mathematical library: The mathematical theory of non-uniform gases: An account of the kinetic theory of viscosity, thermal conduction and diffusion in gases.* en. Cambridge, England: Cambridge University Press, Jan. 1991.

[147] G A Bird. *Molecular gas dynamics and the direct simulation of gas flows.* en. Oxford Engineering Science Series. Oxford, England: Clarendon Press, May 1994.

[148] Francis J Alexander and Alejandro L Garcia. "The direct simulation Monte Carlo method". In: *Computers in Physics* 11.6 (1997), pp. 588–593.

[149] E P Muntz. "Rarefied Gas Dynamics". In: *Annual Review of Fluid Mechanics* 21.1 (Jan. 1989), pp. 387–422. ISSN: 1545-4479. DOI: 10.1146/annurev.fl.21.010189.002131. URL: http://dx.doi.org/10.1146/annurev.fl.21.010189.002131.

[150] Zhi-Xin Sun et al. "Proper cell dimension and number of particles per cell for DSMC". In: *Computers and Fluids* 50.1 (Nov. 2011), pp. 1–9. ISSN: 0045-7930. DOI: 10.1016/j.compfluid.2011.04.013. URL: http://dx.doi.org/10.1016/j.compfluid.2011.04.013.

[151] Alejandro L Garcia. *Numerical methods for physics.* Prentice Hall Englewood Cliffs, NJ, 2000.

[152] Katsuhisa Koura and Hiroaki Matsumoto. "Variable soft sphere molecular model for inverse-power-law or Lennard-Jones potential". In: *Physics of Fluids A: Fluid Dynamics* 3.10 (Oct. 1991), pp. 2459–2465. ISSN: 0899-8213. DOI: 10.1063/1.858184. URL: http://dx.doi.org/10.1063/1.858184.

[153] H. A. Hassan and David B. Hash. "A generalized hard-sphere model for Monte Carlo simulation". In: *Physics of Fluids A: Fluid Dynamics* 5.3 (Mar. 1993), pp. 738–744. ISSN: 0899-8213. DOI: 10.1063/1.858656. URL: http://dx.doi.org/10.1063/1.858656.

[154] Francis J. Alexander, Alejandro L. Garcia, and Berni J. Alder. "Simulation of the consistent Boltzmann equation for hard spheres and its extension to higher densities". In: *Lecture Notes in Physics.* Springer Berlin Heidelberg, pp. 82–90. ISBN: 9783540492030. DOI: 10.1007/3-540-59158-3_36. URL: http://dx.doi.org/10.1007/3-540-59158-3_36.

[155] Jerome J Erpenbeck and William W Wood. "Molecular dynamics calculations of the hard-sphere equation of state". In: *Journal of statistical physics* 35 (1984), pp. 321–340.

[156] SJ Plimpton et al. "Direct simulation Monte Carlo on petaflop supercomputers and beyond". In: *Physics of Fluids* 31.8 (2019). URL: http://sparta.sandia.gov.

[157] Argyrios Anagnostopoulos, Alessio Alexiadis, and Yulong Ding. "Simplified force field for molecular dynamics simulations of amorphous SiO2 for solar applications". In: *International Journal of Thermal Sciences* 160 (Feb. 2021), p. 106647.

[158] Santosh Kumar Meena et al. "The role of halide ions in the anisotropic growth of gold nanoparticles: a microscopic, atomistic perspective". In: *Physical Chemistry Chemical Physics* 18.19 (2016), pp. 13246–13254.

[159] Jianwei Che, Tahir Çağın, and William A. Goddard III. "Generalized extended empirical bond-order dependent force fields including nonbond interactions". In: *Theoretical Chemistry Accounts: Theory, Computation, and Modeling (Theoretica Chimica Acta)* 102.1-6 (June 1999), pp. 346–354.

[160] D. Y. Lee, J. Hwang, and G. N. Bae. "Effect of disk rotational speed on contamination particles generated in a hard disk drive". In: *Microsystem Technologies* 10.2 (Jan. 2004), pp. 103–108. ISSN: 1432-1858. DOI: 10.1007/s00542-003-0327-6. URL: http://dx.doi.org/10.1007/s00542-003-0327-6.

[161] C Y Maghfiroh et al. "Parameters of Lennard-Jones for Fe, Ni, Pb for Potential and Cr based on Melting Point Values Using the Molecular Dynamics Method of the Lammps Program". In: *Journal of Physics: Conference Series* 1491.1 (Mar. 2020), p. 012022. ISSN: 1742-6596. DOI: 10.1088/1742-6596/1491/1/012022. URL: http://dx.doi.org/10.1088/1742-6596/1491/1/012022.

[162] Simon Stephan et al. "MolMod – an open access database of force fields for molecular simulations of fluids". In: *Molecular Simulation* 45.10 (Apr. 2019), pp. 806–814. ISSN: 1029-0435. DOI: 10.1080/08927022.2019.1601191. URL: http://dx.doi.org/10.1080/08927022.2019.1601191.

[163] P.C. Kohnke. *ANSYS Theory Reference: Release 5.6.* ANSYS Incorporated, 1999.

[164] Panayiotis Papadopoulos. "An Introduction to the Finite Element Method". ME 280A Class Notes. 2019.

[165] Jon Wilkening. "Hand-written lecture notes for Math 228B". 2021.

Appendix A

FEM Solutions

A.1 The Transient Heat Conduction Equation

This FEM procedure is adapted from Ansys theory reference [163] (variational statement), Papadopoulos (2019) [164] (matrix assembly and numerical integration), and Wilkening (2021) [165] (reference element transformations).

A.1.1 The Weak Form of the Differential Equation

We begin with the strong form of the transient heat conduction equation given by:

$$\rho C \left(\frac{\partial T}{\partial t} + u \cdot \nabla T \right) = \nabla(\kappa \nabla T) + q_{gen} \tag{A.1}$$

The Dirichlet boundary condition specifies the nodal values of the temperature field,

$$T = T_o \tag{A.2}$$

The Neumann boundary condition can either be a total heat flux or the heat transfer coefficient, which are given by

$$q = q^* = h_f(T_d - T_f) \tag{A.3}$$

where

$$q = \text{Heat flux vector (W/m}^2) = -\kappa \nabla T$$
$$q^* = \text{Specified heat flow (W/m}^2)$$
$$h_f = \text{Heat transfer coefficient (W/m}^2\text{K)}$$
$$T_d = \text{Temperature of adjacent body or fluid (K)}$$
$$T_f = \text{Surface Temperature (K)}$$

For a small perturbation in temperature δT, we can then write the variational weak form of differential equation as:

$$\int_\Omega \delta T \left[\rho C \left(\frac{\partial T}{\partial t} + u \cdot \nabla T \right) \right] d\Omega = \int_\Omega \delta T \left(\nabla(\kappa \nabla T) + q_{gen} \right) d\Omega + \int_{\Gamma_2} \delta T q^* d\Gamma_2$$
$$+ \int_{\Gamma_3} \delta T \left(h_f(T_d - T_f) \right) d\Gamma_3 \tag{A.4}$$

where,

$$\Omega = \text{Simulation domain}$$
$$\Gamma_1 = \text{Boundary surface with specified temperature}$$
$$\Gamma_2 = \text{Boundary surface with specified heat flux}$$
$$\Gamma_3 = \text{Boundary surface with specified heat transfer coefficient}$$
$$\text{Such that } \partial\Omega = \Gamma_1 + \Gamma_2 + \Gamma_3$$

A.1.2 Element Matrices

Since the differential equation that satisfies the whole domain also satisfies individual elements, we can use Eq A.4 for each element form. The fluxes between the element surfaces are ignored as they cancel out when the individual element matrices are assembled into the global equation. Using shape function $[N]$, we can write.

$$T = [N]^T[T_e]$$
$$\delta T = [N]^T[\delta T_e]$$
$$\nabla T = \nabla[N]^T[T_e] = [B]^T[T_e] \text{ where, } [B] = \nabla[N]$$
$$\frac{\partial T}{\partial t} = [N]^T \frac{\partial[T_e]}{\partial t} = [N]^T[\dot{T}_e]$$

where the subscript e represents the nodal values of the element. Imposing the restrictions from Sec 2.2.1 ($u = 0$, $q_{gen} = 0$) and dropping the arbitrary δT, we can transform Eq. A.4 to:

$$\rho C \int_{\Omega_e} [N][N]^T d\Omega_e[\dot{T}_e] = \kappa \int_{\Omega_e} [B][B]^T d\Omega_e[T_e] + \int_{\Gamma_2} [N]q^* d\Gamma_2 + hT_d \int_{\Gamma_3} [N]d\Gamma_3$$
$$- h_f \int_{\Gamma_3} [N][N]^T d\Gamma_3[T_e] \tag{A.5}$$
$$\Rightarrow [C_e^t][\dot{T}_e] + \left([K_e^b] + [K_e^t] \right)[T_e] = [Q_e^c] + [Q_e^f] \tag{A.6}$$

where,

$$C_e^t = \rho C \int_{\Omega_e} [N][N]^T d\Omega_e \qquad \text{(Element-specific heat matrix)}$$

$$K_e^b = -\kappa \int_{\Omega_e} [B][B]^T d\Omega_e \qquad \text{(Element-diffusion conductivity matrix)}$$

$$K_e^t = h_f \int_{\Omega_e} [N][N]^T d\Omega_e \qquad \text{(Element-convection surface conductivity matrix)}$$

$$Q_e^c = T_B h_f \int_{\Gamma_3} [N] d\Gamma_3 \qquad \text{(Element convection surface heat flow vector)}$$

$$Q_e^f = \int_{\Gamma_2} [N] q^* d\Gamma_2 \qquad \text{(Element heat flux vector)}$$

A.1.3 Element and Shape functions

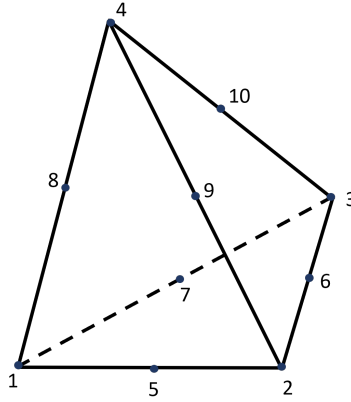A 10-node tetrahedron (Fig. A.1) discretizes the simulation domain.

Figure A.1: 10 node tetrahedron

The shape functions are:

$$[N] = \begin{bmatrix} (2L_1 - 1)L_1 \\ (2L_2 - 1)L_2 \\ (2L_3 - 1)L_3 \\ (2L_4 - 1)L_4 \\ L_1 L_2 \\ L_2 L_3 \\ L_1 L_3 \\ L_1 L_4 \\ L_2 L_4 \\ L_3 L_4 \end{bmatrix} \text{where,} \quad \begin{aligned} L_1 &= 1 - r - s - t \\ L_2 &= r \\ L_3 &= s \\ L_4 &= t \end{aligned} \tag{A.7}$$

The terms r, s, and t are parameters such that at node i, $N_i = 1$. Further, the gradient of the shape matrix can be defined as:

$$[B] = \mathbf{J}^{-1} \begin{bmatrix} \frac{\partial [N]}{\partial r} & \frac{\partial [N]}{\partial s} & \frac{\partial [N]}{\partial t} \end{bmatrix} \tag{A.8}$$

where, $\mathbf{J}$ is the Jacobian given by:

$$\mathbf{J} = \begin{bmatrix} x_2 - x_1 & x_3 - x_1 & x_4 - x_1 \\ y_2 - y_1 & y_3 - y_1 & y_4 - y_1 \\ z_2 - z_1 & z_3 - z_1 & z_4 - z_1 \end{bmatrix} \tag{A.9}$$

where (x_i, y_i, z_i) are the coordinates of the node i. The Jacobian transforms the gradient operator from the reference element to the real element.

A.1.4 Integration Scheme

The integration of the matrices in Eq A.6 was conducted using Gaussian quadrature. We integrate a reference element with unit volume and equal edges.

Volume integrals

For any element volume integral, we approximate the integral using a 4-point quadrature.

$$A = \int_{\Omega_e} f(r, s, t) d\Omega_e = V_e \sum_{i=0}^{4} w_i f(r_i, s_i, t_t) \tag{A.10}$$

where V_e is the volume of the element. The quadrature points are:

r	s	t	w
0.58541020	0.13819660	0.13819660	0.25
0.13819660	0.58541020	0.13819660	0.25
0.13819660	0.13819660	0.58541020	0.25
0.13819660	0.13819660	0.13819660	0.25

$$\tag{A.11}$$

Surface integrals

For any surface integral, we approximate the integral using a 6-point quadrature

$$S = \int_{\Gamma_e} f(r, s) d\Gamma_e = A_e \sum_{i=0}^{6} w_i f(r_i, s_i) \tag{A.12}$$

where A_e is the area of the element. The quadrature points are:

$$
\begin{array}{cc|c}
r & s & w \\
\hline
0.0915762 & 0.0915762 & 0.1099517 \\
0.8168476 & 0.0915762 & 0.1099517 \\
0.0915762 & 0.8168476 & 0.1099517 \\
0.4459485 & 0.4459485 & 0.2233816 \\
0.1081030 & 0.4459485 & 0.2233816 \\
0.4459485 & 0.1081030 & 0.2233816 \\
\end{array}
\tag{A.13}
$$

A.1.5 Time Semi-discretization

We use a 2-stage, L-stable SDIRK method for time-stepping with the Butcher array given by

$$
\begin{array}{c|cc}
r & r & \\
1 & b & r \\
\hline
 & b & r
\end{array}
\qquad \text{where } r = 1 - \frac{\sqrt{2}}{2},\, b = \frac{\sqrt{2}}{2}
\tag{A.14}
$$

Eq. A.6 can be transformed as:

$$
[\dot{T}] = [C^t]^{-1} \left\{ [Q^f] + [Q^c] - [K^b][T] - [K^t][T] \right\}
$$
$$
\Rightarrow \frac{\partial [T]}{\partial t} = f(t, [T])
\tag{A.15}
$$
$$
\text{where,}
$$
$$
f(t, [T]) = [C^t]^{-1}[Q(t)] + [C^t]^{-1}[K([T])]
\tag{A.16}
$$

Then, for a timestep, dt

$$
[T_{n+1}] = [T_n] + dt\,(b[k_1] + r[k_2])
\tag{A.17}
$$
$$
\text{where,}
$$
$$
k_1 = f(t_n + rdt, [T] + rdt[k_1])
\tag{A.18}
$$
$$
k_2 = f(t_n + dt, [T] + bdt[k_1] + rdt[k_2])
\tag{A.19}
$$

The terms $[k_1]$ and $[k_2]$ are terms that quantify the rate of change of $[T]$. Therefore, the Dirichlet boundary conditions can now be strictly imposed by setting $[k_{1,fixed}] = [k_{2,fixed}] = 0$. Thus,

$$
[T_{n+1,free}] = [T_{n,free}] + dt\,(b[k_{1,free}] + r[k_{2,free}])
\tag{A.20}
$$

In all simulations, we use a conjugate gradient method up to a residual norm of 1×10^{-6} to solve for k_1 and k_2 with a timestep of 100 picoseconds.

A.2 Structural Equation

A.2.1 The Weak Form of the Differential Equation

The governing differential equation for structural simulation is Cauchy's first law given by,

$$\nabla \cdot \boldsymbol{\sigma} = 0 \tag{A.21}$$

constrained by,

$$\boldsymbol{\sigma} = \boldsymbol{D}(\boldsymbol{\epsilon} - \boldsymbol{\alpha}\nabla T) \tag{A.22}$$

$$\boldsymbol{\sigma}\boldsymbol{n} = \boldsymbol{P}_{ext} \tag{A.23}$$

where $\boldsymbol{\sigma}$ and $\boldsymbol{\epsilon}$ are second order stress and strain tensors. $\boldsymbol{\alpha}$ is the coefficient of linear expansion of isotropic materials. For a material with Young's modulus, E and Poisson ratio, ν, the stiffness matrix, $\boldsymbol{D}$ is given by:

$$\boldsymbol{D} = \begin{bmatrix} \frac{1}{E} & -\frac{\nu}{E} & -\frac{\nu}{E} & 0 & 0 & 0 \\ -\frac{\nu}{E} & \frac{1}{E} & -\frac{\nu}{E} & 0 & 0 & 0 \\ -\frac{\nu}{E} & -\frac{\nu}{E} & \frac{1}{E} & 0 & 0 & 0 \\ 0 & 0 & 0 & \frac{E}{2(1+\nu)} & 0 & 0 \\ 0 & 0 & 0 & 0 & \frac{E}{2(1+\nu)} & 0 \\ 0 & 0 & 0 & 0 & 0 & \frac{E}{2(1+\nu)} \end{bmatrix}^{-1} \tag{A.24}$$

For a small displacement, $\delta\boldsymbol{u}$, the weak form can be written as

$$\int_{\Omega} \boldsymbol{\epsilon}(\delta\boldsymbol{u})\boldsymbol{D}\boldsymbol{\epsilon}(\boldsymbol{u})d\Omega = \int_{\Gamma} \delta\boldsymbol{u}P_{ext}d\Gamma \tag{A.25}$$

A.2.2 Element Matrices

At a given node, the displacement, stress, strain fields, and coefficient of expansion vector can be written as,

$$\boldsymbol{u} = \begin{bmatrix} u_x & u_y & u_z \end{bmatrix}^T \tag{A.26}$$

$$\boldsymbol{\epsilon} = \begin{bmatrix} \epsilon_x & \epsilon_y & \epsilon_z & \epsilon_{xy} & \epsilon_{xz} & \epsilon_{yz} \end{bmatrix}^T \tag{A.27}$$

$$\boldsymbol{\sigma} = \begin{bmatrix} \sigma_x & \sigma_y & \sigma_z & \sigma_{xy} & \sigma_{xz} & \sigma_{yz} \end{bmatrix}^T \tag{A.28}$$

$$\boldsymbol{\alpha} = \begin{bmatrix} \alpha & \alpha & \alpha & 0 & 0 & 0 \end{bmatrix}^T \tag{A.29}$$

For a 10-node tetrahedron, with the set of shape functions, [N], we can write the displacement field to the strain field as:

$$[\epsilon] = [B^e][u^e] \tag{A.30}$$

$$\text{where } [B] = \begin{bmatrix} \frac{\partial[N_1]}{\partial x} & 0 & 0 & \cdots & \cdots \\ 0 & \frac{\partial[N_2]}{\partial y} & 0 & \cdots & \cdots \\ 0 & 0 & \frac{\partial[N_3]}{\partial z} & \cdots & \cdots \\ \frac{\partial[N_1]}{\partial y} & \frac{\partial[N_1]}{\partial x} & 0 & \cdots & \cdots \\ \frac{\partial[N_1]}{\partial z} & 0 & \frac{\partial[N_1]}{\partial x} & \cdots & \cdots \\ 0 & \frac{\partial[N_1]}{\partial z} & \frac{\partial[N_1]}{\partial y} & \cdots & \cdots \end{bmatrix}_{6 \times 30} \tag{A.31}$$

The element discretized version of Eq. A.25 can then be written as,

$$\int_{\Omega} [B]^T[D][B][u]d\Omega = \int_{\Omega} [B]^T[D][\epsilon^{th}]d\Omega + \int_{\Gamma} [N]^T[P]d\Gamma \tag{A.32}$$

$$\Rightarrow [K_e][u] = [F_e^{th}] + [F_e^{pr}] \tag{A.33}$$

where,

$$K_e = \int_{\Omega_e} [B]^T[D][B]d\Omega_e \qquad \text{(Element stiffness matrix)}$$

$$F_e^{th} = \int_{\Omega_e} [B]^T[D][\epsilon^{th}]d\Omega_e \qquad \text{(Element thermal load vector)}$$

$$= \int_{\Omega_e} [B]^T[D][\alpha][N][\Delta T]d\Omega_e$$

$$F_e^{pr} = \int_{\Gamma} [N]^T[P_{ext}]d\Gamma \qquad \text{(Element pressure vector)}$$

The domain is discretized into 80,000 10-node tetrahedral elements. The shape function and integration schemes are the same as the one used for the transient heat conduction equation (Sec. A.1.3 and Sec. A.1.4). Finally, the unknown displacement field is then calculated by solving Eq. A.33 using a conjugate gradient method.